

# The Behavior of Titanium Alpha Alloys during Hot Creep Forming

TARIK NAWAYA



SIEGENER WERKSTOFFKUNDLICHE BERICHTE | BAND 35/2023  
HERAUSGEBER: PROF. DR.-ING. HABIL. H.-J. CHRIST  
PROF. DR.-ING. AXEL VON HEHL



**Tarik Nawaya**

The Behavior of Titanium Alpha Alloys during Hot Creep Forming

Herausgeber:  
Prof. Dr.-Ing. habil. H.-J. Christ  
Prof. Dr.-Ing. Axel von Hehl  
Lehrstuhl für Materialkunde und Werkstoffprüfung  
Institut für Werkstofftechnik  
Paul-Bonatz-Str. 9-11  
Universität Siegen  
D-57068 Siegen

© Copyright Tarik Nawaya 2023

© Copyright Lehrstuhl für Materialkunde und Werkstoffprüfung,  
Universität Siegen 2023

Alle Rechte vorbehalten, auch das des auszugsweisen Nachdruckes,  
der auszugsweisen oder vollständigen Wiedergabe, der Speicherung  
in Datenverarbeitungsanlagen und das der Übersetzung.

Als Manuskript gedruckt. Printed in Germany.

urn:nbn:de:hzb:467-27032

<https://dspace.ub.uni-siegen.de/handle/ubsi/2703>

<https://doi.org/10.25819/ubsi/10489>

ISSN 2193-5106

# **The Behavior of Titanium Alpha Alloys during Hot Creep Forming**

DISSERTATION

to obtain the degree of Doctor  
of Engineering

submitted by M.Sc. Tarik Nawaya.

Submitted to the Faculty of Natural Sciences and Technology  
of the University of Siegen.

Supervisor and First Appraiser

Prof. Dr.-Ing. Axel von Hehl

University of Siegen

Second Appraiser

Prof. Dr.-Ing. Frank Balle

Department of Sustainable Systems Engineering-

INATECH (Uni-Freiburg)

Date of the oral Examination

26.05.2023





## Preface

The present work was created based on the results obtained during my job as a research assistant at the Leibniz Institute for Materials Engineering (Leibniz-IWT, Bremen) in the period 10.2016-04.2020. My special thanks go to Prof. Dr.-Ing. Axel von Hehl, the former head of the department of lightweight materials, for taking over the role of advisor and for the encouragement during my employment at the institute as well as during the preparation for the doctoral thesis. Furthermore, I would also like to thank Prof. Dr.-Ing. Balle for taking on the position of second appraiser.

I would also like to thank Prof. Dr.-Ing. Hans-Werner Zoch, the former head of the institute at the time, for his support of my work.

Special thanks to my former colleagues in the lightweight materials department at Leibniz-IWT for the helpfulness shown.

I would also like to thank Mr. Werner Beck and Ms. Sabine Wagner from FormTech GmbH for all the facilities they provided, contributing to the success of this work. Similar thanks go to the cooperating scientists from Fraunhofer IFAM, Bremen, who share many results to set them free for my thesis.

Dr.-Ing. habil Nikolai Kashaev, Dr. Volker Ventzke, and Mr. Stefan Riekehr from Helmholtz-Zentrum Hereon in Geestacht have been very supportive through the many fruitful discussions and made many studies feasible. Thank you for this.

Not to mention my wife Lujain for her patience and support, which significantly contributed to this work's success. An important thanks to my siblings for motivating me all along the way.

Finally, I would like to thank my father and mother, who have been wishing for me to obtain a doctorate for ten years. They not only set the basic conditions for this work by making my entire education possible. They were and still are my great support in every situation.

## **Vorwort**

Die vorliegende Arbeit entstand auf Basis der während meiner Tätigkeit als wissenschaftlicher Mitarbeiter am Leibniz Institut für werkstofforientierte Technologien (Leibniz-IWT, Bremen) durchgeführten Studien im Zeitraum 10.2016-04.2020.

Herrn Prof. Dr.-Ing. Axel von Hehl, dem ehemaligen Leiter der Abteilung Leichtbauwerkstoffe, gilt mein besonderer Dank für die Betreuung und Begutachtung der Doktorarbeit sowie für die äußerst vorantreibende Unterstützung während der Beschäftigung am Institut sowie der Anfertigung dieser Arbeit. Des Weiteren möchte ich mich bei Herrn Prof. Dr.-Ing. Frank Balle für die Übernahme des Zweitgutachtens bedanken.

Herrn Prof. Dr.-Ing. Hans-Werner Zoch, dem ehemaligen Institutsleiter, danke ich für die Unterstützung während der Beschäftigung am Forschungsinstitut. Allen ehemaligen Kollegen insbesondere der Abteilung der Leichtbauwerkstoffe am Leibniz-IWT möchte ich für die mir entgegengebrachte Hilfsbereitschaft danken.

Ich bedanke mich auch bei Herrn Werner Beck und Frau Sabine Wagner aus der Firma FormTech GmbH für die Hilfe. Ein großer Dank gilt den kooperierenden Wissenschaftlern des Fraunhofer IFAM in Bremen für die hervorragende Zusammenarbeit.

Dr. Ing.- habil Nikolai Kashaev, Dr. Volker Ventzke und Herrn Stefan Riekehr vom Helmholtz-Zentrum Hereon danke ich vielmals für die vielen fruchtbaren Diskussionen und den Zugang zu ergänzende Studien.

Meiner Frau Lujain danke ich auch für ihre Geduld und Unterstützung, was zum Gelingen dieser Arbeit wesentlich beigetragen hat. Ein großer Dank geht auch an meine Geschwister, die mich den ganzen Weg lang motiviert haben.

Nicht zu guter Letzt danke ich meinem Vater und meiner Mutter, die das Erreichen der Promotion seit zehn Jahren für mich wünschen. Sie haben nicht nur durch das Ermöglichen meiner gesamten Ausbildung die Voraussetzung für diese Arbeit geschaffen, sie waren und sind mir in jeder Situation der große Rückhalt.

**Acknowledgement**

This doctoral thesis is accomplished majorly based on the results of the research project “TiB-Air” (20W1522E), which is funded by the Bundesministerium für Wirtschaft und Energie (BMWi) due to a resolution of the Deutscher Bundestag within the “Luftfahrtforschungsprogramm 5-2”. The author is grateful for the financial support

**Gefördert durch:**

Bundesministerium  
für Wirtschaft  
und Energie

**aufgrund eines Beschlusses  
des Deutschen Bundestages**

Hiermit versichere ich, dass ich die vorliegende Arbeit selbständig und ohne fremde Hilfe verfasst habe. Ebenfalls sind die verwendeten Hilfsmittel und Quellen vollständig angegeben. Wörtlich übernommene Textstellen, Bilder und Zeichnungen sind in jedem Einzelfall kenntlich gemacht worden.

**Kassel, 21.02.2021****Tarik Nawaya**

## Abstract

Hot creep forming (HCF) is an innovative sheet metal forming process used to obtain high demands on material properties along with high geometric accuracy in terms of dimensional and shape stability without any need for post-treatment. Such a manufacturing process has been used mainly for special aluminum alloys. The application on titanium alloys is not known so far.

Titanium alloys, on the other hand, have excellent density-specific mechanical properties combined with high chemical resistance, making them preferred in the aerospace industry. The mechanical properties such as the deformation behavior, are strongly determined by the existing microstructure and phase composition. In this context, the crystal modifications of  $\alpha$ -titanium (hexagonal) and  $\beta$ -titanium (body-centered cubic) differ significantly.

A compromise is offered by the mixed form  $\alpha + \beta$  titanium alloys, which are represented by the most common titanium alloy, Ti-6Al-4V. The latter alloy is used in many different areas, from aerospace to medical applications, and their usage has, therefore, already been widely explored.  $\alpha$ -titanium alloys have so far been used in automobiles, sports goods, and biomedical applications, but rarely in the aerospace industry.

In this work, the behavior of several titanium alpha alloys has been investigated during the hot creep forming process. KS1.2ASNEX, Exhaust-XT®, and ASTM grade 04 were the spoken alloys owing to their excellent oxidation resistance at high temperatures. However, the pronounced springback behavior of titanium alloys poses a significant challenge for sheet metal forming in order to produce dimensionally accurate and stable components and should definitely be avoided. Since the springback effect is temperature dependent, the springback behavior at different temperature levels was investigated. To develop a better understanding of material behavior during hot creep forming, several factors were varied and analyzed for their influence. The relationships between the significant factors such as forming temperature, heating time, creep strain, strain rate and relaxation time were worked out by means of a statistical design of experiments, on the basis of which the HCF process was optimized. In order to analyze the influence of further parameters such as the friction coefficient, die temperature and blankholder force and to use them for process optimization, HCF simulations based on the finite element method were carried out. Based on the approach mentioned above, forming temperature and relaxation time are the most significant factors to impact the oxidation behavior and the residual stresses. The alloy KS1.2ASNEX exhibits the best behavior at 650°C with a relaxation time of 720s so that full stress relief can be achieved without any detrimental oxidation layers. The simulation also shows an improvement in results due to a small coefficient of friction in combination with increasing the blank holding force. The experimental research was accompanied by metallographic investigations, which were used to evaluate the process-microstructure-property relationships.

## Kurzfassung

Hot Creep Forming (Warmkriechformen) ist ein innovatives Blechformgebungsverfahren, mit dem hohe Anforderungen an die Materialeigenschaften und zugleich mit Blick auf die geforderte Maß- und Formhaltigkeit eine hohe geometrische Genauigkeit erzielt werden können, ohne dass eine Nachbehandlung der gefertigten Blechformteile erforderlich ist. Solch ein Fertigungsverfahren wurde bisher hauptsächlich auf spezielle Aluminiumlegierungen angewandt. Eine Anwendung auf Titanlegierungen ist bislang nicht bekannt. Titanlegierungen verfügen hingegen über ausgezeichnete dichtetpezifische mechanische Eigenschaften bei gleichzeitiger hoher chemischer Beständigkeit, weswegen sie bevorzugt in der Luft- und Raumfahrt zum Einsatz kommen. Die mechanischen Eigenschaften, wie u.a. das Formänderungsverhalten, werden stark von der vorliegenden Mikrostruktur und Phasenzusammensetzung bestimmt. In diesem Zusammenhang unterscheiden sich die Kristallmodifikationen von  $\alpha$ -Titan (hexagonal) und  $\beta$ -Titan (kubisch-raumzentriert) deutlich. Einen Kompromiss bietet die Mischform  $\alpha + \beta$ -Titan, zu der die am weitesten verbreitete Titanlegierung Ti-6Al-4V gehört, die in vielen unterschiedlichen Bereichen von der Luft- und Raumfahrt- bis hin in der Medizintechnik Anwendung findet und daher bereits weitreichend erforscht ist.  $\alpha$ -Titanbasislegierungen werden unter anderem im Automobilbau, in der Medizintechnik und in Sportgeräten eingesetzt, weniger jedoch im Bereich der Luft- und Raumfahrt.

Im Rahmen dieser Arbeit wurde das Verhalten einiger Titan- $\alpha$ -Legierungen beim Warmkriechformen untersucht. Die Legierungen KS1.2ASNEX, Exhaust-XT® und ASTM Gr. 04 wurden insbesondere aufgrund ihrer hervorragenden Oxidationsbeständigkeit in erhöhten Temperaturen ausgewählt. Das Rücksprungverhalten von Titanlegierungen bei der Blechumformung stellt eine wesentliche Herausforderung dar, um maß- und formhaltige Bauteile herstellen zu können.

Da das Rücksprungverhalten temperaturabhängig ist, wurde das Verhalten bei verschiedenen Temperaturniveaus untersucht. Zur Entwicklung eines besseren Verständnisses des Werkstoffverhaltens beim Warmkriechformen, wurden eine Reihe von Faktoren variiert und auf ihren Einfluss hin analysiert. Die Zusammenhänge der signifikanten Faktoren wie Umformtemperatur, Erwärmungszeit, Kriechdehnung, Dehnungsrate und Relaxationszeit wurden mittels einer statistischen Versuchsplanung erarbeitet, auf deren Basis der Warmkriechformprozess optimiert wurde. Um den Einfluss weiterer Parameter wie der Reibungskoeffizient, die Matrizen- und die Niederhalterkraft zu analysieren und zur Prozessoptimierung zu nutzen, wurden Prozesssimulationen auf Basis der Finite-Elemente-Methode durchgeführt.

Basierend auf dem oben genannten Ansatz sind die Umformtemperatur und die Relaxationszeit die wichtigsten Faktoren, die das Oxidationsverhalten und die Eigenspannung beeinflussen. Die Legierung KS1.2ASNEX zeigt das günstigste Verhalten bei 650 °C mit einer Relaxationszeit von 720 s, sodass ein vollständiger Spannungsabbau ohne das Auftreten von unerwünschten Oxidschichten erreicht werden kann. Eine weitere Verbesserung der Ergebnisse durch Verringerung der Reibungskoeffizient

in Kombination mit Erhöhung der Niederhalterkraft lässt sich mit Hilfe der Simulation zeigen. Die experimentellen Versuche wurden von metallographischen Untersuchungen begleitet, die zur Bewertung der Prozess-Mikrostruktur-Eigenschaftsbeziehungen herangezogen wurden.

## Table of Contents

<b>List of figures</b> .....	<b>x</b>
<b>List of tables</b> .....	<b>xiii</b>
<b>Symbols</b> .....	<b>xiv</b>
<b>Abbreviations</b> .....	<b>xvi</b>
<b>1 Introduction</b> .....	<b>1</b>
<b>1.1 Overview of light metals applications in aerospace industry</b> .....	<b>1</b>
<b>1.2 Objective of the study</b> .....	<b>2</b>
<b>2 State of the art</b> .....	<b>4</b>
<b>2.1 Titanium and titanium alloys</b> .....	<b>4</b>
2.1.1 Industrial motives for using titanium alloys .....	4
2.1.2 Physical properties .....	5
2.1.3 Mechanical properties .....	5
2.1.4 Crystalline structure of titanium .....	6
2.1.5 Classification of titanium alloys .....	8
2.1.5.1 Alpha alloys .....	9
2.1.5.2 Beta alloys.....	10
2.1.5.3 Alpha-beta alloys.....	11
2.1.5.4 Titanium-aluminide alloys [LEYE03].....	13
2.1.5.5 Additive manufacturing methods in titanium .....	13
<b>2.2 Forming of titanium alloys</b> .....	<b>14</b>
2.2.1 General overview of forming methods [DOEG10].....	14
2.2.2 Sheet forming [DOEG10].....	14
2.2.2.1 Coefficient of friction $\mu_f$ .....	17
2.2.2.2 Springback effect.....	19
2.2.2.3 Anisotropy.....	20
2.2.3 Classification of forming according to temperature.....	22
2.2.4 Oxidation during hot forming .....	23
2.2.5 Superplastic forming .....	26
2.2.6 Hot creep forming .....	27
<b>2.3 Conclusion of the literature review</b> .....	<b>29</b>
<b>3 Experimental Procedure</b> .....	<b>30</b>
<b>3.1 Scientific objective of the study</b> .....	<b>30</b>
<b>3.2 Material selection</b> .....	<b>31</b>

3.2.1	KS1.2ASNEX .....	32
3.2.2	TIMET Exhaust XT® .....	32
3.2.3	ASTM Grade 04.....	33
<b>3.3</b>	<b>Material Characterization at room temperature (RT).....</b>	<b>33</b>
3.3.1	Tensile test at RT .....	33
3.3.2	Tensile test at elevated temperatures.....	36
3.3.3	Metallographic examination .....	36
3.3.4	Fatigue test at RT .....	38
<b>3.4</b>	<b>Parameter selection of hot creep forming .....</b>	<b>40</b>
3.4.1	Definition of the study.....	41
3.4.2	Design of the study.....	42
3.4.2.1	D-Optimal instead of Full-factorial design.....	42
3.4.2.2	Generating table of tests via D-optimal.....	43
3.4.3	Regression analysis and robustness test .....	44
<b>3.5</b>	<b>Numerical study of HCF .....</b>	<b>44</b>
3.5.1	Material definition in the simulation tool.....	45
3.5.1.1	Definition of mechanical properties .....	45
3.5.1.2	Definition of flow curves.....	46
3.5.1.3	Definition of anisotropy.....	47
3.5.2	Setting up the FE-model.....	49
3.5.3	Validation of FE-model with Swift® component .....	50
3.5.4	FE-study on an aerospace component .....	51
<b>3.6</b>	<b>Examination of the t-duct .....</b>	<b>52</b>
<b>3.7</b>	<b>Conclusion of the experimental procedure .....</b>	<b>52</b>
<b>4</b>	<b>Results and discussion .....</b>	<b>54</b>
<b>4.1</b>	<b>Tensile test at RT.....</b>	<b>54</b>
<b>4.2</b>	<b>Metallographic examination at RT.....</b>	<b>57</b>
4.2.1	Microstructure at RT .....	57
4.2.2	Texture at RT .....	58
4.2.3	Hardness at RT.....	59
<b>4.3</b>	<b>Fatigue test at RT.....</b>	<b>60</b>
<b>4.4</b>	<b>Tensile test at elevated temperatures .....</b>	<b>61</b>
<b>4.5</b>	<b>Metallographic examination at elevated temperatures .....</b>	<b>64</b>
4.5.1	Microstructure at elevated temperatures.....	64

---

4.5.2	Texture at temperature level (650°C).....	70
4.5.3	Hardness at elevated temperatures .....	72
<b>4.6</b>	<b>Statistical model for HCF on KS .....</b>	<b>72</b>
4.6.1	Screening phase.....	73
4.6.2	Refinement stage.....	76
4.6.3	Optimum stage .....	80
4.6.4	Statistical study on Gr.04.....	82
4.6.5	Statistical study on XT .....	84
4.6.6	HCF of Ti6AL4V .....	85
<b>4.7</b>	<b>Results of numerical study of HDD .....</b>	<b>87</b>
4.7.1	Setting up the material model .....	87
4.7.2	Validation of the simulation model.....	88
4.7.3	Optimization of the numerical frame conditions of HDD.....	89
<b>4.8</b>	<b>Realization of FE-results with real T-duct.....</b>	<b>96</b>
<b>4.9</b>	<b>Conclusion of the results .....</b>	<b>98</b>
<b>5</b>	<b>Summary.....</b>	<b>100</b>
<b>6</b>	<b>Outlook.....</b>	<b>103</b>
6.1	Uneven representation of micrographs .....	103
6.2	Brittleness at 500°C for ASTM Gr.04 and Exhaust-XT .....	104
6.3	Variation of coefficient of friction between die parts.....	104
<b>7</b>	<b>List of literature.....</b>	<b>105</b>
<b>8</b>	<b>Appendix.....</b>	<b>110</b>
	<b>Overview of all the fitted flow curves.....</b>	<b>110</b>

## List of Figures

Figure 2-1: USA titanium-tonnage over years, courtesy of Lütjering et al. [LÜTJ07].....	5
Figure 2-2: Lattice structure in metals [WEIß07] .....	6
Figure 2-3: Lattice structure of titanium in both phases [LEYE03] .....	7
Figure 2-4: Isomorphous titanium phase diagram [DONA00] .....	9
Figure 2-5: Microstructure of Ti6Al4V according to heat treatment condition [LEYE03] .....	12
Figure 2-6: $\alpha$ - $\beta$ -alloys applications in a civilian airplane [SANA20] .....	13
Figure 2-7: Stress-strain and flow curves with tensile stress [DOEG10].....	15
Figure 2-8: Deep drawing tool [DOEG10].....	16
Figure 2-9: Tribology of contact areas [DOEG10] .....	18
Figure 2-10: Springback angle over forming temperature for ASTM Gr.02 [OZTU10].....	20
Figure 2-11: Relationship between mean normal anisotropy and LDR [DOEG10].....	21
Figure 2-12: Springback within the deep drawing of Ti6Al4V sheet [ODEN10] .....	23
Figure 2-13: Stages of oxide scale formation [LEYE03]. .....	24
Figure 2-14: Formation of $\alpha$ -case on the microstructure of Ti6Al4V surface.....	25
Figure 2-15: Superplastic forming mechanism, courtesy of W. Beck in [LEYE03] .....	26
Figure 3-1: Flow chart to the design of the study .....	30
Figure 3-2: Dog-bone sample for the tensile test at RT, (values in mm). .....	34
Figure 3-3: Tensile sample with strain gauges.....	35
Figure 3-4: Forming dilatometer type Gleeble <sup>®</sup> 3500.....	36
Figure 3-5: Fatigue test sample [DIN EN 6072-2011].....	38
Figure 3-6: Gnedenko method and ansatz to build the Wöhler curve, according to [PFAL13] .....	40
Figure 3-7: Schematic description of HCF .....	41
Figure 3-8: Full factorial design against a composite design. ....	42
Figure 3-9: D-optimal design derived from full factorial one, Courtesy of Erikssen [TREI08] .....	43
Figure 3-10: Definition of mechanical properties in the simulation tool, screenshot Simufact.forming.....	45
Figure 3-11: Definition of flow curve in the simulation tool.....	47
Figure 3-12: Definition of anisotropy in the simulation tool.....	49
Figure 3-13: Tree of the simulation model setup, screenshot from Simufact.forming. ....	50
Figure 3-14: Swift <sup>®</sup> component.....	51

Figure 3-15: Half-shell of a t-duct, Courtesy of FormTech GmbH .....	52
Figure 4-1: Stress-strain curves at RT .....	55
Figure 4-2: Elongation to fracture and $r_m$ -value depending on the angle to the rolling direction. Values for Ti6Al4V: courtesy of [BADR16]. .....	56
Figure 4-3: Microstructure of titanium alloys at RT, scale: (100 $\mu\text{m}$ ) and (20 $\mu\text{m}$ ) .....	57
Figure 4-4: Pole figures and inverse pole figures [001] of the studied alloys at RT. ....	59
Figure 4-5: Wöhler curve for KS according to Gnedenko at RT. ....	60
Figure 4-6: Stress-strain curves at elevated Temperatures for KS, Gr.04, XT, and Ti6Al4V. .	62
Figure 4-7: Microstructure of KS at elevated temperature. ....	65
Figure 4-8: Microstructure of Gr.04 and XT at elevated temperatures. ....	65
Figure 4-9: SEM for KS at 800°C, recognition of $\text{Ti}_x\text{O}_x$ phase at the surface. ....	66
Figure 4-10: Volume fraction of $\beta$ -phase of Ti6Al4V depending on the temperature.....	67
Figure 4-11: Shape of Oxide scale at 800°C for the studied alloys. ....	68
Figure 4-12: Effect of usage a protective gas on the formation of superficial Oxide layer at 800°C. ....	69
Figure 4-13: $\alpha$ and $\beta$ distribution for Ti6Al4V in dependence on forming temperature.....	70
Figure 4-14: Pole figures of KS and Ti6Al4V at RT and 650°C (RD:A1 & TD:A2).....	70
Figure 4-15: Inverse pole figures on plane (RD-TD) for KS and Ti6Al4V at RT and 650°C. .	71
Figure 4-16: Stress relaxation curves for KS in dependence on temperature level. ....	73
Figure 4-17: Scatter plot for residual stress depending on relaxation time in screening stage. .	75
Figure 4-18: Presence of $\alpha$ -case layer according to variation of HCF conditions for KS. ....	78
Figure 4-19: Pareto effect of parameters on the results of refinement stage for KS. ....	80
Figure 4-20: Phenomenon of $\alpha$ -case within the optimum stage for KS. ....	81
Figure 4-21: Stress relaxation curves for Gr.04 in dependence on temperature level. ....	82
Figure 4-22: Appearance of $\alpha$ -case positions for Gr.04 at 600 and 700°C. ....	83
Figure 4-23: Oxide scale and $\alpha$ -case layer for Gr.04 at 800°C. ....	84
Figure 4-24: Stress relaxation curves for XT in dependence on temperature level. ....	85
Figure 4-25: Microstructure of superficial $\alpha$ -case for XT at different temperature levels. ....	85
Figure 4-26: Relaxation curves for Ti6AL4V in dependence on temperature level. ....	86
Figure 4-27: Micrographs of Ti6AL4V with oxide observation at 800°C. ....	86
Figure 4-28: Flow curve fitted according to Hensel-Spittel-Ansatz for KS at 650°C. ....	87
Figure 4-29: Thickness comparison between numerical and experimental forming of Swift. .	88
Figure 4-30: Shapes of blank for the FE-study to form a t-duct. ....	90

Figure 4-31: FE-comparison between the quality of critical positions after HDD on $\alpha$ -alloys. .....	91
Figure 4-32: FE-comparison between square and disc for KS at 730°C.....	92
Figure 4-33: FE-comparison of thickness distribution between square and trapezium for KS at 730°C. ....	92
Figure 4-34: FE-comparison of material flow between square and trapezium for KS at 730°C. .....	93
Figure 4-35: Effect of FT-contour, $\mu_f$ and $F_{bh}$ on the thickness distribution and effective stress for KS at 650°C. ....	94
Figure 4-36: FE-comparison for HDD of KS and Ti6Al4V with the best parameters.....	94
Figure 4-37: FE-study with Hill and Barlat stress state criterion for KS at 650°C.....	95
Figure 4-38: Thickness of the critical curve of half-shell manufactured by FormTech® according to suggested parameters. ....	96
Figure 4-39: Samples from t-duct half-shell of KS for metallographic examination. ....	97
Figure 4-40: Micrographs of positions from t-duct half-shell fabricated by FormTech based on suggested parameters within this study.....	98
Figure 5-1: Schematic representation of all the results of the approach. ....	102
Figure 6-1: Uneven representation of microstructure for similarly prepared samples.....	103
Figure 6-2: Unexpected brittleness at 500°C for XT. ....	104
Figure 8-1: Fitted flow curve at 400°C for Gr.04. ....	110
Figure 8-2: Fitted flow curve at 500°C for Gr.04. ....	110
Figure 8-3: Fitted flow curve at 600°C for Gr.04 ....	111
Figure 8-4: Fitted flow curve at 700°C for Gr.04. ....	111
Figure 8-5: Fitted flow curve at 800°C for Gr.04. ....	112
Figure 8-6: Fitted flow curve at 400°C for KS. ....	112
Figure 8-7: Fitted flow curve at 500°C for KS. ....	113
Figure 8-8: Fitted flow curve at 600°C for KS. ....	113
Figure 8-9: Fitted flow curve at 700°C for KS. ....	114
Figure 8-10: Fitted flow curve at 800°C for KS. ....	114
Figure 8-11: Fitted flow curve at 400°C for XT. ....	115
Figure 8-12: Fitted flow curve at 500°C for XT. ....	115
Figure 8-13: Fitted flow curve at 600°C for XT. ....	116
Figure 8-14: Fitted flow curve at 700°C for XT. ....	116
Figure 8-15: Fitted flow curve at 800°C for XT. ....	117

**List of Tables**

Table 1-1: Price of some famous titanium alloys, year of investigation: 2016. ....	2
Table 2-1: Mechanical properties of some titanium categories at room temperature [DONA00] .....	6
Table 2-2: Slip systems in dependence on structure type [LEYE03].....	7
Table 2-3: Chemical composition of the most common cp-Ti alloys [DONA00].....	10
Table 3-1: Chemical composition of the regarded alloys within the study, by means of an optical spectroscopy. ....	32
Table 3-2: Main properties of the regarded alloys within the study. ....	33
Table 3-3: Mechanical properties of the regarded alloys within the study at RT. ....	33
Table 3-4: Classification of grain size [MACH11]. ....	37
Table 3-5: Factors and outputs of the study.....	41
Table 3-6: Scientific and practical outputs of the simulation study. ....	44
Table 3-7: Forming parameter set of swift <sup>®</sup> , Data provided by FormTech.....	51
Table 4-1: Mechanical properties at RT .....	56
Table 4-2: G-index at RT according to ISO 643.....	58
Table 4-3: Hardness number for all the studied alloys according to Vickers at RT. ....	59
Table 4-4: Mechanical properties obtained from tensile test at elevated temperatures. ....	63
Table 4-5: R <sub>m</sub> -Value at elevated temperatures obtained according to ISO 10113.....	64
Table 4-6: G-index at elevated temperatures .....	69
Table 4-7: Hardness number according to Vickers at 800°C for the studied alloys.....	72
Table 4-8: Stress relief recorded after the screening phase for KS.....	74
Table 4-9: Term significance out of regression analysis after screening stage for KS, $\alpha=0.1$ . ....	76
Table 4-10: Results recorded after refinement stage for KS.....	77
Table 4-11: Term significance out of regression analysis after refinement stage for KS. ....	79
Table 4-12: Predicted values of the significant parameters after refinement stage for KS. ....	80
Table 4-13: Results after test series of optimum stage for KS.....	82
Table 4-14: FE- study approach to form a t-duct.....	91
Table 4-15: The best parameters to manufacture an exhaust component for aerospace applications from titanium $\alpha$ -alloys obtained at the end of this dissertation. ....	99
Table 8-1: Fitted parameter of the flow curves according to Hensel/Spittel Ansatz. ....	117

**Symbols**

<i>Symbol</i>	<i>Description</i>	<i>Unit</i>
A	Instant cross section area	mm <sup>2</sup>
A <sub>0</sub>	Original cross section area	mm <sup>2</sup>
b <sub>0</sub>	Original material width	mm
b <sub>1</sub>	Instant material width	mm
C	Material consistency in the simulation tool	
E	Elastic modulus of material	GPa
ELI	Extra low interstitials	
γ	Intermetallic compound TiAl	
K <sub>f</sub>	True (flow) stress	MPa
L	Instant length of measuring part of specimen	mm
L <sub>0</sub>	Original length of measuring part of specimen	mm
m	Yield loci exponent	
M <sub>f</sub>	Temperature of end formation of martensite	°C
M <sub>s</sub>	Temperature of start formation of martensite	°C
N	number of cycles to fracture	
R	Stress ratio	
R <sub>a</sub>	Arithmetic mean roughness	
r <sub>m</sub>	Mean normal anisotropy term	
R <sub>m</sub>	Ultimate strength	MPa
R <sub>p0.2</sub>	0.2% proof stress	MPa
S	Stress amplitude	MPa
S <sub>0</sub>	Original material thickness	mm
S <sub>1</sub>	Instant material thickness	mm
β <sub>0max</sub>	Limit drawing ratio	

<i>Symbol</i>	<i>Description</i>	<i>Unit</i>
T	Forming temperature	°C
T <sub>m</sub>	Melting point	°C
t <sub>r</sub>	Relaxation time	s
T <sub>rec</sub>	Recrystallization temperature	°C
T <sub>s</sub>	Scatter band	
α	alpha	
α <sub>2</sub>	Intermetallic compound Ti3AL	
β	Beta phase	
Δr	Planar anisotropy term	
ε	Engineering strain	[mm/mm]
ε̇	Strain rate	s <sup>-1</sup>
ε <sub>B</sub>	Elongation to fracture	[mm/mm]
ε <sub>gl</sub>	Uniform elongation	mm/mm
σ	Engineering stress	MPa
σ <sub>D</sub>	Fatigue stress	MPa
σ <sub>pl</sub>	Plasticity strength	MPa
σ <sub>ult</sub>	Ultimate strength	MPa
σ <sub>xx</sub> , σ <sub>yy</sub> , σ <sub>xy</sub>	Principal plane stress	MPa
φ	True strain	
φ	Error factor	

**Abbreviations**

<i>Abbreviation</i>	<i>Description</i>	<i>Unit</i>
Al	Aluminum	
AM	Additive manufacturing	
bcc	Base-centered cubic	
c/a	ideal ratio for plastic deformation	
CAF	Creep age forming	
cp	commercially pure	
Cr	Chromium	
Cu	Copper	
D <sub>0</sub>	Blank diameter	mm
d <sub>0</sub>	Punch diameter	mm
DIN	Deutsches Institut für Normierung	
EBM	Electron beam melting	
EBSD	Electron back scattering diffraction	
EDX	Energy dispersive x-ray	
equ.	equation	
F	Force	N
F <sub>bh</sub>	Blank holding force	kN
fcc	Face-centered cubic	
FEM	Finite element method	
FFF	Fused filament fabrication	
F <sub>p</sub>	Punch force (forming force)	kN
HCF	Hot creep forming	
hcp	Hexagonal close-packed	
HDD	Hot deep drawing	
IPF	Inverse pole figure	

<i>Abbreviation</i>	<i>Description</i>	<i>Unit</i>
ISO	International Standardization Organisation	
LBM	Laser beam melting	
LDR	limit drawing ratio	
Mo	Molybdenum	
Nb	Niobium	
Pa	Pallium	
PF	Pole figure	
$r_d$	Die edge radius	mm
RD	Rolling direction	
RMS	Response methodology stage	
$r_p$	Punch edge radius	mm
RT	Room temperature	°C
SEM	Scanning electron microscope	
Si	Silicon	
SLM	Selective laser melting	
Sn	Tin	
SPF	Superplastic forming process	
SR	Stress relief	
TD	Transverse direction	
US	Ultimate (tensile) strength	MPa
V	Vanadium	
W	Tungsten	
WDX	Wavelength dispersive x-ray	
YS	Yield strength	MPa
Zr	Zirconium	



## 1 Introduction

### 1.1 Overview of light metals applications in aerospace industry

Economic background in many domains is the main motive to let the development wheel rotate, while in others, the ecological reasons have priority over any achievement. Some industrial fields demand both economic and ecological needs to be fulfilled and set these as must requirements to accept the output of the manufacturing process. The aviation industry is a representative example of such fields. Many fabricating methods have recently been used to produce light metal parts for aircraft. Forming, in general, belongs to the most widespread methods in this domain. There, specific mechanical properties are needed in parallel with fulfilling the low manufacturing expenses and other environmental demands. Formability and strength are the most interesting material properties to be observed and developed. So far, the matter of applying the lightweight principle in the aerospace field has risen drastically and enables deploying light materials like the three essential nonferrous metals; magnesium, aluminum, and titanium.

The American aviation community has started using magnesium alloys to fabricate some aeronautical parts as the lightest metal with industrial applicability [GWYN07]. A well-known magnesium alloy in this field is AZ91. Owing to the low density, magnesium alloys have been utilized in Boeing 727 since 1962 to manufacture non-structural components like engine gear boxes and power generation components. However, its corrosion behavior and restricted strength are big issues limiting its application in this kind of industry. Aluminum alloys also became a convenient substitute for steel as a lighter metal with desired material properties. With respect to strength and formability, aluminum alloys are good in both structural and body parts [ISMA16]. Some alloys exhibit a high strength after heat treatment, like 2xxx, 6xxx, and 7xxx families, while others are not as hardenable as the aforementioned ones. They own, however, superior formability even at room temperature. 5xxx alloys are an example of this category [ISMA16] and [JAMB02]. Besides good formability, the latter alloy system exhibits good weldability and high corrosion resistance. Springback is an essential matter in aluminum alloys that makes manufacturing parts via forming aluminum sheets challenging and prompts new heat treatment techniques to avoid or at least minimize it completely. Aluminum still, in all cases, makes up approximately 70% of the aircraft in A380, for instance, according to a study released by [LEYE03].

Titanium alloys have also found use in the aerospace industry for more than 40 years. Their distinguished material properties admit them to be favorable to manufacture many airplane

components over aluminum alloys, especially resistance to heat and corrosion [GERS05]. They possess a high strength-to-weight ratio, and their mechanical properties can be compared to many steel alloys. [LEYE03] describes the benefit of using titanium alloys in the aerospace industry over other metals despite its high price. It is lighter than steel and nickel, able to be applied in higher temperatures than aluminum alloys and exhibits higher corrosion resistance than aluminum alloys as well as low-alloyed steels. It became favorable in some engine components, such as plugs and nozzles, to replace nickel-based alloys saving weight in engines where the temperature could reach 600°C [FIOR15]. Indeed, it can be attributed to the standard material of airplane engines. The behavior of titanium alloys regarding high-temperature applications differs according to the chemical composition and the alloying elements. However, the cost of the semi-finished component also plays a role in choosing the alloy to apply. Table 1-1 represents an example of some titanium alloys and their expense.

<b>Titanium alloy</b>	<b>Price [€/kg]</b>
Innovative $\alpha$ -alloys	40-60
ASTM Gr.02	$\approx 50$
ASTM Gr.04	60 – 120
Ti3Al2.5V	100
Ti6Al4V	150-200
Ti6242	160-200

*Table 1-1: Price of some famous titanium alloys, year of investigation: 2016.*

In this study, we are deeply treating an experimental approach to describe the behavior of some titanium alloys during hot forming and the resulting anticipated properties both during fabrication and operation. The hot forming stage and the optimization of its parameters are also of high importance within this study.

## **1.2 Objective of the study**

Titanium alloys usually have excellent mechanical and chemical properties with a favorable specific weight, which is why they are preferably used in the aerospace industry, also despite the high material costs. Former Studies released profound investigations about the usage of titanium alloys in the aerospace industry and brought two titanium alpha-beta alloys into prominence, namely Ti6Al4V and Ti6Al2Sn4Zr2Mo (briefly Ti64 or Ti6242). The characteristic of both alloys will be profoundly explained in the literature review. The mechanical properties, especially the deformation behavior in sheet metals, are largely

determined by the existing microstructure. The crystal modifications of different titanium alloys impact their material properties and, hence, their suitability to apply in one environment or another.

This work aims at developing the fabrication of alpha titanium alloys, which are mainly used in automotive engineering, sports equipment, and biomedical components, to find a use in the aviation industry in order to avail their good characteristics over the aforementioned alpha-beta alloys, i.e., in-depth examinations and characterizations should investigate whether alpha titanium alloys are also suitable for the aerospace industry as good and enough as the already used titanium alloys.

On the other hand, the manufacturing process, especially the forming process, poses challenges highlighted in the dissertation. One of the most faced challenges is the springback effect. For this reason, solutions should be sought. The essential manufacturing method which should be considered intensively here is hot deep drawing. With the aid of a statistical model, real forming processes, and an accompanying numerical simulation, the study is expected to achieve its objective. For this purpose, methods of statistical test planning are used here.

The examined parameter field is characterized by suitable test procedures and analysis methods, and the desired process window is to be derived from this. In addition to basic scientific questions of deformation and strength behavior, the transferability of the research results to manufacturing practice and industrial application is one of the major goals of the study. Therefore, the objective of this work can be concluded into two main points:

- Investigation of some titanium alpha alloys at elevated temperatures to secure their utilization in high-temperature applications.
- Optimization of the hot forming stage to facilitate the usage of titanium alpha alloys in the aerospace industry.

## 2 State of the art

### 2.1 Titanium and titanium alloys

Titanium is the ninth most abundant element on Earth. It was discovered as mineral oxides, which took their name mostly according to the place of the first appearance. At the end of the 18th century, people started finding rutile ( $\text{TiO}_2$ ) and ilmenite ( $\text{TiFeO}_3$ ), which later became the main source of purified titanium. Indeed, the actual production of titanium was in the very first decades of the 20th century [POLM17]. Titanium slag was made from ilmenite in Australia, Canada, Norway, and the Republic of South Africa [DONA00].

In Russia and the United States, titanium sponge production started, and they provided it to the world. In the middle of the 20<sup>th</sup> century, the real industrial use of titanium alloys was established, especially in the United Kingdom, and released were some important titanium alloys to find a specific industrial use [LÜTJ07].

#### 2.1.1 Industrial motives for using titanium alloys.

Several industrial fields have adopted titanium since the development of its alloys, owing to its unique specific strength and excellent corrosion resistance. This makes it a favorable metal in fields, where there are corrosive environments, such as aerospace engines and the human body [DONA00]. However, military applications were the first stimulus to admit titanium alloys into the industrial society. SR71 serves as the first use of titanium beta alloys in the aerospace structure. In figure 2-1, the USA titanium manufacturing tonnage over the years is displayed. Reports from Russia demonstrate the exclusive usage of titanium alloys in the military before 1967 [LÜTJ07]. Prof. Lütjering et al. also observed the development of the industrial applications of titanium alloys over the years in both Russia and Japan, which shows a noteworthy advancement in the usage of titanium alloys in other domains as military, so that at the end of the 20th century, some medical, household, and automobile components became of titanium. However, its high price is still a matter of second thought in such industrial applications [NEUG06]. Another point of view to using titanium alloys is the compatibility to adhere composite materials. Usage of the latter materials is increased industrially, which nominates titanium upon steel and aluminum to be a partner of composite parts owing to the very convenient thermal expansion difference and very low contact corrosion between both materials [TAKA20], [STUT14].

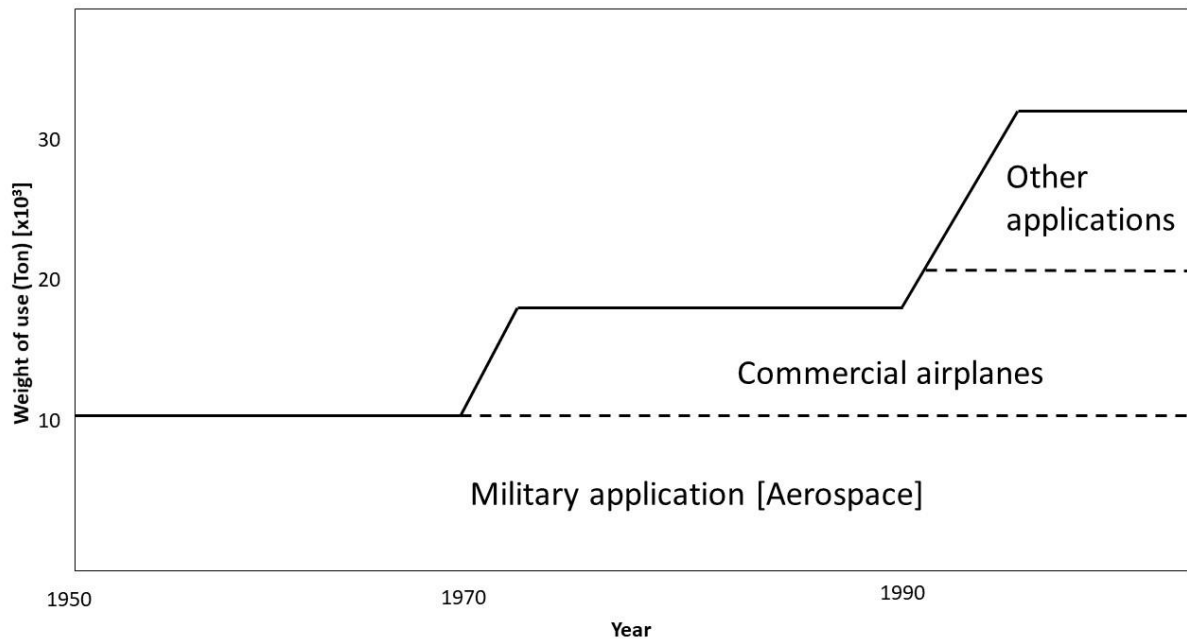


Figure 2-1: USA titanium-tonnage over years, courtesy of Lütjering et al. [LÜTJ07]

### 2.1.2 Physical properties [LEYE03].

Titanium is the heaviest light metal, which finds use in the industry. It has a density of  $4.51 \text{ [g/cm}^3\text{]}$  (ca. 60% of steel or nickel-base alloys) with an atomic number of 22 and an atomic weight of 47.9. It looks nearly dark grey (darker than aluminum). Its melting point amounts to  $1670 \text{ }^\circ\text{C}$  (1940 K), thermal conductivity is ca.  $11.4 \text{ [W/m. K]}$ , and it exhibits at ambient temperature a specific heat of  $0.5223 \text{ [kJ/kg]}$ . Another important physical property of titanium to be mentioned is its electrical conductivity, which amounts to 0.03 IACS (3% of copper)

### 2.1.3 Mechanical properties

Since many features impact the mechanical properties of each material, especially the temperature in which they are measured and the chemical composition of the alloy, it is not possible to cover all the mechanical properties in the whole titanium alloy spectrum in one section. In order to obtain a rough idea about the mechanical behavior, a short overview of the essential mechanical properties at room temperature will be given in table 2-1 below.

It might be noteworthy to stress the statement that these values were estimated at room temperature and on average. Alloying titanium (even in tiny amounts) plays a major role in the mechanical properties. More about this matter will be illustrated in chapter 2.1.5.

Property	Value [Range] and unit	Category
Hardness	150-200 [HV0.5]	alpha alloys
	Min. 250 [HV0.5]	[not heat-treated alpha-beta alloys]
	Min. 400 [HV0.5]	Heat-treated alpha-beta alloys
Tensile strength	250-750 [MPa]	Alpha alloys (alloying makes difference)
	Up to 950 [MPa]	Not heat-treated alpha-beta alloys
	Over 1100 [MPa]	Heat-treated alpha-beta alloys
Young's modulus	Ca. 120 [GPa]	Variation according to temperature

Table 2-1: Mechanical properties of some titanium categories at room temperature [DONA00]

### 2.1.4 Crystalline structure of titanium

Understanding the lattice structure of the crystalline material is a basic step to conceiving the material behavior, thus the material properties in accordance with the lattice structure. Formability (in our case, specifically drawability) is heavily influenced by the microstructure. Therefore, it is important to classify the type of structure arising during forming. Generally, the common lattice structures found in metals are (Figure 2-2):

- Face-centered cubic lattice [fcc],
- Base-centered cubic lattice [bcc] and
- Hexagonal close-packed lattice [hcp].

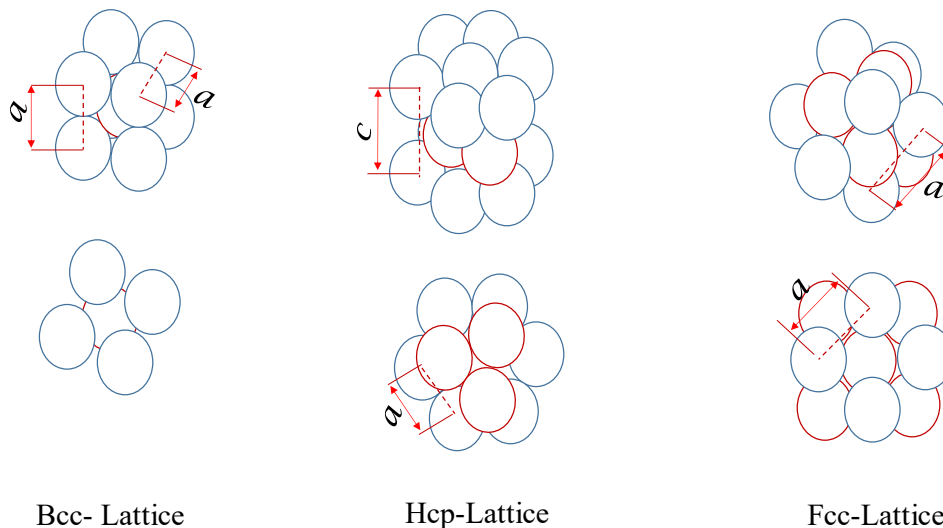


Figure 2-2: Lattice structure in metals [WEIβ07]

The characteristic of material deformation depends on a movement among the atoms called slip. Slip plane and Slip direction are the plane and direction with higher dense packed atoms. To describe the lattice well, the number of dislocation glide opportunities is called the slip system, which is the product of the number of slip planes and slip directions [LEYE03]. There are different numbers of slip planes, slip directions and the resulting slip systems in the metal structure. In this context, both the fcc and bcc lattice have 12 slip systems, while the hcp lattice exhibits only 3 slip systems. Table 2-2 illustrates the main parameters of each lattice structure. This difference is the reason for the poor formability of materials with a hexagonal versus face-centered lattice structure, whereas the minimum required independent slip systems to achieve homogeneous plastic deformation is 5 [LEYE03].

Structure type	Slip planes	Slip directions	Slip systems
hcp	[0001]: one basal plane	112̄0: three directions	1x3 = 3
bcc	[110]: six prismatic planes	111: two directions	6x2 = 12
fcc	[111]: four prismatic planes	110: three directions	4x3 = 12

Table 2-2: Slip systems in dependence on structure type [LEYE03]

Titanium can crystalize in different crystal structures. At a temperature of about 875 °C (varies in dependence upon the alloy), pure titanium undergoes while cooling a structural allotropic transformation from “bcc” to “hcp” lattice [KULP03]. The former is called beta structure (hereafter  $\beta$ ), while the latter is called alpha one (hereafter  $\alpha$ ). The temperature at which this allotropic transformation takes place is called the beta transus temperature, i.e., above this temperature, the  $\beta$ -phase is stable, and below it, the  $\alpha$ -phase. Figure 2-3 shows both.

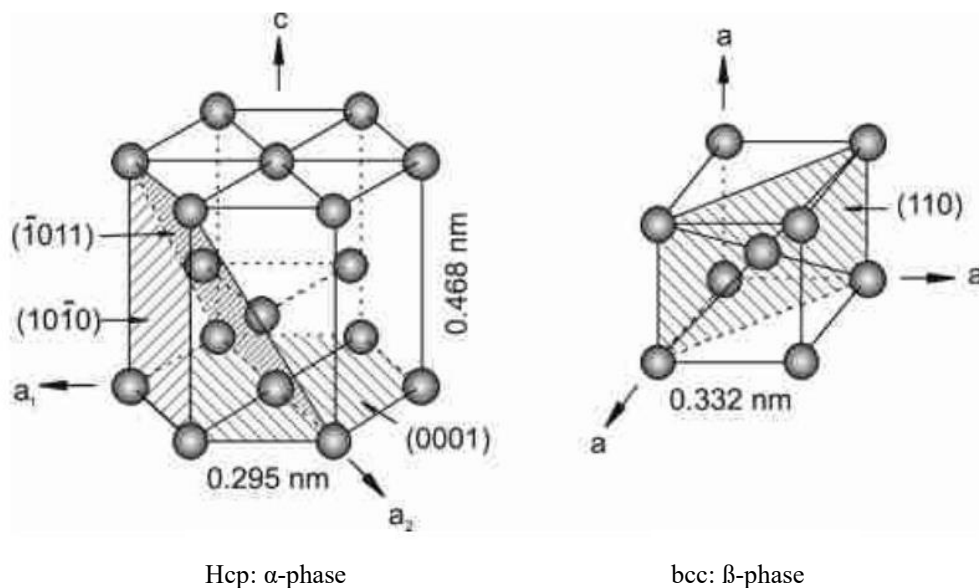


Figure 2-3: Lattice structure of titanium in both phases [LEYE03]

As seen in the  $\alpha$ -phase, the lattice parameters are [a] and [c]. In order to obtain good formability, a ratio  $c/a = 1.633$  is defined as the ideal ratio for plastic deformation of HCP [LIU01].  $\alpha$ -phase exhibits an hcp lattice structure with  $c/a = 1.587$  [LEYE03]. This is the reason for the poor formability of  $\alpha$ -titanium alloys in cold environments. Alloying can, however, manipulate this ratio and improve the cold formability of titanium alloys. Contrary to this, titanium  $\beta$ -phase with its bcc lattice has only one parameter [a], which presumes in the case of  $\beta$ -phase the value  $a = 0.332$ . The typical transformation of slip planes corresponding to the bcc to hcp transformation is given by the **Burger** relationship:

$$\begin{aligned} & \{0001\}_{\alpha} // \{110\}_{\beta} \\ & \langle 1120 \rangle_{\alpha} // \langle 111 \rangle_{\beta} \end{aligned}$$

In the case of cold forming, slip system and deformation twinning are the two plastic deformation mechanisms encountered in the material deformation of the hcp structure. Basal, prismatic, and pyramidal slip systems are inclined with [112-0] Burgers' vector, while a pyramidal slip system is inclined with [112-3] Burgers' vector [LIU01] et al.

### 2.1.5 Classification of titanium alloys

As mentioned before, titanium is an allotropic element which exhibits more than one crystallographic form. Titanium alloys are therefore categorized into four types. They are generally called:  $\alpha$ -Alloys, near  $\alpha$ -alloys,  $\alpha$ - $\beta$ -alloys and the metastable  $\beta$ -alloys. The name of each category corresponds to the phase arising at room temperature or the higher volume fraction [LEYE03]. There are alloying elements that enhance stabilizing  $\alpha$ -phase rather nearly up to  $\beta$ -transus. They are called  $\alpha$ -stabilizers. Other elements cause the  $\beta$ -phase to exist at the ambient temperature, the so-called  $\beta$ -stabilizers. Thus, the relationship  $\alpha$  to  $\beta$  stabilizers determines the volume fraction of each phase at the end of treatment. Figure 2-4 describes the distribution of titanium alloys corresponding to the content of  $\beta$ -stabilizers in each alloy and shows some well-known industrial alloys for the categories [DONA00].

The most common  $\alpha$ -stabilizers are aluminum, oxygen, and nitrogen. On the other hand, vanadium, molybdenum, iron, and copper are typical  $\beta$ -stabilizers. Zirconium and tin have a high solid solubility in both phases and serve as strengthening elements. Silicon is also known as an alloying element of titanium to develop creep resistance. This element promoted in the very current studies a profound investigation to have its suitable amount specified in order to develop the creep resistance. [LEYE03] assigned to silicon content in titanium alloy up to 0.1 wt. %, while recently, [MANT20] and [ANTT20] observed the silicon content in an important

$\alpha$ - $\beta$ -alloy and recommended 0.09 and 0.07 wt. % respectively. In the coming section, the main characteristics of each category will be addressed.

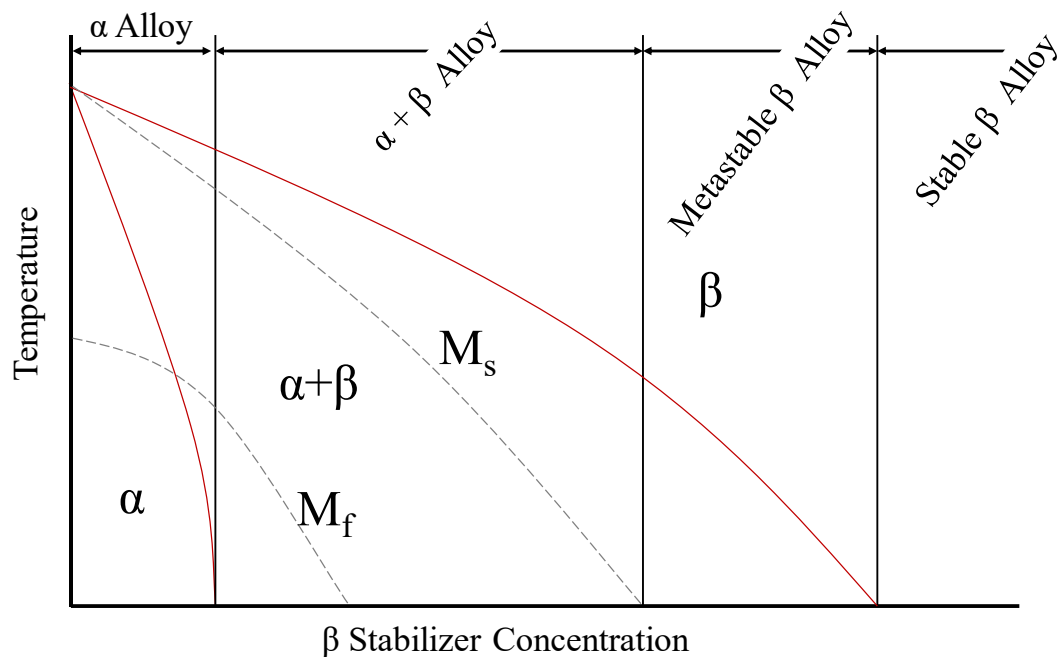


Figure 2-4:  $\beta$ -Isomorphous titanium phase diagram [DONA00]

### 2.1.5.1 Alpha alloys

This category includes a subcategory called commercially pure titanium [cp]. It is pure titanium with the addition of a tiny number of elements to improve its mechanical properties. Such alloying elements can be added interstitially, as oxygen and nitrogen, or substitutionally, like niobium (Nb), silicon, or iron. Oxygen is the most decisive element in this subcategory, owing to the fact that its content determines the strength of the alloy proportionally [BEAL06]. An amount between 0.1 – 0.4 wt. % is experimentally denoted for this element. However, oxygen content at elevated temperatures makes the operation very challenging and calls for special attention [LEE20]. [PATA01] observed a high oxygen solubility in titanium, up to 34%, during high-temperature exposure forming a surface-hardened zone (called in the scientific community oxygen scale). This layer seems to be hard and very brittle and downscales the mechanical properties or even results in a permanent failure in high temperatures [CASA20]. Therefore, it should be either prevented from forming by heating under a protective ambience or removed after hot treating via machining or pickling processes. For this reason, oxygen content in cp titanium should not exceed 0.6 wt. % and, thus, cp titanium alloys have been graded according to their oxygen content, see table 2.3. The most used alloy within this subcategory is cp Gr.02 [ASTM Gr.02]. Obviously, cp Gr.04 has higher strength than others, while cp Gr.01 possesses the highest ductility [LEYE03] and [HARA14]. Cp titanium alloys are mostly used in corrosive

as well as high-temperature environments, where these come in the first place and strength is not of high value. Another favorable property of these alloys is their weldability. On the other hand, anisotropy is a general feature arising from the cold forming of  $\alpha$ -alloys, which implies modest cold formability of this type of alloy compared to  $\beta$ -alloy [JURE13]. Table 2-3 shows merely these four alloys. However, other important cp titanium alloys relevant to this work will be discussed in the experimental procedure, section 3.2.

Cp alloy [ASTM]	Chemical composition ma.% max.						Tensile properties [MPa]		Elongation [%]
	C	H	O	N	Fe	others	YS [min]	US [min]	Min.
Gr.01	0.1	0.015	0.15	0.03	0.2	0.1	200	250	25
Gr.02	0.1	0.015	0.25	0.03	0.03	0.3	300	350	20
Gr.03	0.1	0.015	0.35	0.05	0.3	--	400	440	18
Gr.04	0.1	0.015	0.4	0.05	0.5	--	480	500	20

Table 2-3: Chemical composition of the most common cp-Ti alloys [DONA00]

The other subcategory of  $\alpha$ -alloys comprises alloys with a large amount of  $\alpha$ -stabilizers and a very low concentration of  $\beta$ -stabilizers. They are also preferable for high-temperature and cryogenic applications. Ti5Al2.5Sn is a famous  $\alpha$ -alloy in such applications with low interstitial elements (ELI).  $\alpha$ -alloys, in general, cannot be strengthened by heat treatment. The only benefit of heat treatment on these alloys is the annealing or recrystallization to remove the residual stresses [DONA00] and [BEAL06]. Strengthening via heat treatment basically depends on microstructural changes during phase transformation. This is restricted to grain refinement in the case of titanium  $\alpha$ -alloys. However, alloying of  $\alpha$ -alloys with a small amount of  $\beta$ -stabilizers could enhance the microstructural change and cause the material to be strengthened by grain size conveniently. An example of such  $\alpha$ -alloys with a small volume fraction of  $\beta$ -phase at room temperature is Ti8Al1V1Mo. This alloy possesses higher strength than typical  $\alpha$ -alloys. For this reason, they are also categorized as near-alpha alloys [BEAL06]. Zirconium has been observed in [YUE19] as a  $\beta$ -stabilizer added to near  $\alpha$ -alloys and considered a strengthened element due to the precipitation of (Ti, Zr)<sub>6</sub>.

### 2.1.5.2 Beta alloys

When the amount of  $\beta$ -stabilizers is quite sufficient to drive the  $\beta$ -transus nearly to room temperature, then the alloy is called  $\beta$ -alloy or metastable  $\beta$ -alloy.  $\beta$ -alloys are characterized by

their high ability to be strengthened by heat treatment. Due to the cooling mechanism, the microstructure can be shaped into either thin sections (air cooling) or thick sections (water quenching).  $\beta$ -alloys can retain in the solution-treated condition a 100%  $\beta$ -phase and, hence, they are distinguished for cold forming. Ti15V3Sn3Cr3Al, for instance, is formed almost exclusively at room temperature [BEAL06]. However, its formability decreases at elevated temperatures, owing to the  $\alpha$ -precipitation in high temperatures. Therefore, it should be overaged before being formed at a high temperature. Another feature to make  $\beta$ -alloys unpreferable at high temperatures is the bad creep resistance there, which corresponds to the bad creep resistance of the bcc structure due to a larger number of independent slip systems than the hcp one [MANT20].

### 2.1.5.3 Alpha-beta alloys

The most widely used category of titanium alloys. Contrary to both previous categories, none of  $\alpha$  and  $\beta$  phases is predominating in the microstructure at room temperature, whereas  $\beta$  volume fraction ranges between 5-40% depending on the amount of  $\beta$ -stabilizers and their content as well as the process conditions [LEYE03] and [DONA00]. Owing to this fact,  $\alpha$ - $\beta$ -alloys can retain a significant  $\beta$ -volume fraction at room temperature, which means they can be strengthened by solution treating. The latter process occurs upon  $\beta$ -transus followed by quenching with water, oil, or another soluble quenchant. The hardenability of this type of alloy is heavily dependent on the percentage of  $\beta$ -stabilizers. The microstructure of  $\alpha$ - $\beta$  alloys is influenced by heat treatment conditions and plays a major role in their mechanical properties. Cooling from the  $\beta$ -phase (above  $\beta$ -transus) field results in a so-called lamellar microstructure, while recrystallization causes the microstructure to be equiaxed [LEYE03]. The latter process generally occurs after manufacturing processes, like deformation or aging. As soon as the temperature goes below the  $\beta$ -transus,  $\alpha$ -starts nucleating at grain boundaries and propagates as lamellae into  $\beta$ -grains. In addition, the cooling rate impacts the emerging microstructure. The lamellae can be fine or coarse according to the cooling rate. Slow cooling from the  $\beta$ -phase leads to the form of a pure coarse lamellar microstructure. Rapid quenching results in a fine needle-like microstructure called martensite. Cooling from an area just below  $\beta$ -transus forms a combination of lamellar and equiaxed microstructure, called bimodal. [LEYE03] illustrates the difference among the three microstructural types and visualizes it in figure 2-5. The fine-grained microstructure improves the mechanical properties in general. Fine equiaxed microstructure exhibits better strength as well as better ductility. However, a coarse lamellar microstructure is needed for both creep and fatigue crack growth resistance. So, a bimodal

structure acquires the advantages of both microstructures and is consequently sought within an ideal heat treatment. It is noteworthy to define the martensite in titanium alloys as a non-brittle needle-like microstructure, unlike in steel.

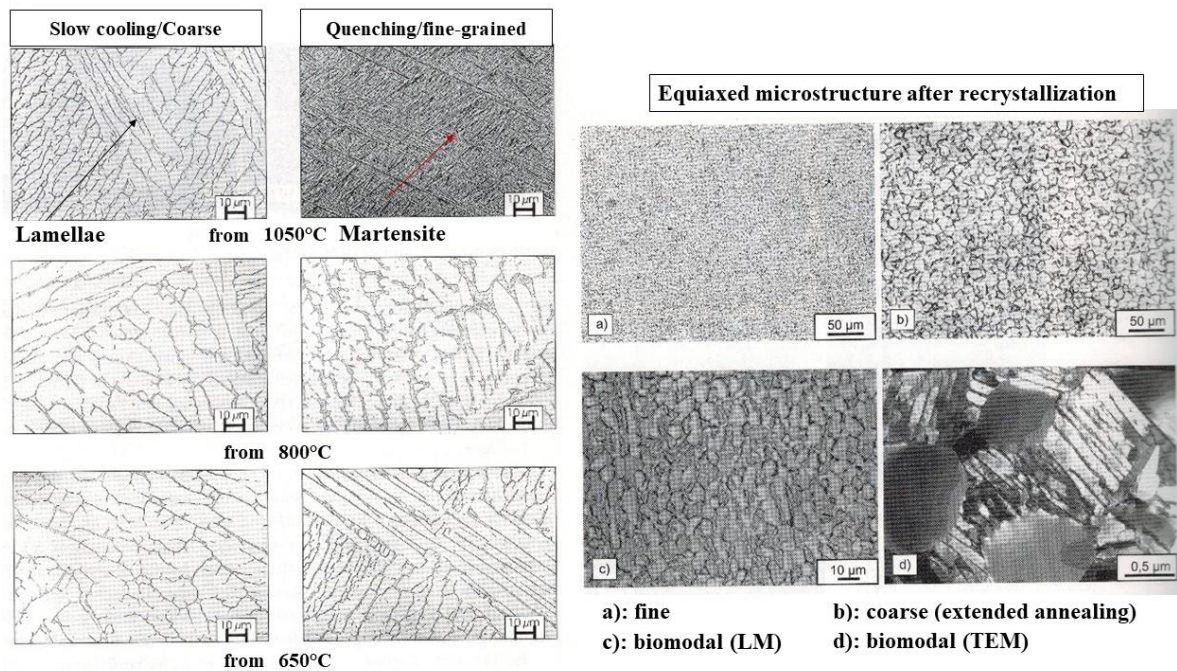


Figure 2-5: Microstructure of Ti6Al4V according to heat treatment condition [LEYE03]

Ti6Al4V is the representative alloy of  $\alpha$ - $\beta$ -ones and still, so far, the widest-used titanium alloy in the aerospace industry. Many studies have characterized its behavior in high temperatures to estimate the tensile properties at various temperature levels. While [BADR15] stated a severe cold forming of Ti6Al4V with undesired fracture and springback, [LÜTJ07] limited its applications up to 400°C. In the late 1960s, the Americans developed a new  $\alpha$ - $\beta$  titanium alloy to find a use in the fabrication of aeronautical engine components, where the high temperature prevents the usage of Ti6Al4V [ODEN08]. They replaced the vanadium with zirconium, tin, and molybdenum to improve the creep resistance in temperature levels beyond 400°C. This alloy is called Ti6Al2Sn4Zr2Mo (Ti6242).

[MANT20] and [ANTT20] investigated the creep resistance of Ti6242 at elevated temperatures and pronounced a superior behavior up to 538°C, provided in addition to some silicon as described above, which makes it a preferable titanium alloy in aerospace applications. Figure 2-6 overviews the usage of both Ti6Al4V and Ti6242 in civilian airplane parts.

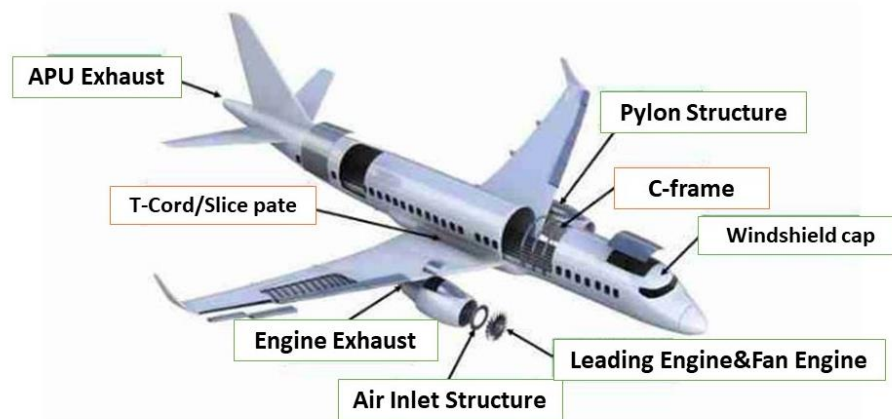


Figure 2-6:  $\alpha$ - $\beta$ -alloys applications in a civilian airplane [SANA20]

Ti6Al4V and Ti6242 were the most suitable alloys in superplastic forming, conducted at approximately 900°C. Company NKK developed a new  $\alpha$ - $\beta$ -alloy to suit superplastic forming and reached similar superplasticity and rather better than that of Ti6Al4V at 730°C, reducing the manufacturing cost of superplastic forming. This alloy is called SP700 and has the following material composition: Ti4.5Al3V2Fe2Mo [SWAL04].

#### 2.1.5.4 Titanium-aluminide alloys [LEYE03]

In order to achieve an alloy to be used in higher temperature levels, alloying of titanium alloy with aluminum to a percent higher than 6 wt. % was discussed in the 1970s. The distinctive intermetallic compound is in the form of Ti3Al ( $\alpha_2$ ) as well as TiAl ( $\gamma$ ). Titanium aluminide alloys exhibit excellent oxidation resistance at high temperatures with increasing aluminum content (its range is limited between 20 and 65 wt. %). Improving Creep resistance at extensively high temperatures is formulated by the addition of tungsten [W], molybdenum, and silicon [LEYE03]. This kind of titanium alloy is of high importance. However, further investigation of it is out of the scope of this dissertation.

#### 2.1.5.5 Additive manufacturing methods in titanium

Additive manufacturing (AM) methods have been developed in the last decade so that they have become a relevant method to fabricate semi-finished products of metals like steel or titanium. Reports presented at the 14th world conference on titanium 2019 treated Ti6Al4V exclusively and showed an ability to avail AM methods to improve the microstructure of such an alloy. Some of these articles demonstrated that very complex aircraft parts have been precisely manufactured by powder bed and large prototypes via powder feeding accompanied by controlled microstructure and convenient corresponding mechanical properties [CHAN20].

Other approaches tried to control the microstructure of Ti6Al4V via additive manufacturing. A French study in Toulouse [CASA20] facilitated electron beam melting [EBM] to produce samples of Ti6Al4V and examined their properties according to the corresponding parameters of manufacturing. [DUMO20] and [DUNS20] aimed at describing the effect of parameter variation on the mechanical properties of the titanium alloy, as mentioned above, fabricated by laser beam melting [LBM] or fused filament fabrication [FFF]. [FUNC20] established a relationship between selective laser melting [SLM] parameters and the acquired Ti6Al4V microstructure, which impacts, in turn, the mechanical properties, and stated good tensile properties depending on the surface quality within SLM.

## **2.2 Forming of titanium alloys**

### **2.2.1 General overview of forming methods [DOEG10]**

German institute for standardization (Deutsches Institut für Normierung [DIN]) set a definition for forming methods as one of six manufacturing processes in which a plastic changing in the body shape takes place, whereas both its mass and cohesion are retained. Research institutes investigated the deployment of wrought materials. Rolling and open die forging were ascribed as suitable methods for the first processing [DOEG10]. Then wrought material is delivered to another processing stage, namely the fabrication of material to a nearly finished product. Two main forming categories are regarded in this stage:

- Sheet forming
- Mass forming

In the following, the sheet forming will be discussed extensively. Mass forming is out of the scope of this dissertation.

### **2.2.2 Sheet forming [DOEG10]**

Sheet forming is used to produce semi-finished industrial parts. Bending, rolling, warping, deep drawing, stretch forming, stamping, extension, and bulging are sheet forming methods deployed for this purpose. The important sheet forming method, which will be mainly discussed in this study, is deep drawing. According to DIN 8584, it is defined as a manufacturing process of tension-compression forming, in which a flat sheet metal blank is formed into a hollow body. Prof. Doege et al. demonstrated in [DOEG10] that understanding the material behavior is essential to adapt the right forming method. Material deformation is categorized into reversible (elastic) and irreversible (plastic). A tensile test was introduced to describe the material

behavior, in which homogeneous uniaxial stress is introduced into the material. With regard to sheet forming, some parameters (like the shape of the tensile test sample, strain rate, temperature, etc.) are specified in European Standards EN 10002 for the characterization of the mechanical behavior. Figure 2-7 shows a typical tensile curve called a stress-strain curve.

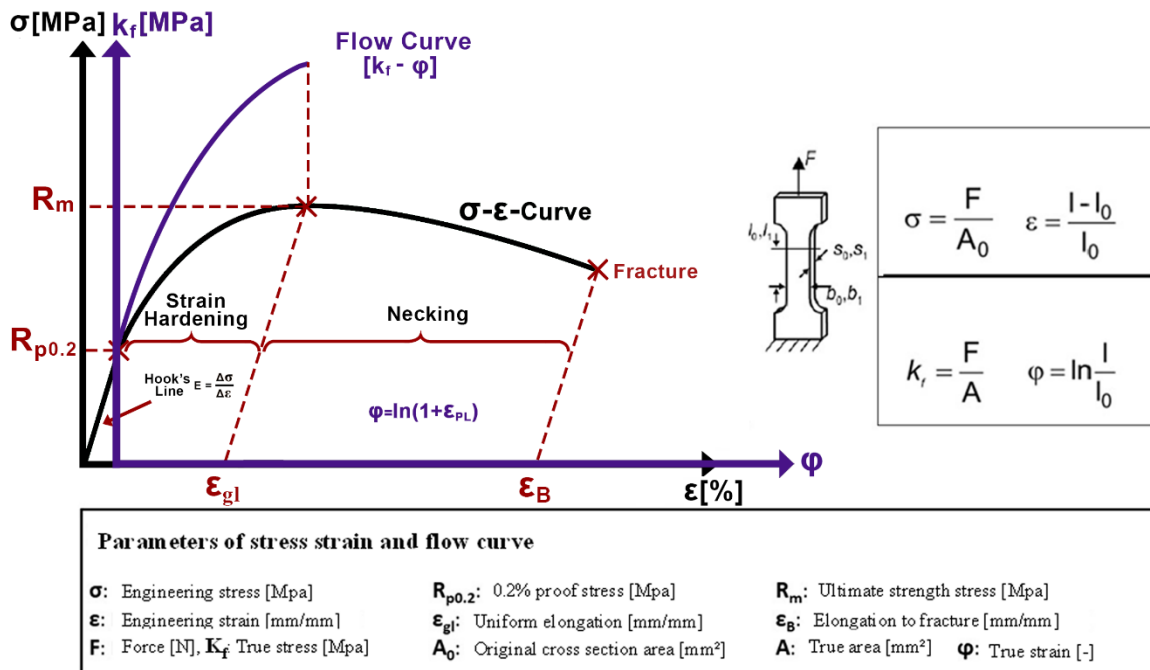


Figure 2-7: Stress-strain and flow curves under tensile loading in acc. with [DOEG10]

The dashed line represents the stress-strain curve, while the continuous line represents the flow curve. At the beginning of loading, the material behaves elastically. This is depicted graphically as a straight line called Hook's line [DOEG10]. In this area, we can describe the material behavior with the elastic modulus "E" as a function of the engineering stress and strain, figure 2-7. Loading beyond the Hook's line induces a plastic deformation inside the material. The point at which the plastic strain starts in the material is called the yield point ( $R_{p0.2}$ ). It is also the starting point of the flow curve. Most pure metals, such as Al and Cu, have no pronounced yield point. Titanium and steel exhibit, however, such a pronounced yield point [DOEG10]. The homogeneous uniaxial elongation ends at the maximum uniaxial tension, called ultimate tensile strength  $R_m$ . At this point, the highest elongation is called uniform elongation or elongation before necking  $\epsilon_{gl}$ . Beyond this point, a multiaxial stress state occurs, and thus, the material cohesion is lost, and its behavior cannot be described precisely anymore. For this reason, the area between the yield point and ultimate tensile strength in the tensile test is the whole matter from the point of sheet forming view. This area is called the strain hardening area.

$\varepsilon_B$  describes the elongation to fracture and is important rather for obtaining general information about the material ductility. Such a typical curve is usually obtained by testing at room temperature. However, testing at elevated temperatures reveals another material behavior (look at chapter results). The flow curve considers the strain hardening area and is drawn with flow stress  $K_f$  over true strain  $\phi$ , which is the logarithmic change in shape. The relationship between flow (true) stress and true strain has been described by a lot of scientists who took all the involved parameters into consideration. The issue of the flow curve will be presented in 3.5.2, “Experimental Procedure,” explicitly. A deep drawing tool, shown in figure 2-8, consists of a punch, a drawing ring, a drawing die (cavity), and a blank holder [DOEG10].

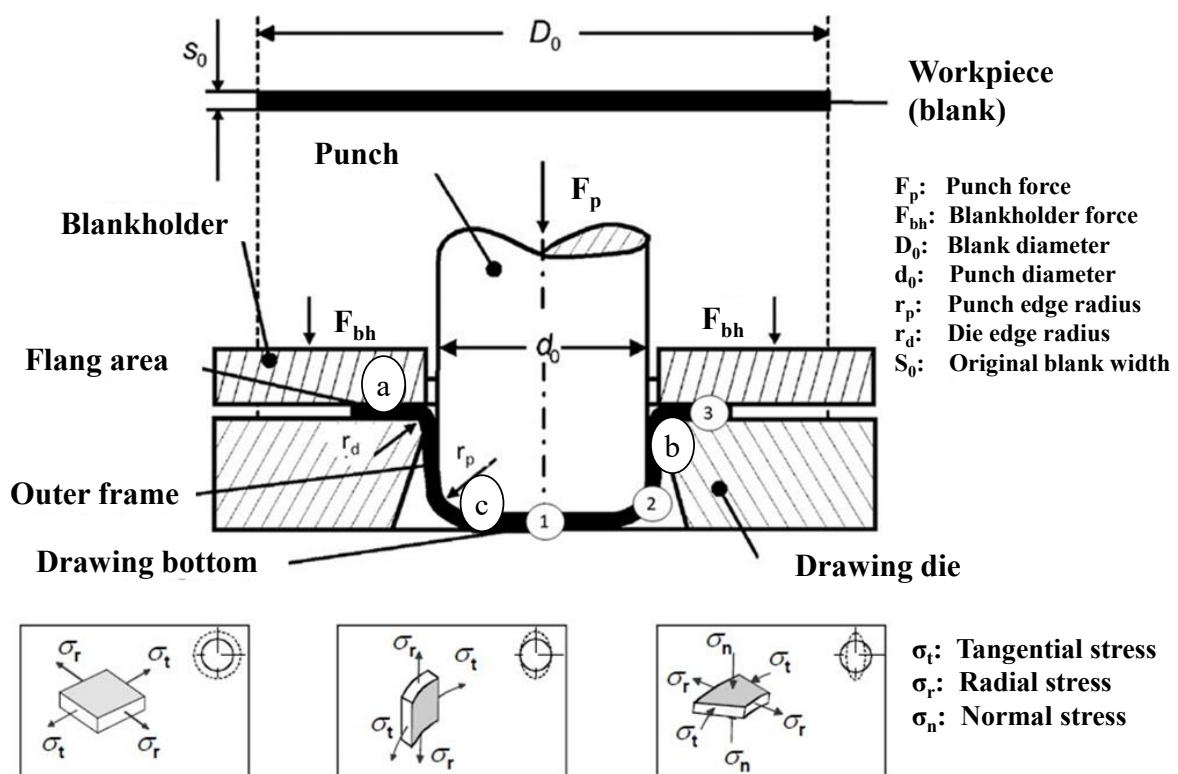


Figure 2-8: Deep drawing tool [DOEG10]

After applying a pre-defined blank holding force ( $F_{bh}$ ), a multi-stage load drives the punch to contact the blank. The blank bottom initiates forming by stretch drawing without any material flow in the flange area. After that, biaxial tensile stress causes the material to flow, corresponding with an increase in the surface area and a drop in the blank width ( $S_0$ ). When a material can transfer the local stresses to the adjacent area through a pronounced hardening behavior, it is considered suitable for deep drawing. This hardening behavior can be described in the material model and is highly important to evaluate the drawability of the alloy [DOEG10].

A local constriction in the material indicates the upper limit of the applicable strain and gives a point toward stopping the deep drawing process [KULP03].

Figure 2-8 also shows the stress distribution within the material during deep drawing. If the force applied on the bottom (1) reaches the required value, the material starts to flow from the flange area down toward the cavity, and the deep drawing process begins. Here, flange area (3) is deformed under tangential compressive stress as well as radial tensile stress, figure 2-8. Due to the normal compressive stresses, the formation of wrinkles (hereafter: earing) in the area (3) can be at most prevented. A two-dimensional stress state occurs at the punch-blank contact area (2), preventing any further deformation in the peripheral direction at  $r_p$ . For this reason, stresses in areas (2) and (3) should be profoundly adapted to ensure smooth plasticity [DOEG10].

Prof. Doege et al. defined in [DOEG10] an important parameter to estimate the deep drawability for a rotationally symmetrical component.  $\beta_{0max}$  is the limit drawing ratio (hereafter LDR) and calculated as a quotient of a maximum blank diameter without failure  $D_{0max}$  to the punch diameter  $d_0$  as given in equ.2.1.

$$\beta_{0max} = \frac{D_{0max}}{d_0} \quad (2.1)$$

The adaptation of the aforementioned issue is connected to additional effective parameters within the sheet forming stage to achieve a convenient component with high consistency of mechanical properties and geometry. Unadapted parameters result in drawbacks in the deep-drawn part or, in some cases, an irremediable defect. The coefficient of friction, springback, and anisotropy are the spoken parameters [DOEG10].

### 2.2.2.1 Coefficient of friction $\mu_f$

Figure 2-8 shows three contact areas between the blank and the deep drawing tool or between two parts of the tool itself. Area (a) is the contact in the flange area with the blank holder and the drawing die, while area (b) is between the rounding edge of the blank and the drawing die. The friction in these two areas must be very low to ensure a homogeneous wall thickness throughout the drawing process. With respect to material flow, a low friction value in area (a) leads to small frictional forces. However, such low friction in this area could result in material convexity. On the other side,  $F_{bh}$  should be adjusted to ensure low friction in area (a) with continuous contact between the blank holder and the blank preventing the formation of wrinkles, known in the field of forming technologies as “earing” [DOEG10]

Contrary to the low friction value in area (a) and (b), the coefficient of friction contact area (c) between the punch and the blank should be relatively high to establish a good force transmission. With regard to tool wear, the application of a lubricant, which creates a

hydrostatical film between the tool and the workpiece, ensures suitable arithmetic mean roughness ( $R_a$ ). Therefore, choosing the right lubricant depends on the material of both the tool and workpiece [DOEG10]. Within deep drawing, the following basic friction mechanisms of solid body friction have to be considered (figure 2-9):

- Adhesion
- Abrasion
- Deformation

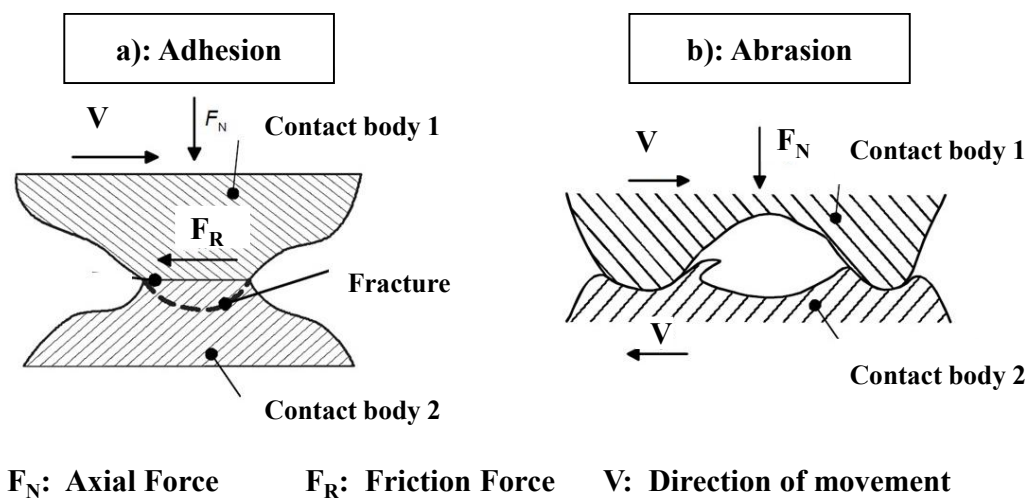


Figure 2-9: Tribology of contact areas [DOEG10]

Adhesion is all forms of the formation of molecular bonds on the surface of the mutual area of participating parts. It occurs when metal surfaces are touched with molecular interactions on a thin surface. Contrary to this, abrasion covers deeper areas. It occurs mainly when two contact bodies with different hardness move away from each other. Consequently, the material with higher hardness penetrates the surface of the softer one, which leaves some grooves on its surface and indicates wear on the body. The third tribological aspect is contact deformation, which occurs due to a tangential movement of the contact bodies. However, the description of this deformation relies on the refinement of the body's surface [DOEG10].

Titanium alloys exhibit adhesive friction by contact with a steel tool, which cannot be avoided by applying a lubricant [MANG83]. For this reason, significant friction is expected to occur during the deep drawing of titanium sheets in a steel forming tool; thus, a high tool wear with possibly process failure. [DOEG10] et al. recommend gluing the blank with a drawing film before forming, while [BEAL06] recommends for hot forming a graphite suspension with boron nitride. This could be particularly important on the side of the drawing die, reducing friction and improving the flow of the material during the deep drawing process. It is also suggested to

use a plastic-forming tool instead of steel. [SHAO12] studied the influence of the coefficient of friction value on the thickness distribution of a superplastic deep-drawn sheet of Ti6Al4V. According to the simulation conducted in this context, the lower  $\mu_f$ , the more uniform the thickness distribution.

### 2.2.2.2 Springback effect

Non-ferrous metals exhibit a noteworthy drawback within the deep drawing process called springback [BEAL06]. It is a significant return of the material to its original shape after releasing the component out of the forming tool owing to the high internal elastic energy. This phenomenon should be avoided in many pretreatment and post-treatment methods to ensure an accurate geometry for the part. For this reason, residual stresses have to be reduced. Many papers handle this issue with aluminum and titanium alloys as, mostly, the two metals corresponding to the springback effect. [RIBE10], [KIM18], and [ZHAN13a] investigated the angular return after sheet forming on three different kinds of aluminum alloys; namely 2xxx, 5xxx, and 7xxx systems, and suggested solutions to avoid this drawback. They all agreed on the forming at elevated temperatures to minimize the elastic energy of the material. Profound works concentrated on titanium alloys to describe their behavior in cold and hot forming. [KOT14a] confirmed the statement of high springback potential in the cold forming of Ti6Al4V. Forming of such an alloy at higher temperatures was studied by [ZON15a] and revealed a convenient springback behavior. [LI12] regarded the cold draw bending of high strength Ti-3Al-2.5V tube and stated a bad springback behavior for this alloy within cold forming in comparison to AA5xxx and stainless steel, which reached worst cases in accordance with variation of other parameters 78%. Although cp-titanium alloys have excellent ductility at room temperature, they are unfavorably cold-formed because of the high residual stresses. To avoid this, [OROZ18] therefore suggested a forming temperature above 500°C. [OZTU10] studied specifically the effect of temperature on springback of sheet forming of Ti cp2 and established a functional relationship between the springback angle and the forming temperature up to 300°C, irrespective of other effective parameters such as punch radius or blank thickness. Figure 2-10 shows his contribution to the springback investigation on this important titanium  $\alpha$ -alloy and the resulting equation.

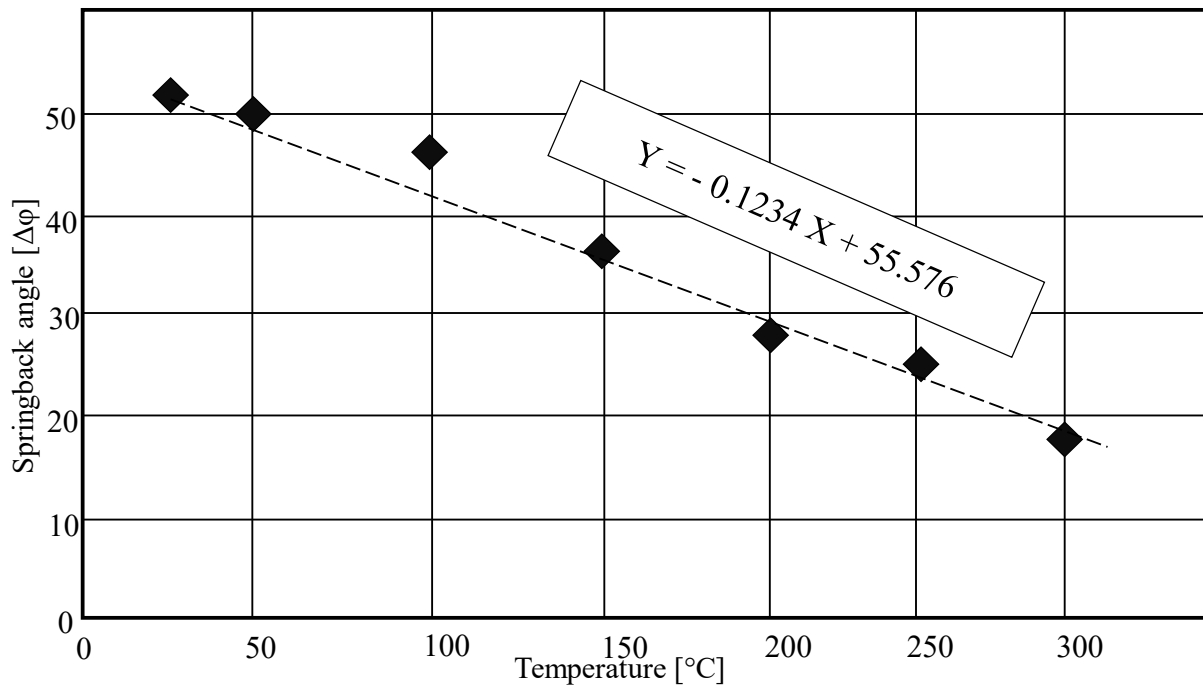


Figure 2-10: Springback angle over forming temperature for ASTM Gr.02 [OZTU10]

### 2.2.2.3 Anisotropy

Isotropy is a crystallographic feature to describe a material with the same mechanical and physical properties in all directions (represented mostly by rolling direction  $0^\circ$ , transverse  $90^\circ$ , and diagonal  $45^\circ$ ). According to the specific texture, some materials exhibit different mechanical and physical properties depending on orientation [STUT14]. This is referred to as an anisotropic property of a material. Such a specific crystallographic feature plays a major role in defining material behavior. Depending on the purpose, anisotropy can be a good feature. However, in deep drawing, it is detrimental. It plays a big role in the deformation of the material flow and specifies the formability of the material, especially in the case of cold forming [WON15] and [HARA14]. In deep drawing, two parameters of anisotropy are recognized: the normal ( $r_m$ ) and the planar anisotropy ( $\Delta r$ ) [DOEG10]. The former describes the directional dependence of deformation behavior under uniaxial tensile stresses. R-value in each direction can be calculated according to DIN EN 10130 and ISO 10113 at a 20% strain by equ. 2.2.

$$r = \frac{\ln \frac{b_1}{b_0}}{\ln \frac{s_1}{s_0}} \quad (2.2)$$

Whereas  $b_1$ ,  $b_0$ ,  $s_1$ , and  $s_0$  are the instant width, the original width, the instant thickness, and the original thickness, respectively [DOEG10]. If  $\varepsilon_{gl}$  is lower than 20%, then ( $r$ ) can be calculated in a strain below, mentioning this strain as an index, i.e.,  $r_{90/15}$  denotes an r-value determined in the transverse direction at 15% strain value. Obviously, ( $r$ ) can be calculated in the three

abovementioned directions. Consequently, a so-called mean normal anisotropy ( $r_m$ ) is a result of  $r_0$ ,  $r_{45}$ , and  $r_{90}$  as follows [DOEG10].

$$r_m = \frac{r_0 + r_{90} + 2r_{45}}{4} \quad (2.3)$$

A high  $r_m$  value ( $r_m \gg 1$ ) means that the change in width is greater than the change in thickness. Strengths are inversely proportional, though, i.e., the strength in the width direction is lower than that in the thickness direction. This is a sign that the material is particularly suitable for deep drawing. The higher the mean normal anisotropy  $r_m$ , the lower the strength in the blank, which is why the flange area can be drawn in with comparatively small forces [DOEG10]. On the other hand, the force transmission in the bottom area at risk of cracking is greater with a high  $r_m$  value since the sheet metal thickness is formed mostly in this area, and the sheet metal has a higher strength in the direction of the sheet metal thickness [DOEG10]. For this reason, a proportional relationship between  $r_m$  and LDR for some steel alloys has been dictated at room temperature and depicted schematically in figure 2-11 [DOEG10].

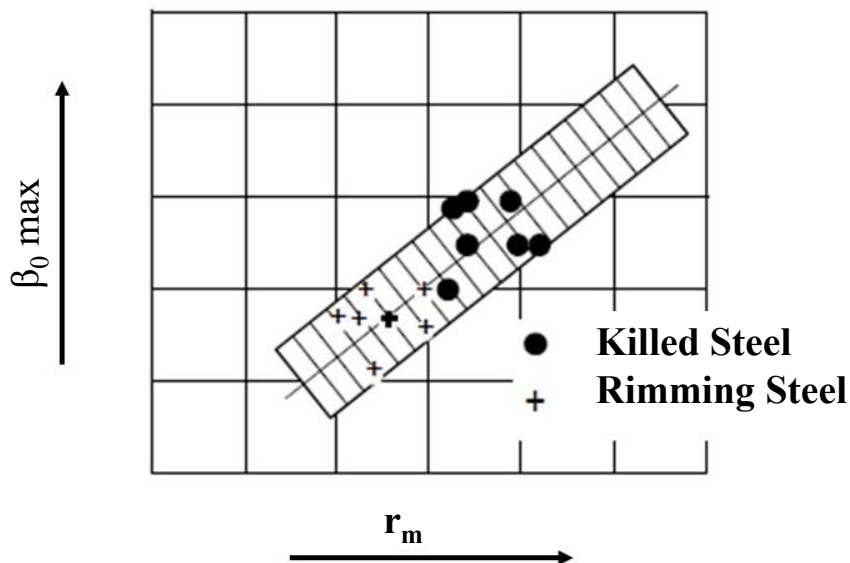


Figure 2-11: Relationship between mean normal anisotropy and LDR [DOEG10]

Planar anisotropy  $\Delta r$  denotes the affinity of material to build the ears, which are undulations in the flange area at the end of the deep drawing stage accompanied by non-uniform wall thickness distribution. It is calculated as follows [DOEG10].

$$\Delta r = \frac{r_0 + r_{90} - 2r_{45}}{2} \quad (2.4)$$

Indeed,  $r_m$  and  $\Delta r$  are quite decisive in describing the good drawability of the sheet metal [DOEG10]. An ideal drawability is assigned for the material by a high  $r_m$  in combination with low  $\Delta r$  values [KRÜP86]. With regard to titanium and its alloys, anisotropy has been investigated by many reports, owing to the deformation mechanisms of metals with hexagonal close-packed lattice structures prescribed by the  $c/a$  ratio of the unit cell. The matter of the formation of ears in titanium has become highly important. An idea of adapting the blank shape came up by [AKAM95], assuming a small blank in the high  $r$ -value direction and a large one in the low-value direction. Submicron grain size was also a suggested solution by [KAIB06] to induce isotropic formability in Ti6Al4V during superplastic forming. A numerical study conducted by [KOT14b] revealed a characteristic model of warm deep drawing and dictated convenient results of anisotropic behavior at 400°C. A similar model will be conducted within this dissertation to identify the anisotropic behavior of titanium  $\alpha$ -alloys at room and elevated temperatures and compare their behavior with respect to material anisotropy.

### 2.2.3 Classification of forming according to temperature

According to [DIN 8582], the forming process is basically divided with respect to temperature level, in which forming process is conducted in three categories.

- Cold forming,
- Warm forming, and
- Hot forming.

Recrystallization temperature ( $T_{rec}$ ) is the limit between hot forming and the other two types.  $T_{rec}$  is determined depending on the composition of the alloy and regarded generally as a function of the melting point of an alloy  $T_m$ , which is described nearly as [DOEG10]:

$$T_{rec} = 40\% T_m \quad (2.5)$$

During the cold-forming process, the metal undergoes a high-grade force in a relatively short time to achieve the scheduled degree of deformation, resulting in strain hardening, which retards further forming. Consequently, a complex shape cannot be achieved by cold forming, not to mention the required high forming force. For this reason, an approach to produce complex parts must be conducted by means of warm forming or, in case a higher degree of deformation is needed, a hot forming process [DOEG10].

Titanium alloys are generally cold formed at room temperature. Warm forming is conducted in several temperature levels starting from 150°C up to 650°C. A remarkable improvement in formability can be obtained by increasing the temperature from 20 to 150°C [DOEG10].

Typical twinning arises mostly in cold forming according to the dynamic Petch effect and results in an increase in the flow stress. This was observed by [ROBE84] and stated to be obsolete beyond 150°C. In addition, the effect of strain hardening caused by reorientation at room temperature can be avoided in warm forming and raises, hence, the drawability to almost triple value at 400°C [LIU01].

Hot forming occurs at 650-925°C, depending on the titanium alloy (see section 2.1.5). A remarkable improvement in the ductility for most titanium alloys starts above 540°C [BEAL06]. Owing to the introduction of temperature, very deep draws in one operation could be feasible [SHIP91]. An important and essential benefit of hot forming is the reduction of internal stresses to avoid the springback, which is studied by [ODEN10] and illustrated graphically in figure 2-12. A remarkable behavior of titanium alloys, speaking exclusively of  $\alpha$  and  $\alpha$ - $\beta$  alloys, is retaining mechanical properties to a high-temperature level, to which [OZTU13] referred in his publication.

Hot forming of titanium alloys also minimizes the so-called Bauschinger effect, which is defined as a drop in compressive yield strength with a simultaneous increase in tensile strength in another direction. This phenomenon can be avoided within hot forming by employing stress relieving methods (more about this matter in section 2.2.4) [ODEN10].

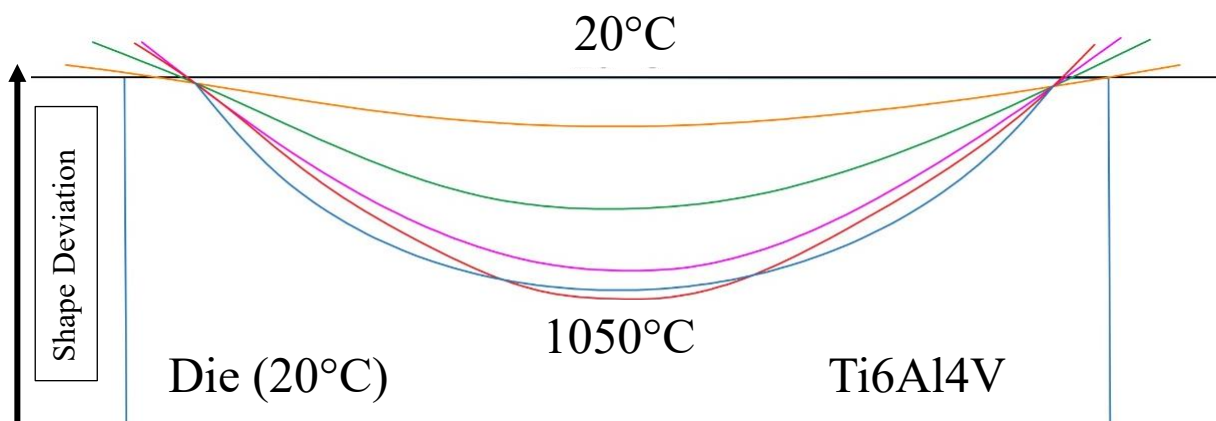


## Illustration of shape deviation with the start temperature

Figure 2-12: Springback within the deep drawing of Ti6Al4V sheet [ODEN10]

### 2.2.4 Oxidation during hot forming

Hot forming possesses many benefits over cold forming, as mentioned above. However, some features make it highly challenging and need to be deeply considered. Oxidation is a process

that occurs at elevated temperatures on the metal surface owing to exposure to a hot gaseous atmosphere [LEYE03]. It takes place in four steps: as shown in figure 2-13, the metal surface adsorbs oxygen from the environment, and a metal oxide is nucleated constantly afterward. Lateral growth of the metal oxide is accelerated in dependence on the metal's affinity of oxygen and the oxygen solubility grade. At the fourth stage of oxidation, the oxide scale becomes responsible for any further oxide transportation into the metal to compose a so-called interdiffusion layer. Various material properties and frame conditions influence the mass transport of oxide scale and can, for example, in long-term high-temperature exposure, result in cracks initiation. However, this oxide scale might protect the metal from further oxidation and can consist of mixed oxides with favorable oxides in the case of oxidation-proof alloys. Therefore, oxidation can be desired (external or selective) or undesired (internal) [LEYE03]. Titanium alloys exhibit, in general, a high affinity to combine with oxygen, whereas the solubility of oxygen in the  $\alpha$ -phase amounts to approximately 34%. Titanium dioxide  $\text{TiO}_2$  forms on the metal surface and causes the component to be brittle [PATA01]. For this reason, sub-stage oxide removal is stated by [DONA00] after each thermo-mechanical process as mandatory, especially before welding. Another solution to prevent the formation of oxide scale is to heat up titanium alloys under a vacuum or an inert gas ambient.  $\alpha$  phase seems to be more stable than  $\beta$  one in such environments, making  $\alpha$  alloys the most favorable for welding and high-temperature applications [LEYE03].

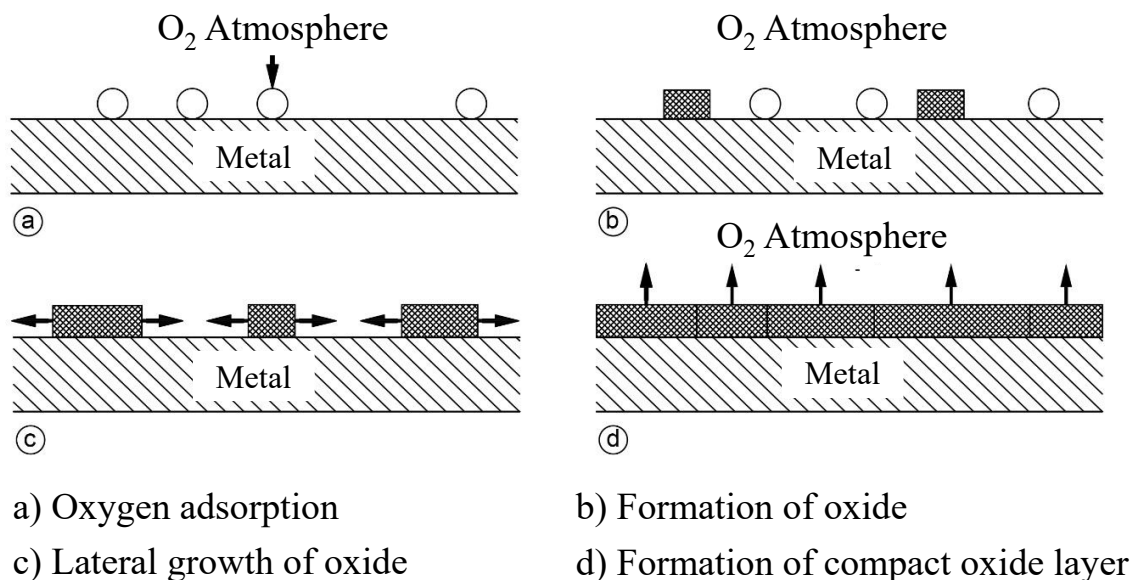


Figure 2-13: Stages of oxide scale formation [LEYE03].

Aluminum is observed as an alloying element in titanium alloys to maintain good mechanical properties at high temperatures with stable corrosion resistance. Indeed, thanks to the Al-

content of 6 wt. %, selective oxidation can be superficially induced to form  $\text{Al}_2\text{O}_3$  instead of the detrimental  $\text{TiO}_2$ . Unfortunately, the thermodynamic stability of  $\text{Al}_2\text{O}_3$  seems not to be higher than that of  $\text{TiO}_2$  at high temperatures, making internal oxidation unavoidable at operation temperatures higher than  $500^\circ\text{C}$ . Here, Titanium aluminide is suggested to be the alternative. Nb and Pa are evolved in alloying of titanium  $\alpha$ -alloys to improve their oxidation resistance, while V reduces it [DONA00]. A remarkable drawback of titanium oxidation is the formation of a surface-hardened zone known as alpha-case. The presence of this marginal feature affects the material ductility readily. [LEYE03] et al. mentioned the alpha-case presence on the surface of the near  $\alpha$ -alloy TIMETAL 1100 causes the fracture strain to be ca. half of the initial value after short-term exposure to oxide at  $600^\circ\text{C}$ , reducing the ductility of the metal consequently. Alpha-case is the typical illustration of internal (undesired) oxidation, in which a continuous layer of  $\alpha$ -phase with high oxygen content forms in the base metal [LEYE03]. Ti6Al4V has been investigated profoundly with respect to the appearance of the  $\alpha$ -case layer at an elevated temperature. [ODEN11a] stated in his modelling study a formation of  $\alpha$ -case layer at the surface of the Ti6Al4V sheet, starting from  $700^\circ\text{C}$ . For this reason, [LEYE03] and [DONA00] suggested a coating procedure to prevent the existence of an  $\alpha$ -case layer either with inert gas surrounding, like argon, for instance, or the sheet coating, which has been implemented by [PATA01] afterward. Figure 2-14 shows this  $\alpha$ -case layer emerged on a Ti6Al4V surface. On the other hand,  $\text{TiO}_2$  film enhances the corrosion resistance of titanium alloys by passivating the surface against various corrosive environments, such as nitric acid, sulfurous acid seawater, liquid hydrogen, and chlorides. However, the integrity of  $\text{TiO}_2$  must be guaranteed to ensure the passivation effect.

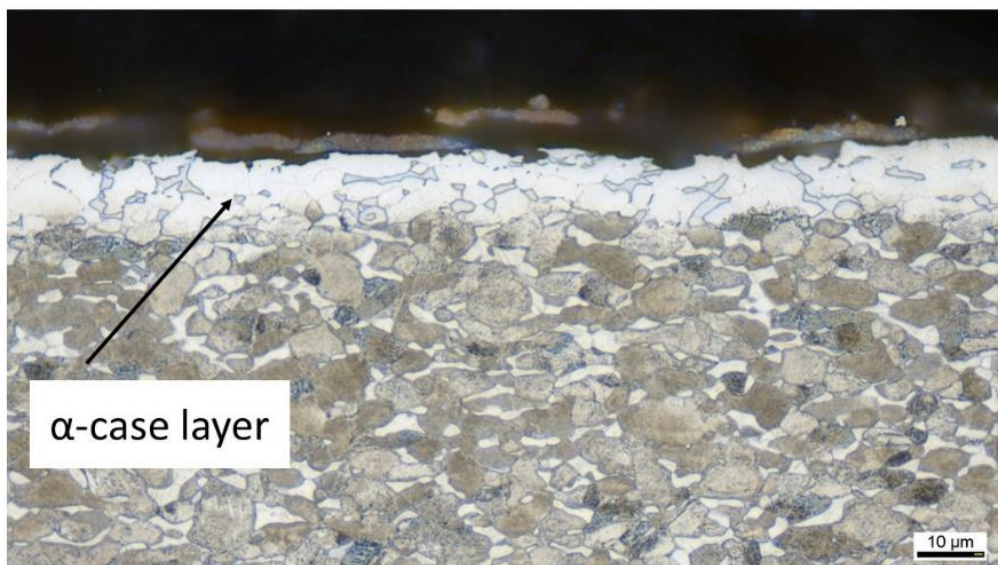


Figure 2-14: Formation of  $\alpha$ -case on the microstructure of Ti6Al4V surface.

### 2.2.5 Superplastic forming

Superplastic forming is a sheet-forming process developed to raise alloy formability. Originally, superplastic forming (hereafter SPF) is conducted above 870°C. [KOBA01] defined superplasticity as a phenomenon of enhanced ductility under a low resistance to deformation. The prefix “super” denotes a high grade of plasticity. W. Beck in [LEYE03] forwarded the definition of it, which is called up in the 4<sup>th</sup> international world conference on superplasticity of advanced materials in Osaka-Japan (ICSAM), as the ability of a polycrystalline material to exhibit very high tensile elongation prior to failure in a general isotropic manner.

The conduction of SPF can be explained as follows. Figure 2-15 shows a schema of the tool: A forming tool is prepared with all the required set-up and placed into a press machine. There, the tool is preheated to the SPF temperature, whereas SPF is an isothermal process with a small tolerance range. Once the device is ready to be closed, a predefined pressure, or vacuum, is applied and regulated the whole SPF cycle to flow the material into the form [LEYE03].

The conventional superplastic titanium alloys are Ti6Al4V, Ti6242, and Ti3Al2.5V. However, Ti6Al4V occupies the first place in SPF [BEAL06]. SPF found a big use in aerospace applications accompanied by the diffusion bonding process, meanwhile exclusively for Ti6Al4V [WENB07]. An important application to manufacture satellite fuel tanks of superplastic-formed Ti6Al4V was observed in [SATO07]. Forming at this temperature level could reach a strain about ten times higher than a normal hot forming process. This was measured with a strain rate of  $10^{-4} \text{ s}^{-1}$  [SIEM07].

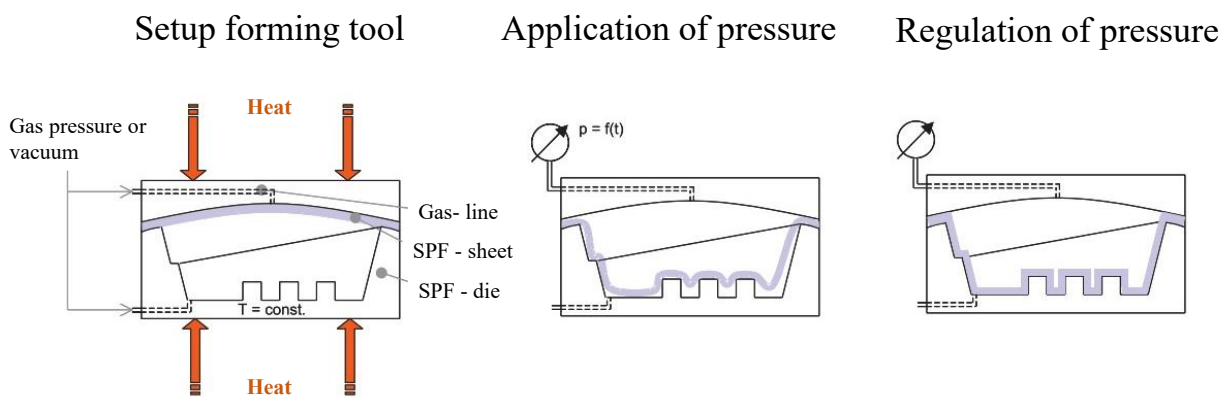


Figure 2-15: Superplastic forming mechanism, courtesy of W. Beck in [LEYE03]

Consequently, a very complex part can be formed in one stage, saving the severe effort of machine retrofitting. In addition, using superplastic forming enables precise forming owing to the high temperature, which makes the internal stress extremely low. Since the gas pressure is

the force supply, it ensures an equal stress distribution and causes the blank to form uniformly with consistent wall thickness all around [LEYE03].

However, SPF presents challenges with regard to the temperature level at which it is executed, making the material apt to oxidation and formation of  $\alpha$ -case. In this case, an application of protective gas becomes necessary, as well as an expensive heat-resistant material tool. A very low strain rate should be applied to obtain the desired strain value. Moreover, the cycle time is quite high compared to other forming methods [CHAR13]. [LIU13] tried to reduce the SPF temperature of Ti6Al4V from 900°C to 800°C and stated a considerable loss in strain range. Other studies regarded the optimization of material structure in order to implement SPF at a lower temperature without recording a significant loss in strain. [ZHAN14] investigated an ultra-fine-grained Ti6Al4V and demonstrated the theory that grain size may influence the forming outputs. Here, an SPF temperature reduction to 800°C could have been achieved, thanks to the grain size. A similar result with a similar approach had been obtained by [KAIB06] before, which also reported better weldability owing to decreasing the grain size.

Based on the refinement of the microstructure, other works concentrated on the alloying itself to adapt SPF and reduce its temperature. NKK developed a new fine-grain alloy called SP700 in the year 2004. This titanium alloy was particularly fabricated to conduct SPF between 730-800°C with resulting mechanical properties better than Ti6Al4V due to the elimination of  $\alpha$ -case presence [SWAL04]. A new study, presented at the 14<sup>th</sup> world Conference on Titanium in Nantes 2019, introduced a new  $\alpha$ - $\beta$ -titanium alloy called Ti54M (Ti5Al4V0.6Mo0.4Fe) as a real replacement of Ti6Al4V in SPF with temperature 100°C lower, which has a positive influence on the durability of the forming tool [MAND20].

### 2.2.6 Hot creep forming

Hot forming has been admitted to fabricating aerospace components of titanium alloys to achieve high strain values and stress relief without affecting the material properties in general. SPF fulfills these features as mentioned above. However, some challenges have been faced within the SPF process [BEAL06]. So, it was necessary to find a compromise and have a convenient strain range with the non-springback issue while simultaneously avoiding SPF's disadvantages. This was the motive of many studies, either to conduct a pretreatment as illustrated in [ZHAN19] about the benefit of using pre-stretching to improve the mechanical properties of a formed component or to adapt a post-treatment stage after HDD like the so-called hot creep forming (hereafter HCF). The latter solution was mentioned by Roger Pearce

in Great Britain at the Conference of Advanced Materials in 1991 and commercially submitted as an industrially important forming method [DONA00].

For a long time, aluminum, as well as titanium alloys, were investigated with regard to HCF. In the case of age-hardenable aluminum alloys, this process must be conducted below the age-hardening temperature of the alloy in order not to retard the mechanical properties. For this reason, HCF is called, in this case, creep age forming (hereafter CAF) [JAMB02]. [LUO17] established a CAF for AA-2xxx alloy at 165°C and achieved an approximate 10% improvement with respect to springback compared to forming without creep. AA-7xxx alloys exhibit rather better springback behavior than 2xxx after CAF at the same temperature level [RIBE10]. According to [JESH11], the forming temperature was raised up to 190°C for AA7075 to achieve a high restraint of springback. With respect to non-age-hardenable aluminum alloys, they are more favorable, owing to their corrosion resistance upon age-hardenable ones [ISMA16], and a higher forming temperature is allowed to be used. AA-5xxx (AlMgSc) alloy was developed to endure corrosivity at 300-400°C and obtain better formability than CAF according to the ability to raise the forming temperature resulting in a low-stage of springback [JAMB02].

Titanium alloys are more qualified for cold forming than aluminum ones in general. Therefore, creep forming was originally a subsequent stage after cold forming to retain the desired shape. This stage was called hot sizing or stress relaxation [BEAL06]. Indeed, springback effect of titanium cannot only be reduced but also completely overcome if a proper hot sizing stage is applied [FIOR15]. Studies in the new century contain another approach to forming with the subsequent hot sizing stage. This new approach delivered the hot creep forming process for titanium. It consists of a hot deep drawing stage, whose temperature is readily lower than SPF, and the subsequent hot sizing stage, in which the sheet is kept loaded for a predefined period, called stress relaxation time, after being hot deep drawn [BEAL06]. Holding the strain value constantly in this stage for the relaxation time contributes to transforming the elastic strain into plastic and, consequently, induces stress relief in the microstructure by reducing the residual stresses [NAWA18].

Most studies focused on the HCF behavior of Ti6Al4V, as a workhorse alloy, to adapt the process window and obtain the best parameter set. [LIU15] investigated the hot stress relaxation stage on Ti6Al4V and defined the essential parameters within HCF to be considered. A tensile test at 700°C was chosen to characterize the process and expanded the forming temperature range to 650-800°C in [ZON15b]. In the latter paper, the choice of this temperature range is traced back to the fact that 650°C is the upper limit of titanium application temperature, while 800°C is close to the recrystallization temperature of Ti6Al4V. In addition, these two papers

talked about the efficiency of the stress relaxation stage to eliminate any possible springback and its dependence on the process duration. It also ascribed stress relief to a microstructural change by migration of dislocations causing the refined sub-grains to merge, forming a larger grain. Ti6242 has also been examined for HCF suitability in [ODEN08]. It exhibited good consistency with prerequisites regarding process parameters.

HCF finds widespread use in aeronautical applications to replace SPF in some cases because their benefits are nearly like SPF ones and can even overcome many drawbacks presented in the latter process like extremely high temperatures and tool wear [KAIB06]

### 2.3 Conclusion of the literature review

The research above has focused on a string of studies that are strictly related to our work within this dissertation. According to the literature review, the following statements can be pronounced:

- Titanium  $\alpha$  alloys are already present in many industrial domains except for the aviation industry, where their application is represented exclusively by ASTM Gr.02. They exhibit very good oxidation behavior as well as heat resistance. Their inability to be hardened makes their application, in many cases, doubtful, though.
- Ti6Al4V is still the workhorse in the aviation industry among titanium alloys due to its hardenability and acceptable heat resistance. Many studies have recently reported the development of other titanium  $\alpha$ - $\beta$  alloys to enhance the creep resistance (as Ti6242).
- Cold forming of titanium alloys corresponds with some drawbacks, like high required driving forces, springback, and anisotropy.
- On the other hand, superplastic forming admits a forming method free of these features. However, other challenges arise instead.
- Hot creep forming could be a potential method to gather the benefits of superplastic forming. It could enable a generous forming with minor disadvantages compared to superplastic forming.

For all the mentioned points, an approach to examine the behavior of some titanium  $\alpha$ -alloys within deep drawing at different elevated temperatures in the crossover of warm forming to hot forming with a subsequent hot sizing stage and to compare such behavior with Ti6Al4V might be useful to admit this type of titanium alloys into the aviation industry in a proper manner.

### 3 Experimental Procedure

#### 3.1 Scientific objective of the study

As demonstrated in section 2.3,  $\alpha$ -alloys have not been investigated deeply at elevated temperatures due to the preference for Ti6Al4V usage in the aerospace industry. For this reason, titanium  $\alpha$ -alloys' behavior at elevated temperatures is examined carefully, and readiness to assess their behavior from forming stage to the next manufacturing stages. For this purpose, a collaborative project called TiB-Air, in cooperation with research partners and industrial plants, initiated the approach to manufacture a bleed air t-duct, which is generally produced of Ti6Al4V via SPF, this time of titanium  $\alpha$ -alloy via HCF and a subsequent laser beam welding. The current dissertation focuses exclusively on the formability of some  $\alpha$ -alloys and the oxidation resistance to deliver a convenient surface to the welding stage without any required treatment in between. In other words, we need to find out a parameter set of HCF conducted on suitable titanium  $\alpha$ -alloy to fulfill the aforementioned objective. Figure 3-1 depicts a sequential workflow of the study.

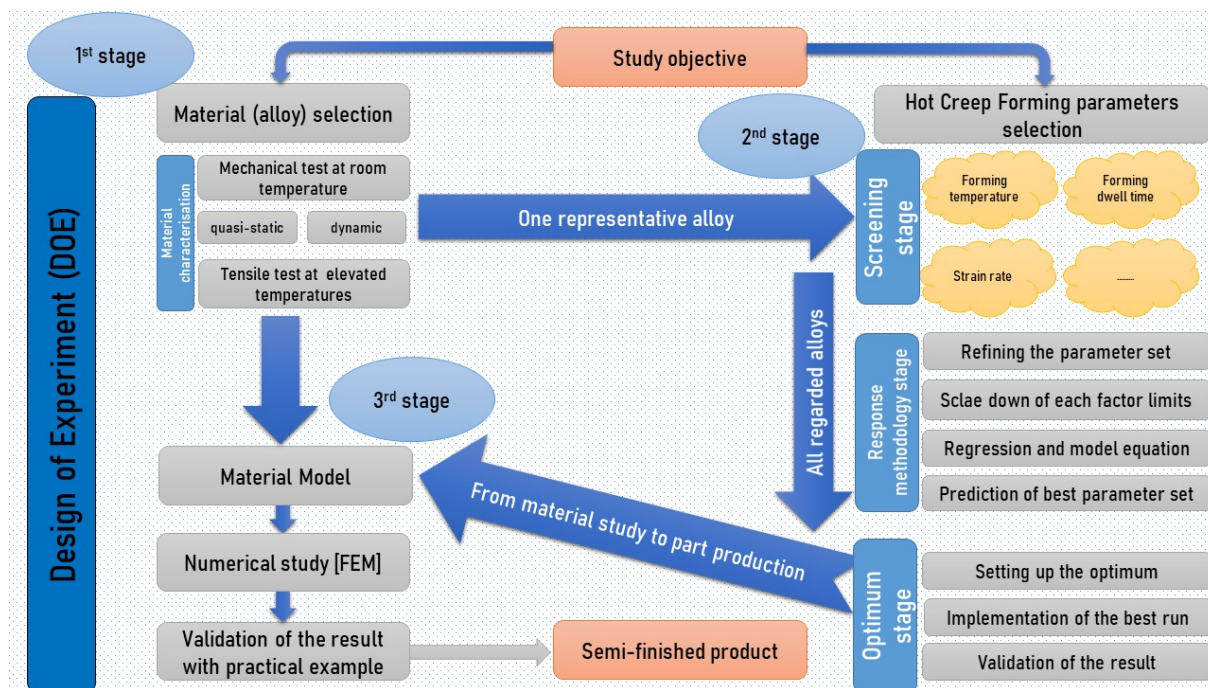


Figure 3-1: Flow chart to the design of the study

The study aims to optimize the HCF process by adapting a parameter set, with which the output implies a minor springback and, if possible, no presence of an oxide layer (or  $\alpha$ -case layer) at the end of the process.

The first stage of the study would be the material characterization of a string of titanium  $\alpha$ -alloys. Herewith, both quasi-static and dynamic tests are implemented to obtain an idea of the mechanical behavior of each alloy at room temperature. At the same time, a thermal tension test is conducted at several temperature levels to establish a material model later. Simultaneous metallography is conducted to characterize the microstructure of these alloys, including light microscopy and electron backscatter diffraction (EBSD).

In the second stage, HCF will be examined within a statistical study, which is divided into three sub-stages: Screen stage, response methodology stage (RMS), and optimum stage. The screen stage is superficial since a string of parameters will be investigated and varied without any statistical weighting to figure out the most important factors. At RMS, the shape of the parameter set is roughly defined by scaling down the factors limits step by step. At the end of RMS, a regression analysis is performed, and a model equation is revealed to describe the relationship between the (statistically) most significant parameters and the desired output. Based on the regression analysis, a statistical prediction of the best parameter set is released and transferred to the optimum stage to validate it.

The third stage of the study comprises the output of both former stages, which flows into this stage as an input to establish a material model. Since the statistical study is very detailed, one alloy is called a first-priority alloy and nominated out of the material selection stage to undergo the variation of parameters with higher scope. Based on the study mentioned above, the other alloys can be examined with a smaller number of test runs, availing results of the profound study conducted on the first-priority alloy.

After ranking the alloys in terms of their HCF behavior, a material model for each at room temperature and at elevated ones is defined in the database of a forming simulation tool. A numerical study based on these material models is conducted after defining the frame condition of HCF. After the validation of the numerical results, a semi-finished product can be implemented to industrialize the whole approach. It must be stated that the study's focus is titanium  $\alpha$ -alloys. Ti6Al4V is a part of the study to make the comparison between its HCF behavior and  $\alpha$ -alloys'. Therefore, the benefit of  $\alpha$ -alloys usage upon Ti6Al4V can be notified. In the upcoming sections, the facilities of each stage of the study will be handled in detail.

### **3.2 Material selection**

The benefits of titanium  $\alpha$ -alloys were explained in section 2.1.5. Apparently, commercially pure titanium alloys possess the highest creep resistance and formability at high temperatures. It was also demonstrated that the oxygen content plays an essential role in determining the

material strength and ductility. The most famous commercial pure titanium alloys, listed in table 2-3, are ASTM Gr.02 and Gr.04. Recently, a few titanium  $\alpha$ -alloys has been released with comparable mechanical properties to cp grade 2 but enhanced creep resistance as well as outstanding oxidation resistance. For this reason, some of them are studied instead of cp grade 2. Consequently, the experimental procedure of this work is accomplished with three titanium  $\alpha$ - alloys (besides Ti6Al4V): *KS1.2ASNEX*, *TIMET Exhaust XT*, and *ASTM grade 4*. (Hereafter: KS, XT, and Gr.04 respectively). Table 3-1 depicts the chemical composition of these alloys.

	Content max. %									
	AL	V	Nb	Si	Fe	C	O	N <sub>2</sub>	H <sub>2</sub> [ppm]	Ti
<b>KS</b>	0.7	-	0.3	0.6	0.2	0.08	0.15	0.05	13	bal
<b>XT</b>	-	-	-	0.6	0.5	0.1	0.15	0.03	15	bal
<b>Gr.04</b>	-	-	-	-	0.5	0.08	0.4	0.05	12.5	bal
<b>Ti6AL4V</b>	6.75	4.5	-	-	0.4	0.08	0.2	0.05	15	bal

*Table 3-1: Chemical composition of the regarded alloys by means of an optical spectroscopy.*

### 3.2.1 KS1.2ASNEX

This alloy was developed in Japan 2005 by KOBE STEEL, LTD to fulfill oxidation resistance of automobile parts undergoing high temperatures (as exhaust components). According to the developer it reveals the same mechanical properties of ASTM Gr.02 at room temperature. At high temperature its strength is 2 to 4 times higher than Gr.02 though. Owing to the addition of Nb and Si, a distinctive oxidation resistance compared to ASTM Gr.02 was reported up to 800°C with nearly no thickness reduction [KOBE05]. Moreover, its formability is comparable to ASTM Gr.01. It is also distinguished due to the reported weldability. Application of protective gas is however still recommended to avoid the formation of  $\alpha$ -case. An example of industrial usage of such an alloy is a tube gas in Toyota Lexus 2009 [TAKA20].

### 3.2.2 TIMET Exhaust XT<sup>®</sup>

A similar titanium  $\alpha$ -alloy was developed by *TIMETAL*<sup>®</sup> with nearly similar elevated temperature properties to KS. TIMETAL released XT also as a replacement to ASTM Gr.02, which is also utilized to manufacture exhaust components for vehicles. It exhibits an oxidation resistance at 870°C, seven times better than Gr.02 after 100 hours of air exposure [TIME10]. With regard to formability, it seems to be similar to Gr.04. *NISSAN GTR* pronounced XT usage to manufacture tube parts in 2016 [TAKA20].

### 3.2.3 ASTM Grade 04

This cp titanium alloy provides a similar ductility like XT. However, its oxidation resistance is not as good as the latter one. Such an alloy has excellent corrosion resistance, which distinguishes it [SCOT94], and superior biocompatibility, making it a potential substitute for Ti6Al4V in implants, which exhibits toxicity according to Al and V content [LI14]. Its tensile properties sound to be relatively close to untreated Ti6Al4V. It can exceed it by means of ultrafine-grained microstructuring through. The weldability of Gr.04 has been reported to be better than KS and XT [SMIR17].

To summarize the material selection, table 3-2 concludes the main aspect of each alloy, while table 3-3 collects the tensile properties of the aforementioned alloys. The recorded values are obtained from the rolling direction. Other directions, diagonal and transverse ones, exhibit other properties, which will be discussed in the results section.

Alloy	Industrial Usage	Benefit
KS1.2ASNEX	Automotive Exhaust Components	Excellent oxidation resistance compared to ASTM grade 2 with higher strength and better formability
Exhaust XT	Automotive Exhaust Components	Excellent oxidation resistance beyond KS1.2ASNEX with higher strength
ASTM Gr.04	Medical applications	Superior corrosion resistance

Table 3-2: Main properties of the regarded alloys within the study.

Max. tensile properties at room temperature, rolling direction			
Alloy	YS [MPa]	TS [MPa]	EI [%]
KS1.2ASNEX	215	350	Min. 23
Exhaust XT	480	550	Min. 20
ASTM Gr.04	560	685	15 - 23

Table 3-3: Mechanical properties of the regarded alloys within the study at RT.

## 3.3 Material Characterization at room temperature (RT)

### 3.3.1 Tensile test at RT

After selecting the titanium  $\alpha$ -alloys for this work, a quasi-static test is prepared to characterize the material properties at RT. For this purpose, some dog-bone specimens were cut from 0.9 mm thick sheets. In order to consider the material anisotropy, samples from different directions

were taken. Figure 3-2 shows the dimensions of this sample. Equ. (2.2), (2.3), and (2.4) are used to identify the normal and planar anisotropy at room temperature.

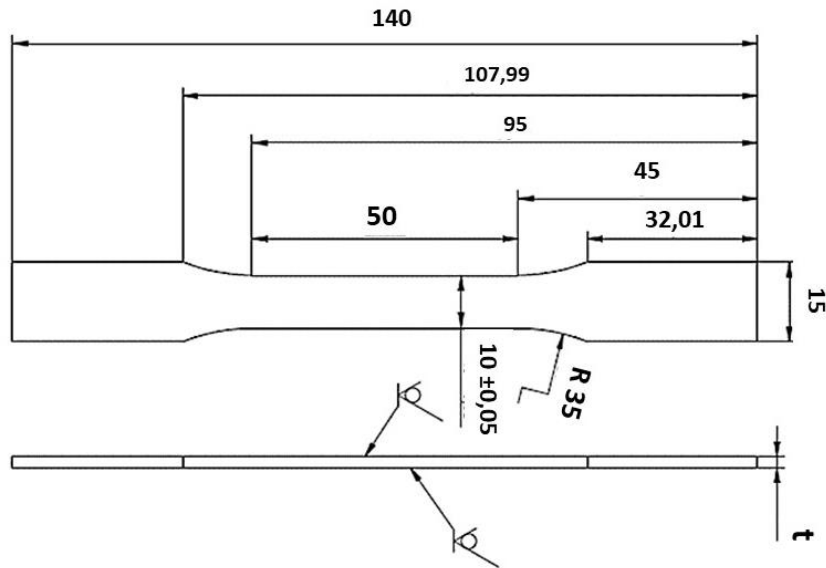


Figure 3-2: Dog-bone sample for the tensile test at RT, values in [mm].

The tensile tests at RT were carried out using a Zwick-Roell testing machine with a clamping pressure of 1.5 bar. Strain gauges were used to measure even strain. According to the tensile testing machine used, a strain rate of  $13 \times 10^{-5} \text{ s}^{-1}$  (smaller than in the hot tensile tests) was selected. For statistical reasons, each test was repeated three times, in which the machine path, the applied force, and the longitudinal and transverse strain were recorded. With the help of the strain gauges, strain can be instantly recorded, which is needed to determine  $r_m$ . There are two ways to obtain the stress-strain curve. The first one is to calculate stress and strain out of the obtained force and elongation values during the test according to equ. 3.1 and 3.2 [DOEG10].

$$\sigma = \frac{F}{A_0} \quad (3.1)$$

$$\varepsilon = \frac{l - l_0}{l_0} \quad (3.2)$$

$\sigma$ : Engineering stress [MPa]

F: Instantly recorded force [N]

$A_0$ : Original cross section area [mm<sup>2</sup>]

$\varepsilon$ : Engineering strain [mm/mm]

l: Instant length of measuring part of specimen [mm]

$l_0$ : Original length of measuring part of specimen [mm]

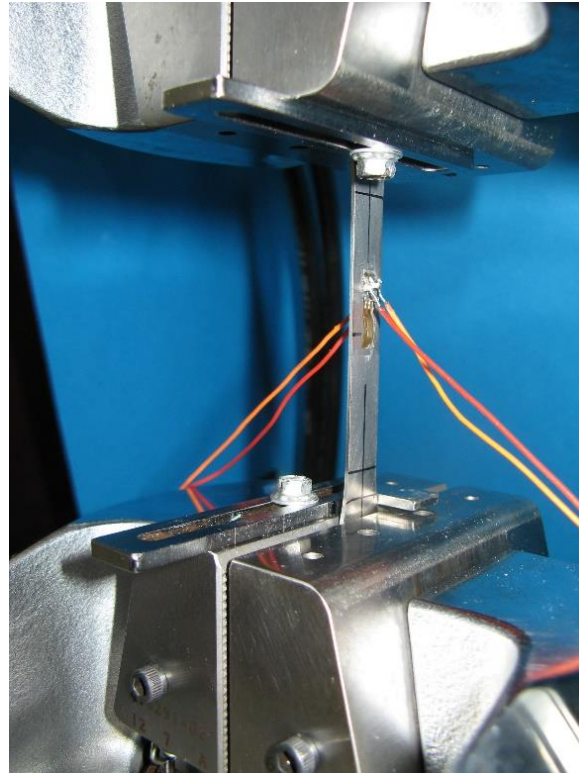


*Figure 3-3: Tensile sample with strain gauges*

The other way to obtain the stress-strain curve is to use the recorded strain directly by strain gauges. However, drawing up the curve in both ways simultaneously serves as a validation way for strain gauges. Equ. 3.3 and 3.4 describe how to build the flow curve out of the stress-strain one. Here, the instant cross-section area is regarded instead of the original one, and an incremental strain is used instead of the instant one, called degree of deformation or true strain and symbolized by ( $\varphi$ ). The strain hardening area is the most important one to draw the flow curve, i.e., necking defines the end of the flow curve, see section 2.2.2 [DOEG10].

$$k_f = \frac{F}{A} \quad (3.3)$$

$$\varphi = \ln \frac{l}{l_0} \quad (3.4)$$

$K_f$ : True stress [MPa]

$A$ : Instant cross-section area [mm<sup>2</sup>]

$\varphi$ : True strain [--]

The course of the stress strain gives information about the material's mechanical properties, while the flow curve is about its plasticity. For this reason, the creation of the flow curve is essential to establish the material model in the simulation tool.

### 3.3.2 Tensile test at elevated temperatures

Analog to the tensile test at RT described in 3.3.1, a tensile test at the following temperatures is conducted: 400, 500, 600, 700, and 800°C. Later on, a tensile test at 650°C was included due to an essential result from this approach, which will be explained in the result and discussion section. The whole tensile test is performed by the mechanical lab in the MPA institute for materials testing in Bremen on a forming dilatometer type Gleeble 3500©. It is a servo-hydraulic forming dilatometer for high heating and quenching speeds produced by DSI® in the USA. Gleeble can offer force and strain control during the experiment, making the principle of HCF, at which strain is held constant within the relaxation time, also feasible. A high conductive heating rate (up to 775 °C/s) serves to accelerate the heating phase. A pyrometer with four thermocouples, a measurement capsule, and a 2D- laser extensometer record the result of the test, respectively. Figure 3-4 shows Gleeble 3500.



Figure 3-4: Forming dilatometer type Gleeble© 3500.

The main parameter of deep drawing is the strain rate. Since Gleeble enables a large spectrum of forming velocity, even low values, a strain rate of  $25 \times 10^{-4} \text{ s}^{-1}$  is determined. This value is chosen to imitate the same strain rate used industrially to produce an exhaust system component by *Formtech® GmbH*, the industrial partner involved in this work.

### 3.3.3 Metallographic examination

In parallel to the tensile test, the microstructure of the material is investigated metallographically. In this context, a light microscope is used to deliver micrographs in various

magnifications. Here, the grain size can be determined using the so-called grain size index (G). According to DIN ISO 643, “G” can be calculated as shown in equ. 3.5.

$$G = \frac{\log m}{\log 2} - 3 ; m = \frac{1}{d} \quad (3.5)$$

G: Grain size index, m: Number of grains per mm<sup>2</sup>, d: Mean grains diameter [mm]

According to this standard, G is divided into two main categories. Up to G=5, the structure is assigned as coarse-grained, while an index of G=6 and higher defines a fine-grained structure. Such a classification is illustrated in table 3-4 in detail [MACH11].

	<b>Mean grains diameter (d) [mm]</b>	<b>Number of grains per mm<sup>2</sup> (m)</b>	<b>Grain size index (G)</b>
<b>Coarse-grained structure</b>		.....	.....
	0.7	2	-2
	0.5	4	-1
	0.354	8	0
	0.25	16	1
	0.177	32	2
	0.125	64	3
	0.0884	128	4
<b>Fein-grained structure</b>	0.0625	256	5
	0.442	512	6
	0.0312	1024	7
	0.0221	2048	8
	0.0156	4096	9
	0.0110	8192	10
	0.00788	16984	11
	0.0055	32768	12
...	....	.....	

Table 3-4: Classification of grain size [MACH11].

Another feature to be investigated with micrographs is the emergence of  $\alpha$ -case, which is related to the hot forming. In some cases, the quantification of the  $\alpha$ -case layer cannot be determined accurately with light microscopy. So, scanning electron microscopy (SEM) is also used. Electron backscatter diffraction (EBSD) is also implemented to quantify the volume fraction of

$\alpha$ ,  $\beta$ , and the oxide scale on the surface precisely, which is also detected via energy and wavelength-dispersive X-ray (EDX and WDX). EBSD Mapping, represented by pole figures (PF) and inverse pole figures (IPF), also describes the texture of the alloys at different temperature levels and ensures a comparison among the alloys texturing in correspondence to temperature levels. Microtexture is also studied with analysis of inverse pole figures to identify the material behavior from the point of HCF view. It is noteworthy to mention a remarkable aspect of sample preparation within the metallographic examination that titanium alloys are sensitive to the etching process. In this context, a special etching method is acquired according to Fuss Ti-m8 [PETZ94], with which an etching period between 10-15 s is specified, and the following composition of etchant is suggested: (150ml H<sub>2</sub>O + 3ml HF + 3ml H<sub>2</sub>SO). The same skilled worker conducts the whole samples' preparation for metallographic examination in order to eliminate any possible deviation of results. As a part of this examination, a hardness measurement, according to Vickers, is also performed at RT as well as at elevated temperatures. Most of the examinations are conducted on Ti6Al4V to achieve a comparison between the behavior of  $\alpha$ -alloys and non-treated Ti6Al4V.

### 3.3.4 Fatigue test at RT

A fatigue test is also a part of describing the material behavior to fracture under dynamic loading. In this case, the dynamic material behavior is described by the determination of stress amplitude (S) and the number of cycles to fracture (N), justifying the name of the S-N curve.

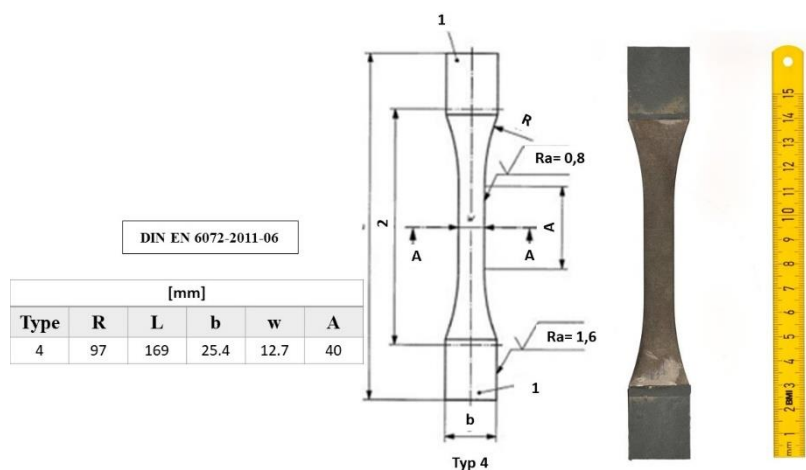


Figure 3-5: Fatigue test sample [DIN EN 6072-2011]

The sample geometry is chosen according to DIN EN 6072:2011-06, which is compatible with previous fatigue studies supported by an Airbus specification QVA-Z10-38-00, figure 3-5. The specification dictates a sample preparation process without any presence of notches before

testing. The latter results in a local increase of tension, which is not desired in our case. Therefore, the edges of the samples are rounded to a radius smaller than 0.5 mm and then polished as described in the specification. A so-called **pearl string method** is used to determine fatigue strength [RADA07]. Here, the load is gradually increased until  $10^7$  cycles, where the fatigue limit ( $\sigma_D$ ) is read out. A very important prerequisite in this method is that the highest loading value should not exceed the yield strength of the material obtained by the tensile test. A Wöhler curve is recommended to be built in order to estimate the mathematical probability of surviving under dynamic loading. In this case, a stochastic model should be assumed to extrapolate the values obtained by the S-N curve [PFAL13]. Gnedenko et al. in [PFAL13] suggested an ansatz to fit the experimental curve and have it described stochastically to plot the Wöhler curve as follows.

$$\sigma_{max}(N) = \sigma_D + \frac{\sigma_{ult} - \sigma_D}{e^{(\frac{\log N}{\alpha})^\beta}} \quad (3.6)$$

$\sigma_{max}$ : Instant strength during cycle loading [MPa]

$\sigma_D$ : Fatigue strength [MPa]

$\sigma_{ult}$ : Ultimate tensile strength [MPa]

N: Number of cycles

$\alpha$  and  $\beta$ : Shape constants.

As can be seen in equ. 3.6  $\sigma_{max}$  is a function of the instant number of cycles, and the Wöhler curve will be depicted in logarithmical form. A remarkable matter in equ. 3.6 is the existence of static and dynamic stresses in one expression, which ensures the consideration of static and dynamic failure in this equation.

In addition, all the presented stresses in equ. 3.6 are in amplitude value, which amounts to 0.45 of the stress value, assuming the stress ratio amounts to  $R=0.1$ . Shape constants can be approached with the aid of the method of least square root failure. After determining all the terms of equ. 3.6, a Wöhler curve can be drawn up to the fatigue limit at  $10^7$  cycles, whereas  $N=10^3$  is defined as the limit of the low cycle fatigue [PFAL13].

According to Gnedenko, this curve represents the survival probability of 50%. A scatter band in the survival probability range of 10-90 % can be estimated depending on the 50% curve and assuming the lognormal distribution of the results obtained experimentally, whereas standard deviation and mean value are also fitted by the method of least square. The width of the scatter band gives a sign of the result's robustness [PFAL13]. Figure 3-6 shows the projection of experimental results of the S-N curve on the y-axis in the assumption of equ. 3.6.

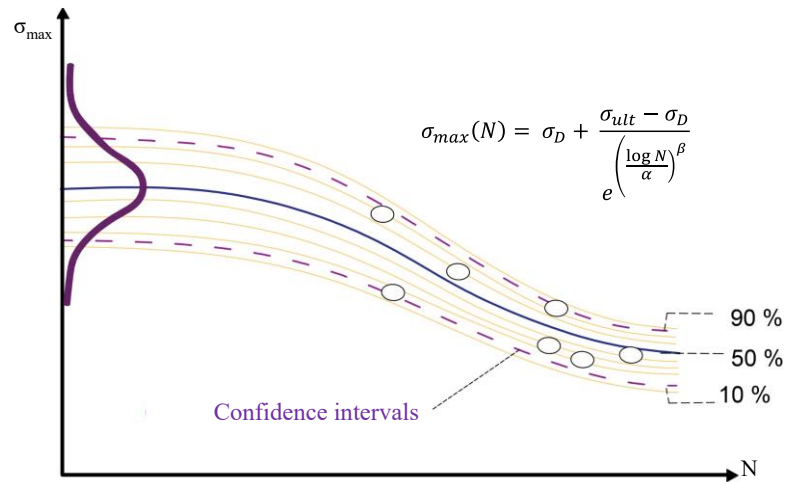


Figure 3-6: Gnedenko method and ansatz to build the Wöhler curve, according to [PFAL13]

[PFAL13] recommends a minimum number of specimens to draw the Wöhler curve of 15 samples, which is adopted within our study. Since the fatigue test is sophisticated, one of the  $\alpha$ -alloys will be tested dynamically. It is the first-priority alloy, according to the result of the tensile tests.

### 3.4 Parameter selection of hot creep forming

At the end of the material selection and characterization stage, one alloy is nominated to be investigated in terms of a statistical study. Here, the most significant parameters of HCF are identified. The HCF process consists of many steps. Figure 3-7 illustrates its sequence.

As depicted below, such a process requires two types of curves to be described. A stress curve over time consists of a heating phase, then the forming phase at whose end the stress reaches the highest value, and the stress relaxation at the last phase of HCF. The constant creep curve enhances the statement that stress relief takes place at the end of the forming stage due to the holding of material under constant strain. For this reason, the strain at the end of the forming stage, which is the start of the relaxation stage, is called creep strain. Out of this process, the factors can be determined, and the stretching tests are prepared.

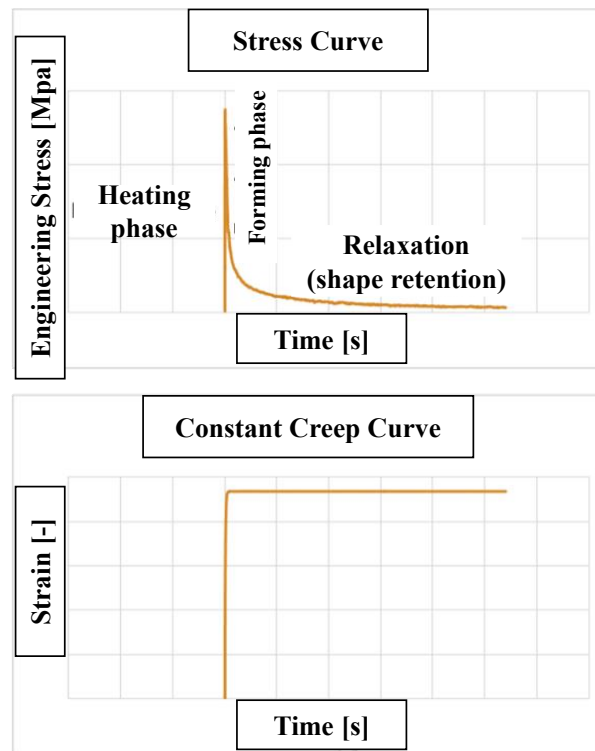


Figure 3-7: Schematic description of HCF

### 3.4.1 Definition of the study

With the help of a design experiment tool called Cornerstone©, the statistical study is performed to mention the factors of the HCF process and define their upper and lower limits. Based on papers published with respect to hot stretching of cp Gr.02 and Ti6Al4V, factors (including their ranges) and outputs are defined as listed in table 3-5 below [XIAO15] and [OZTU15].

Factors		Responses
Item [Unit]	Ranges	
Forming temperature [°C]	550 – 800	Stress relief
Heating time [s]	120 – 360	$\alpha$ case
Relaxation time [s]	0 – 1800	
Creep strain [%]	0.2 – 10	
Strain rate [ $s^{-1}$ ]	0.06 – 0.09	

Table 3-5: Factors and outputs of the study

Since the range of each input factor is already known and roughly defined as a proper one, the center point can be easily determined by Cornerstone to obtain a nearly symmetric distribution of tests around it.

### 3.4.2 Design of the study

For the screening stage, it is recommended to conduct the study without any external influences. For this reason, a linear relation among the factors is determined. Results from this linear model are introduced into the regression analysis to obtain the statistical significance of each term. This stage requires ca. 12 test runs according to the factors mentioned above.

After defining the statistically most significant factors, a refinement of these parameters and their ranges is adapted by RMS testing. At this stage, the linear model would be insufficient to determine the significance of the terms. So, a full factorial design with substantial testing might be achieved. However, such a design requires at least 128 runs to cover all the frame conditions. For this reason, an alternative design is sought.

#### 3.4.2.1 D-Optimal instead of Full-factorial design

Full factorial design means including all the possible parameter sets in the design of the experiment. Indeed, some tests require even a design with additional experiments beyond the given range to ensure covering the whole range precisely. This design is called a composite design [TREI08]. Figure 3-8 clarifies the difference between both designs schematically.

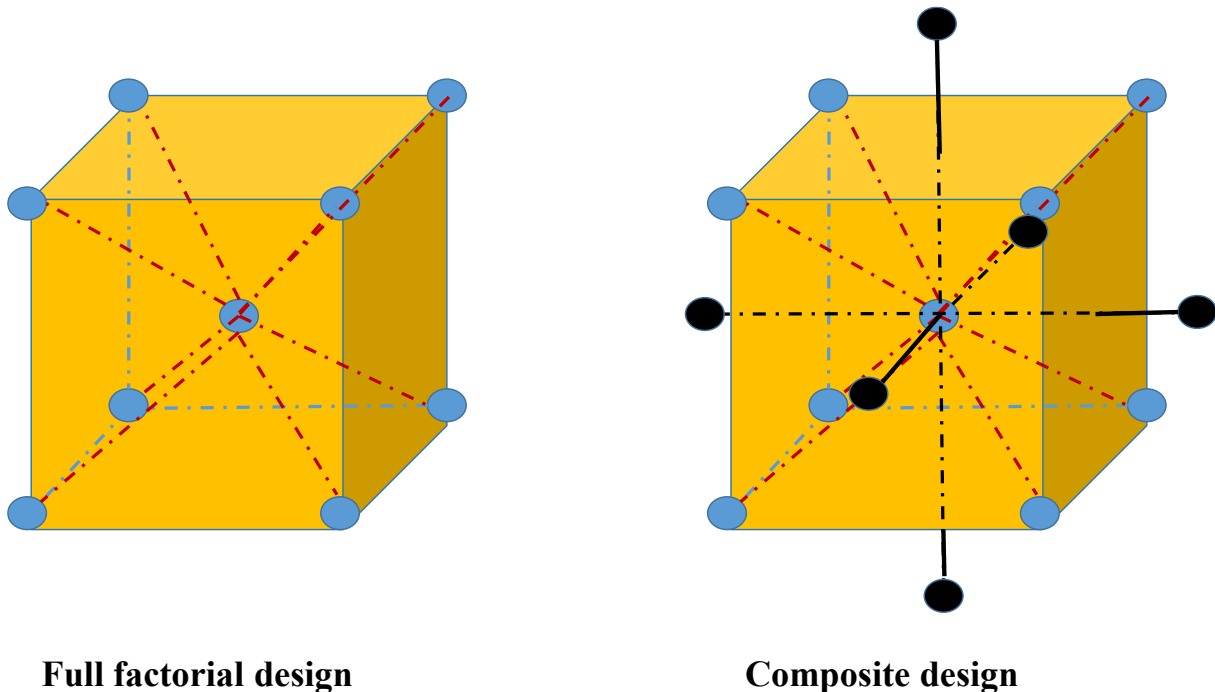


Figure 3-8: Full factorial design against a composite design.

Since our study regards five input factors and two essential outputs, it is quite expensive to conduct a full factorial or rather, a composite design. For this reason, a computer-generated (D-optimal) design is used to manipulate the design of the study without a meaningful influence

on the results. [TREI08] released a detailed thesis about D-optimal design and concluded the benefits of using it in the following points.

- The inclusion of a predefined test run is enabled by D-optimal,
- The weighting of one parameter statistically is also possible with D-optimal,
- More feasible deal with qualitative (discrete) factors,
- Some factors can have more than two levels (center point or other inclusion points), and
- The number of tests can be reduced.

The main principle of reducing the number of test runs without affecting the experiment is to create middle points among the corner ones, finding a balanced design with less number of test runs, as seen in figure 3-9 [TREI08].

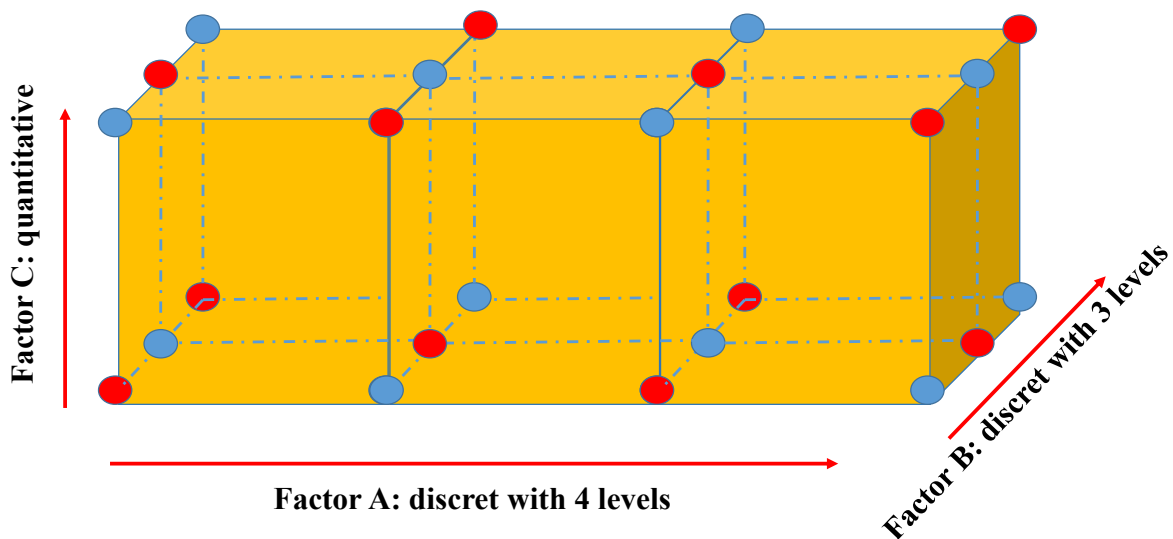


Figure 3-9: D-optimal design derived from full factorial one, Courtesy of Erikssen [TREI08]

In this example, an experiment with discrete variables and one quantitative one is designed. Both discrete variables include four levels. A full factorial design imposes a usage of all the balls to build the test runs. Consequently, the number of tests would be 24 runs. Utilizing D-optimal designs means choosing one of both paths, i.e., either the blue or the red balls. So, the number of test runs can be reduced to only 12.

### 3.4.2.2 Generating table of tests via D-optimal

In our study, seven factors are varied. That means the number of tests would be 128 with a full factorial test. Thanks to the D-optimal test, the number can decrease to 35 runs. After generating

the table of tests with the help of Cornerstone, some inclusions are favored to be also tested. For this reason, the number of test runs rises to 40. The table of tests in this sub-stage will be depicted in the results and discussion section.

### 3.4.3 Regression analysis and robustness test

At the end of RMS, regression analysis helps to define the most significant parameters and reveals a model equation in which stress relief could be estimated as a function of the best parameter set. According to such an equation, the coefficient of each term is determined. So, a statistical prediction of the best run can be estimated. Both stress relief percentage and  $\alpha$ -case layer thickness are now ready to imply the parameters of the best run.

In order to validate the study, an optimum test with the best run is conducted. The output values are specified and studied in terms of consistency with the study objective. A transfer of this parameter set can be achieved to set up the simulation tool properly.

### 3.5 Numerical study of HCF

The finite element method (FEM) is implemented within this dissertation to characterize HCF numerically. For this purpose, a simulation tool called SIMUFACT.forming© is used. Numerical study aims at achieving not only a scientific advance but also an industrial one. While the main goal of the FE study is to determine the material behavior during the forming process, such a simulation gives the manufacturers profound information about the setup of the forming tool itself to ensure consistent results with low trial-and-error testing. Table 3-6 sets a comparison between the scientific and the industrial pursuit.

Scientific interest	Industrial interest
Material flow	Forming force (pressing pressure)
Coefficient of friction	Pressing velocity
Effective stress and strain distribution	Material of the forming tool
Thickness distribution	Blank thickness
Anisotropic effect (earing)	Applied pressure on the blank holder
Thermal distribution within calculation	Expected required post processing

*Table 3-6: Scientific and practical outputs of the simulation study.*

Since the regarded titanium alloys in this dissertation are kind of uncommon, the material library of simulation tools, among them Simufact.forming, does not include a material model of them. For this reason, a proper material model should be entered into the material library.

The definition of each material is divided into essential features, which are strictly related to the hot forming process, and additional supporting ones. The essential features are described in the following.

### 3.5.1 Material definition in the simulation tool

#### 3.5.1.1 Definition of mechanical properties

Results of tensile tests described in 3.3.1 and 3.3.2 are taken into the database of Simufact.forming-library to define the materials conditions (among others). Figure 3-10 shows a representative interface of the material window in the library.

The screenshot displays the material definition interface in Simufact.forming, divided into several sections:

- General properties:** Fields for Name (New\_Material), Variant (Define variant), Int. name (Define internal name), DIN (Define DIN), JIS (Define JIS), AISI (Define AISI), AWS (Define AWS), Area of application (none), Group (none), Import source (none), and Created by (Define creator). There are also checkboxes for Tool material and Rigid plasticity.
- Comment:** A large text area for entering comments.
- Flow curves:** Includes an 'Approach' dropdown (Tables) and a 'Scope' table. The 'Scope' table has columns for Min, Max, and Unit. The 'Temperature' field in the 'Scope' table is circled in red.
- Mechanical properties:** A table defining material parameters.
 

Parameter	Type	Constant values	Unit	Tables
Young's modulus:	Constant	1.05e+11	Pa	Create table
Poisson's ratio:	Constant	0.35	-	Create table
Density:	Constant	4550.0	kg/m <sup>3</sup>	Create table
Thermal expansion coeff.:	Constant	8.5	1/K	Create table
Only for information and optional flow curve scaling:				
Yield strength:	Constant	9.85e+7	Pa	Create table
Tensile strength:	Constant	2.09e+8	Pa	Create table
Only for information / not used for simulation:				
Ultimate strain:	Constant	0.35	-	Create table

Figure 3-10: Definition of mechanical properties in the simulation tool, screenshot Simufact.forming.

Here, the mechanical properties of the alloy KS at RT are entered. Some physical properties are also demanded to complete defining the material model more accurately. Simufact.forming imposes a separate definition for each temperature range. As can be seen below in figure 3-10, the temperature level should be declared and assigned to the upcoming mechanical properties.

### 3.5.1.2 Definition of flow curves

The second step of defining a material is to enter the flow curve result into the model. In figure 3-11, the upper window contains the temperature level, strain rate, and the plotted flow curve. Flow stress is denoted by the letter Y in the flow curve window (figure 3-11). It is a function of the true strain, as seen in equ. 3.3 and 3.4. A precise description of the material plasticity behavior demands consideration of a string of parameters. Besides temperature level and true strain, the strain rate is a decisive factor in influencing the amount of flow stress. However, such an influence is expected to be more remarkable at elevated temperatures than at RT [DIER17]. For this reason, two types of fitting equations have been defined according to the temperature level. It can take one shape of both so that an ansatz, according to Ludwik, is used at RT and another one, according to Hensel/Spittel, at elevated temperatures. Both models are described by equ. 3.7 and 3.8, respectively. Such material equations are typed into the blank field shown in figure 3-11, lower window. The latter factors can be calculated mathematically with the aid of the method of least squares failure. Previous studies, like [DIER17], reported another shape of equ. 3.8 with additional factors to consider the temperature effect. Simufact.forming deals with a simplified form of this equation because the temperature has already been considered by the original material definition in the upper window of figure 3-10. The multi-level temperature material model can also be defined in Simufact.forming, as shown in the upper window of figure 3-11. However, the anisotropy can be entered in correspondence to one temperature level and is not extrapolated to other levels. For this reason, it makes more sense to define one temperature level in the interface if anisotropy is taken into consideration. Based on equ. 3.7 and 3.8, the experimental result, plotted according to equ. 3.1 to 3.4 are fitted to extrapolate the curve beyond the experimental area. It is noteworthy to mention that flow curves are obtained normally from the bulge test. Tensile tests are utilized for this purpose in our study, which restricts the accuracy of the experimental results up to  $\varphi=0.2$  [DIER17].

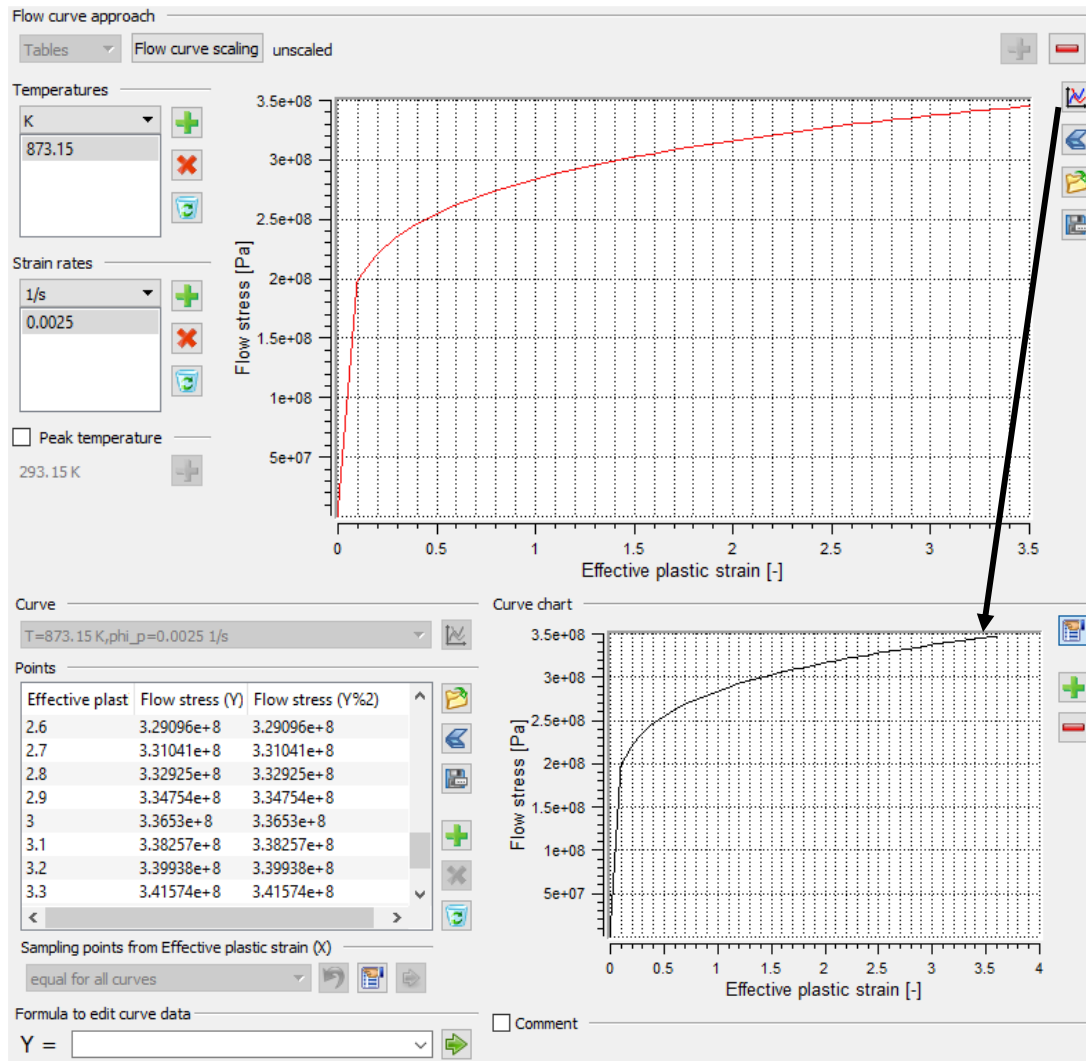


Figure 3-11: Definition of flow curve in the simulation tool

**Ludwik**  $k_f = k_{f_0} + a \cdot \varphi^n$  (3.7)

**Hensel/Spittel (easy form)**  $k_f = C \cdot \varphi^n \cdot \dot{\epsilon}^m$  (3.8)

$k_{f0}$ : start flow stress [MPa]

C: Material consistency

$\dot{\epsilon}$ : Strain rate [ $s^{-1}$ ]

a, n, m: factors related to process parameters

### 3.5.1.3 Definition of anisotropy

Anisotropy should also be considered in the material model. The effect of both types of anisotropy was explained in section 2.2.2.3. According to FEM studies made on metals, there are three stress types to describe the stress state during the forming. Figure 3-12 shows the typical von Mises type, which describes the optimal material behavior in terms of ductility. This type of stress state distribution does not match the behavior of an anisotropic material. For this

reason, Simufact.forming admits both Hill48 and Barlat91 models to achieve a material model regarding the anisotropic behavior. Hill48 was studied by [CHAR13] and profoundly by [ABSP17], while [KOT14b] performed a comparison between Hill48 and Barlat91 models. In the case of the Hill48 stress model, normal anisotropy should be calculated via equ. 2.2 and 2.3. The yield strength in all three directions (0°, 45°, and 90°) should also be entered to complete the description correctly. The background solver of Simufact.forming regarded Hill48 model according to equ. 3.9, which is described in [KOT14b] as follows.

$$f = (\sigma_{xx}^2 + \sigma_{yy}^2 - 2 \cdot \frac{2r_m + 1}{r_m + 1} \cdot \sigma_{xx} \cdot \sigma_{yy} + 2 \cdot \frac{2r_m + 1}{r_m + 1} \cdot \sigma_{xy})^{0.5} \quad (3.9)$$

$\sigma_{xx}$ ,  $\sigma_{yy}$  and  $\sigma_{xy}$ : Principal plane stresses [MPa].

On the other hand, the Barlat model imposes the calculation of the so-called yield loci exponent ( $m$ ) instead of  $r_m$ . Figure 3-12 shows the definition of anisotropy according to Barlat91. In addition, yield strength in the three directions is still entered respectively. ( $y_b$ ) is the balance stress, which is normally obtained from the bulge test. Otherwise, 0 is assigned to this field, meaning the balance stress would be the yield strength value. Simufact.forming recommends an  $m=6$  for steel and  $m=8$  for aluminum. Such a value was investigated by [ZHAN13b] et al. for cp-ti alloys and recommended an ( $m$ ) range of 8-12 and attributed the result with  $m=10$  with the highest precision. A controversial  $m=2$  was suggested by the international titanium association in [GAIA10]. Since the denoted study concentrated on KS-alloy, the suggested  $m$ -value has been adopted in this dissertation. Such a decision was made after consultation with Simufact.forming developers. The background solver of Simufact.forming submits the function in equ. 3.10 in order to express the yield criterion as follows [ZHAN13b].

$$f = a \cdot |K_1 + K_2|^m + a \cdot |K_1 - K_2|^m + c \cdot |2K_2|^m \quad (3.10)$$

$$K_1 = \frac{\sigma_{xx} + h \cdot \sigma_{yy}}{2}$$

$$K_2 = \sqrt{\left(\frac{\sigma_{xx} - h \cdot \sigma_{yy}}{2}\right)^2 + p^2 \cdot \sigma_{xy}^2}$$

$a$ ,  $c$ ,  $h$  and  $p$ : Material constants

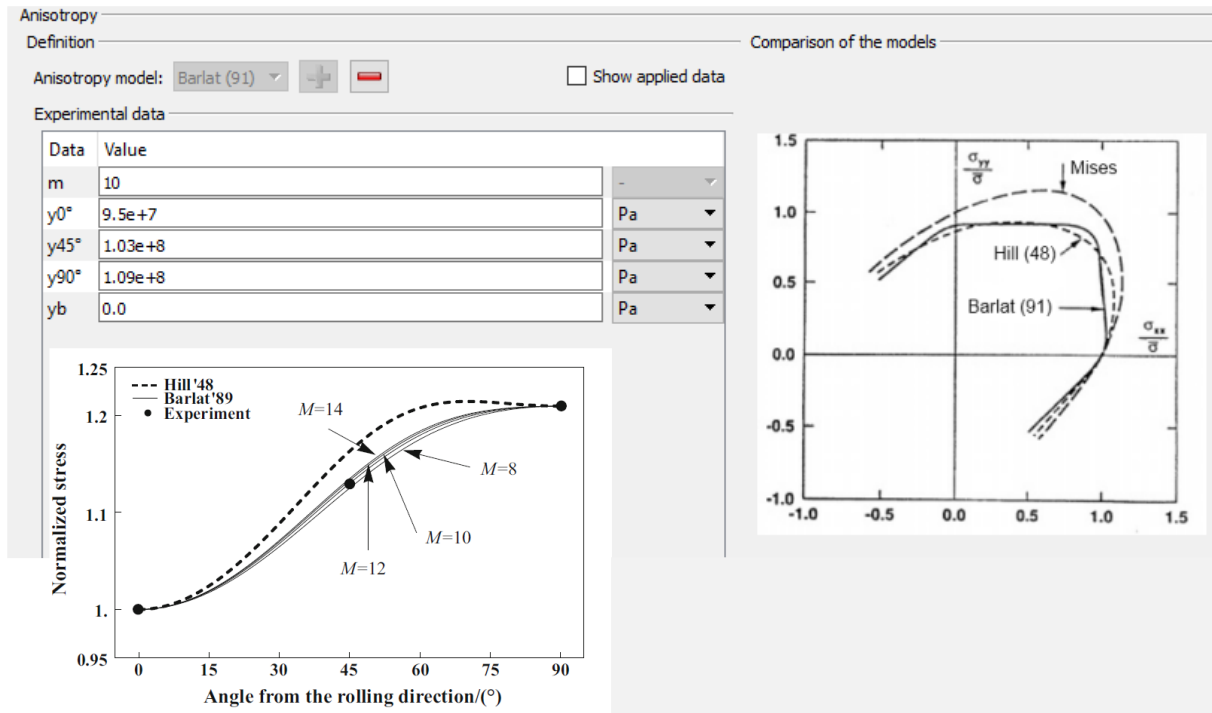


Figure 3-12: Definition of anisotropy in the simulation tool, screenshot Simufact.forming

[KOT14b] and before [JURE13] proved a better matching of the Baralt model upon Hill48 in the case of titanium alloys at RT. Hill48 is still preferred at elevated temperatures, as confirmed by Simufact.forming developers. However, both models are submitted in our simulation study with more concentration on the Hill48 criterion.

### 3.5.2 Setting up the FE-model

After establishing a material model for each regarded alloy within this study, an FE model can be generated. The following tree in figure 3-13 describes the sequence of the model setup.

A hydraulic press is used to achieve the forming stage with a constant velocity of 3.4 mm/s. The latter value is adopted according to previous experimental fabrication of components by our partner, FormTech. The second step comprises the geometry of the punch, blank holder, and cavity, respectively. The coefficient of friction is defined according to Coulomb. Its value has varied within this approach. The tree shown below is merely an example of model adjustment. For the whole tool parts,  $\mu_f$  is assigned identically. Temperature should also be assigned to both tool parts and the workpiece. The forming process is adapted to be implemented with a warm tool, whose temperature is similar to the workpiece, and is conducted isothermally, i.e., the heat transfer coefficient is not considered.

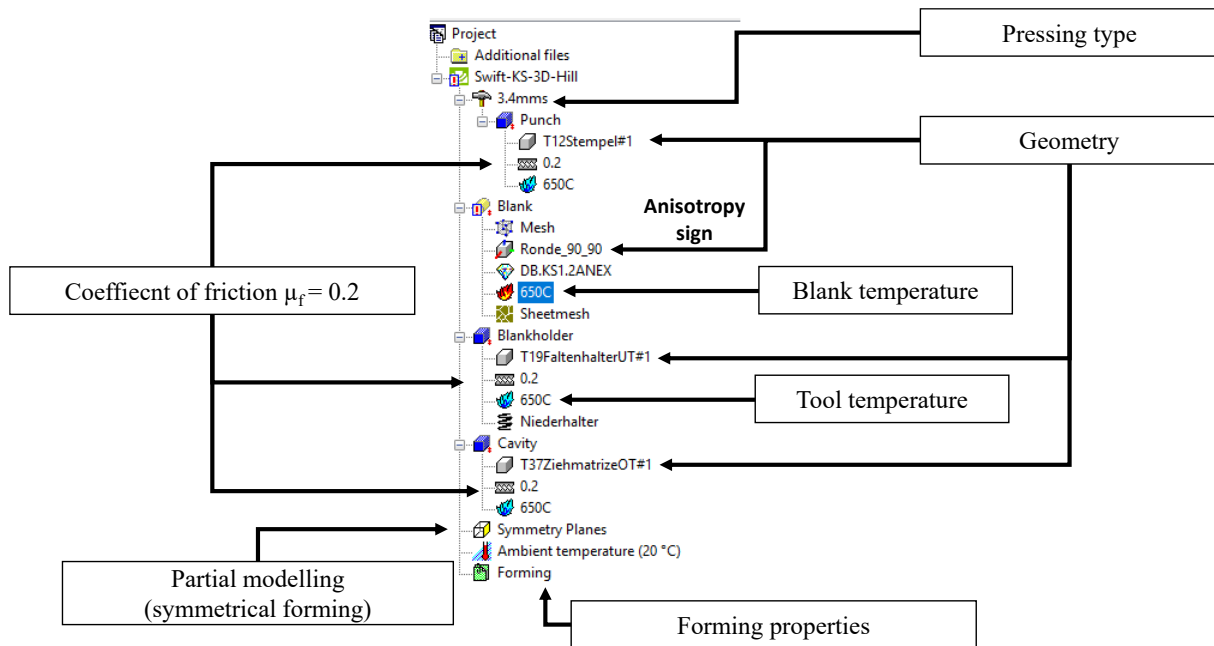


Figure 3-13: Tree of the simulation model setup, screenshot Simufact.forming.

However, variation of blank temperature is also a part of the approach within the study to estimate the best parameters of HCF numerically. An item of the symmetry plane enables a partial numerical calculation of the forming process, providing that the forming process is symmetric. Consequently, the solving time will be reduced to a quarter of the original value if merely a quarter of the component is regarded. A forming properties window is popped-up to define the forming properties more specifically. Here, the springback behavior can be obtained if the draw-back box is checked. In addition, contact between each two adjacent tool parts and the sheet is defined to avoid any possible convergence problem, which leads to detention during the solving process.

Unfortunately, a creep model cannot be involved in the explicit FEM, which is used in Simufact.forming to simulate the forming stage. So, the relaxation phase cannot be FE-modeled in Simufact.forming. Therefore, a draw-back stroke does not make any sense anymore. HCF is simulated in our case until the end of the forming stage.

### 3.5.3 Validation of FE-model with Swift<sup>®</sup> component

The prepared FE model needs to be validated by modelling a component that has already been industrially fabricated. Needless to say, the parameters of the simulation should be identical to those of the manufacturing process. In cooperation with industry partner, FormTech, the parameter of an already formed swift<sup>®</sup> component is adopted. Figure 3-14 shows a sketch of the formed swift.

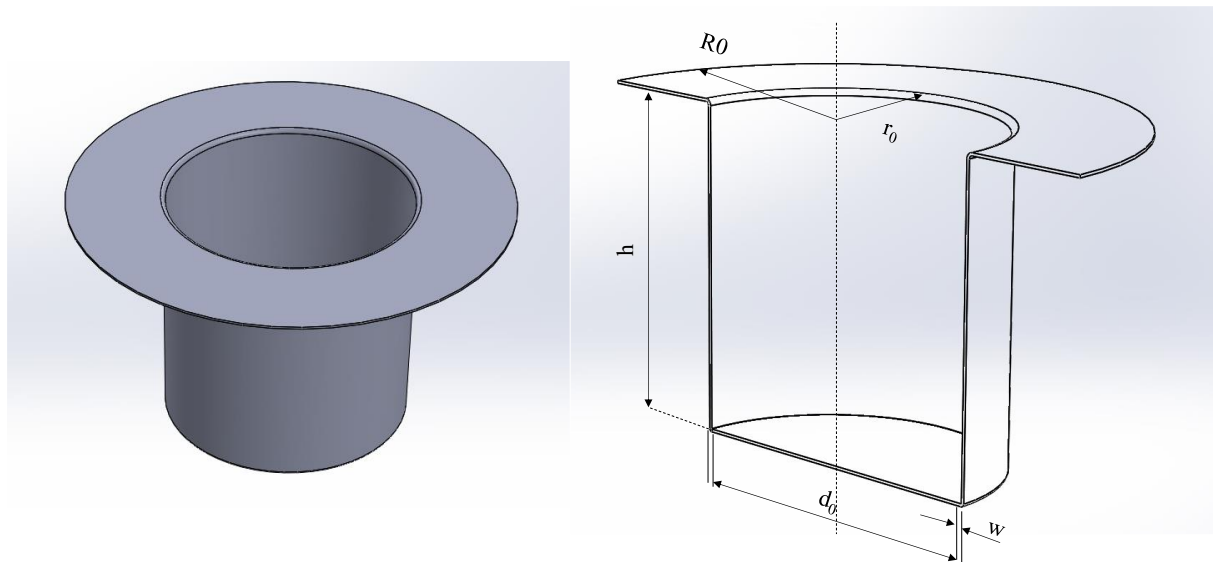


Figure 3-14: Swift<sup>®</sup> component

So, forming parameters are adopted from reality and rebuilt in favor of a simulation model. Table 3-7 concludes the whole adjusted parameters within the validation model. As can be noticed, parameters are not varied in this stage. At the end of the simulation, a couple of results can be compared with the real part. An important output is the required pressing force during the forming process. Other features to be noticed are thickness distribution, thermal distribution, and the possible presence of ears.

Model- No.	Material	T [°C]	R <sub>0</sub> [mm]	r <sub>0</sub> [mm]	h [mm]	W [mm]	F <sub>bh</sub> [kN]	μ <sub>f</sub> [--]	F <sub>p</sub> [kN]
1	XT	715	90	50	45	0.9	25	0.35	.....
2	XT	650	90	50	45	0.9	25	0.35	.....
3	XT	650	90	50	90	0.9	25	0.35	....
4	KS	670	90	50	45	0.9	30	0.35	.....
5	Gr.04	660	90	50	45	0.9	30	0.35	.....

Table 3-7: Forming parameter set of swift<sup>®</sup>, Data provided by FormTech.

### 3.5.4 FE-study on an aerospace component

After validation of the FE model, the plasticity behavior of the titanium α-alloys is numerically investigated in comparison to Ti6Al4V. Here, parameters listed in table 3-7 will be varied frequently to adopt a set of parameters of high consistency. Such a variation will be achieved based on the results of stretch forming conducted as described in sections 3.3 and 3.4. The main form of the half-shell is shown in figure 3-15.



*Figure 3-15: Half-shell of a t-duct, Courtesy of FormTech GmbH*

Outputs of this stage would be the effective stress and strain, thickness and thermal distribution, formation of earing, and pressing forces. It will also reveal the best alloy with regard to plasticity. These results are attempted to be reproduced by manufacturing a half-shell of a t-duct. However, any further investigation within this dissertation will be conducted based on the results of the numerical study.

### **3.6 Examination of the t-duct**

A half-shell of an aerospace t-duct was intended to be produced via HCF by the industrial partner, FormTech. However, one  $\alpha$ -alloy is nominated to be chosen for this target. A similar component is also made of Ti6Al4V to fulfill the comparison with it. Moreover, the critical positions of the t-duct are detected during the FE-study described in section 3.5.4, and samples of these positions are investigated metallographically according to the examination explained in section 3.3.3.

### **3.7 Conclusion of the experimental procedure**

The whole approach can be concluded with the following points:

- KS, XT, and Gr.04 are characterized by tensile tests at RT and elevated temperatures. A fatigue test at RT is also conducted.
- HCF behavior of the alloys mentioned above is investigated utilizing the relaxation test at the temperature range 400-800°C.
- FEM is implemented to adapt the best set of parameters during HCF.

- 
- An aerospace component is produced via HCF based on results obtained out of the whole previous approach.
  - Material properties are detected on samples cut out of the produced component.
  - A comparison between the HCF behavior of Ti6Al4V and the regarded titanium  $\alpha$ -alloys is also made.

## 4 Results and discussion

In the following, the results of the whole approach will be depicted in a similar sequence to the former description of the experimental procedure.

### 4.1 Tensile test at RT

The tensile test has been conducted on KS, XT, Gr.04, and Ti6Al4V. Results are depicted as graphs in figure 4-1 and concluded in table 4-1 and figure 4-2.

KS exhibits the higher ductility among all the regarded alloys. Its elongation to fracture seems to be double that of Ti6Al4V. The latter alloy has the least ductility at room temperature. With regard to strength, Ti6Al4V does possess the highest ultimate strength, as expected, while KS possesses the lowest one. Gr.04 is the stronger among  $\alpha$ -alloys, and its ultimate strength goes far near Ti6Al4V. However, its ductility is the least among  $\alpha$ -alloys. XT shows an intermediate ductility among regarded alloys. It is important to remember that Ti6Al4V is studied under non-treated conditions, i.e., heat treatment of such an alloy would change its mechanical properties positively. KS and XT exhibit the most pronounced yield strength. However, the other titanium alloys imply it as well. A remarkable matter obtained from the graphs is the different behavior after necking. Ti6Al4V exhibits an accelerated fracture after necking, while  $\alpha$ -alloys diffuse more beyond the uniform elongation. The most extensive elongation after necking is remarked in the case of KS. The difference between  $\epsilon_B$  and  $\epsilon_{gl}$  can be read in table 4-1. Such behavior was noticed by [BADR15] and ascribed by anisotropy. Figure 4-1 also signalizes the material anisotropy of all alloys at different rates, which is also described in table 4-1. KS exhibits the highest difference in yield strength in dependence on specimen orientation. The ultimate strength of Gr.04 with  $0^\circ$  specimen is equal to  $45^\circ$ . The uniform elongation is, however, quite different. The typical anisotropy of titanium alloys was illustrated in [SUWA14], that the strength at  $90^\circ$  is higher than elsewhere. Such a phenomenon is mostly observed in the case of Gr.04 and XT. All in all, titanium alloys sound to have an obvious material anisotropy at room temperature. R-values are depicted in figure 4-2 and confirm this statement. Moreover, plasticity strength ( $\sigma_{pl} = US - YS$ ) is relatively small in all cases, i.e., the strain hardening up to the uniform elongation is barely noticeable. XT with  $90^\circ$  specimen does not reveal any strain hardening in the plastic area, while a tiny  $\sigma_{pl}$  with  $45^\circ$ . The latter strength is very small, with  $45^\circ$  and  $90^\circ$  for KS compared to  $0^\circ$ . However, strain hardening for Gr.04 and Ti6Al4V is much higher, implying better drawability for KS and XT at room temperature.

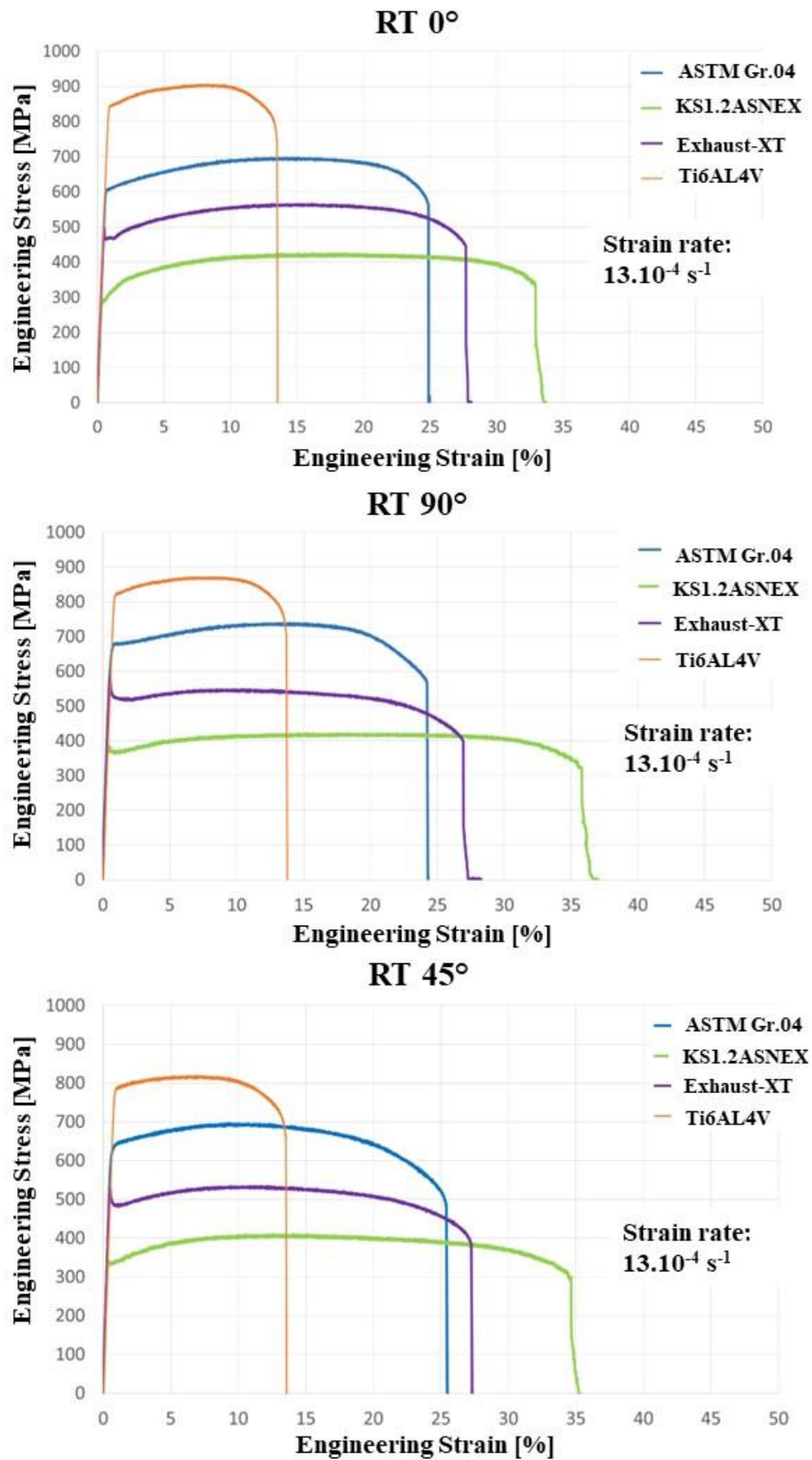


Figure 4-1: Stress-strain curves at RT

The lower ultimate strength with higher elongation before fracture distinguishes KS from XT, though. Apparently, oxygen content plays a major role in increasing the strain hardening with Gr.04 in the case of  $\alpha$ -alloys, see table 3-1. The effect of Si and Nb content on XT and KS creep behavior sounds to be minor. This will be studied further.

The potential of springback can be explained based on the E-modulus obtained from table 4-1. As can be seen, E-modulus ranges between [105 and 117] at room temperature. The more elastic energy causing springback behavior, the higher the ratio  $Y_S/E$ . According to this statement, the high yield strength of Ti6Al4V with relatively low E-modulus compared to  $\alpha$ -alloys implies a high potential for springback.

[MPa]	0°				45°				90°			
	Ti64	Gr.04	KS	XT	Ti64	Gr.04	KS	XT	Ti64	Gr.04	KS	XT
YS	845	600	290	490	777	640	326	525	820	675	380	585
US	905	700	424	565	820	695	410	535	870	740	420	
$\epsilon_{gl}$ %	8	15	16	16	7	10	14	12	8	14	15	-
$\epsilon_B$ %	14	25	33	27	14	25	35	26	13	24	35	26
E. [10 <sup>3</sup> ]	110	105	105	108	108	114	111	107	100	111	117	113
r-value	-	4.25	2.8	2.7	-	4.9	3.1	4.95	-	5.35	4	5
Poisson	$\approx 0.35$ [DONA00]											

Table 4-1: Mechanical properties at RT

In any case, elongation to fracture and the Poisson ratio are independent of the specimen orientation, as seen in table 4-1. Figure 4-2 also shows  $\epsilon_B$  values besides  $r_m$  ones. A similar study was conducted by [JURE15] on KS, showing consistent results with the current ones.

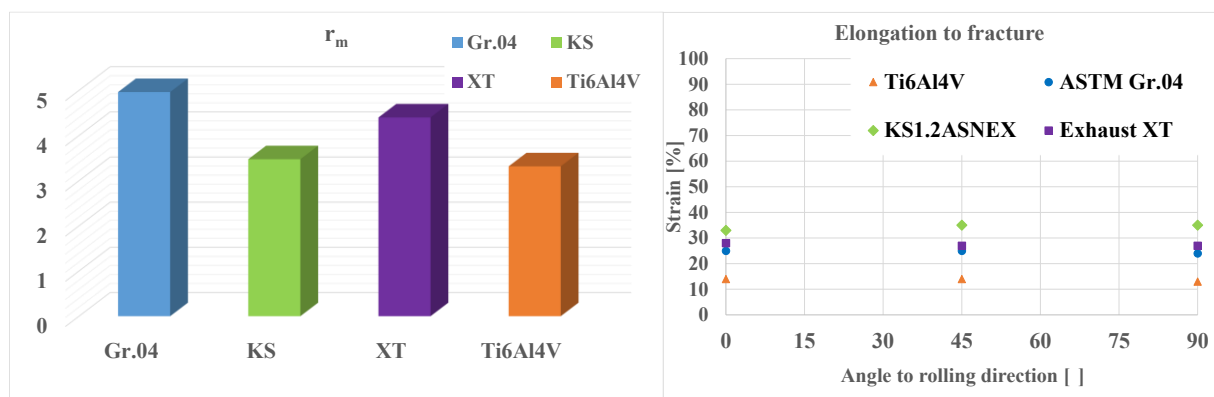


Figure 4-2: Elongation to fracture and  $r_m$ -value depending on the angle to the rolling direction. Values for Ti6Al4V: courtesy of [BADR16].

## 4.2 Metallographic examination at RT

### 4.2.1 Microstructure at RT

The optical microscope was used to obtain a representative micrograph made with a 100  $\mu\text{m}$  scale to characterize the studied titanium alloys. Ti6Al4V micrograph reveals  $\beta$ -grains in white color covering  $\alpha$ -ones, while the other micrographs reveal a single-phase structure.

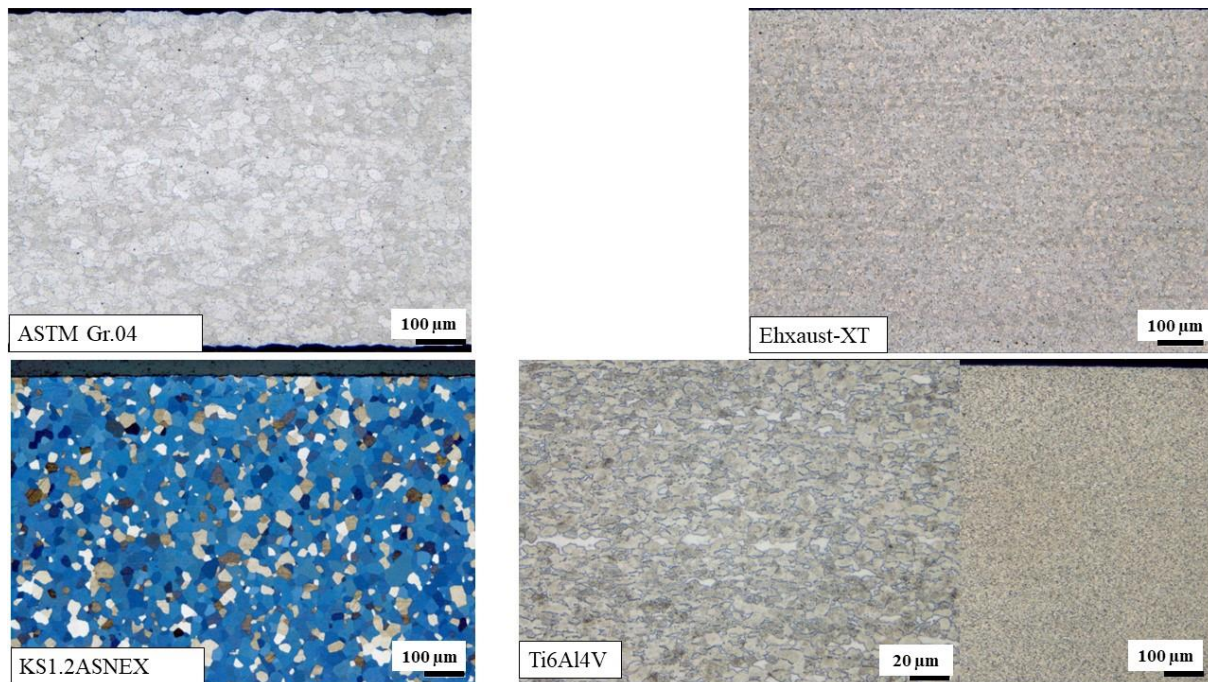


Figure 4-3: Microstructure of titanium alloys at RT, scale: (100  $\mu\text{m}$ ) and (20  $\mu\text{m}$ )

The equiaxed microstructure obtained in figure 4-3 does not imply any twinning deformation anyhow. The highly fine-grained microstructure explains the high strength of Ti6Al4. The discovered anisotropy with it limits its cold-forming potential, though. On the other hand, the G-index of XT represents an illustration of its high strength with high ductility compared to the lower strength of KS. However, all the studied alloys can be ascribed to a fine-grained structure according to the classification depicted in table 3-4.

The difference in G-index is a result of variability in the starting material and cannot be a consequence of grain growth, as long as G-index denotes a fine-grained microstructure. Table 4-2 summarizes the G-index number of each studied alloy at RT and confirms the statement about their fine-grained microstructure with a mean G-index above 7 for all the cases.

Alloy	G- 0°	G- 45°	G- 90°	G- mean
KS	7.5	7.5	7.5	7.5
XT	11	11	11	11
Gr.04	8	8	7.5	7.8
Ti6Al4V	10.8	11.3	11.8	11.3

Table 4-2: G-index at RT according to ISO 643.

#### 4.2.2 Texture at RT

R-value gives a rough idea about the dependence of the material properties on the orientation. However, such information seems not to be sufficient to describe the anisotropic behavior of the material. For this reason, a corresponding textural observation describes it profoundly. In figure 4-4, PF and IPF with EBSD mapping illustrate the grain orientation at RT, assuming A1 and A2 are RD and TD, respectively.

As seen in figure 4-4, an EBSD map in the RD-TD plane with a projection plane (001) emphasizes the high texture of KS at RT and the predominance of the basal plane (0001) parallel to RD and TD according to the predominance of the red color within the map. Since more than 30% of the grains shown in the map have nearly a similar orientation, a technical texture can be assigned to KS, XT, and Gr.04.

However, PF from Gr.04 and XT, respectively, is evidence that the basal pole is inclined to TD with a split around ND as expected. Contrary to the typical texture of  $\alpha$ -alloys, PF from KS shows a high probability of grains projection on the basal plane (0002) with more inclination to RD. These abovementioned differences can be the consequence of the highest ultimate strength of KS in RD, while US of Gr.04 and XT are the highest in TD.

The phenomenon observed with PF from KS is expected to be present in the case of Ti6Al4V, which is confirmed by its own PF, as seen in figure 4-4. However, the prismatic plan (101-1) of KS is less occupied than others, which is the most occupied in the case of Ti6Al4V.

EBSD map for KS and Gr.04 implies a tiny twinning mode deformation as defined in [LIU01]. Maps reveal an orientational gradient within some grains, denoting twins, while the map of XT does not reveal any twins. This is a meaningful reason for the relatively small strain hardening observed in these alloys at RT.

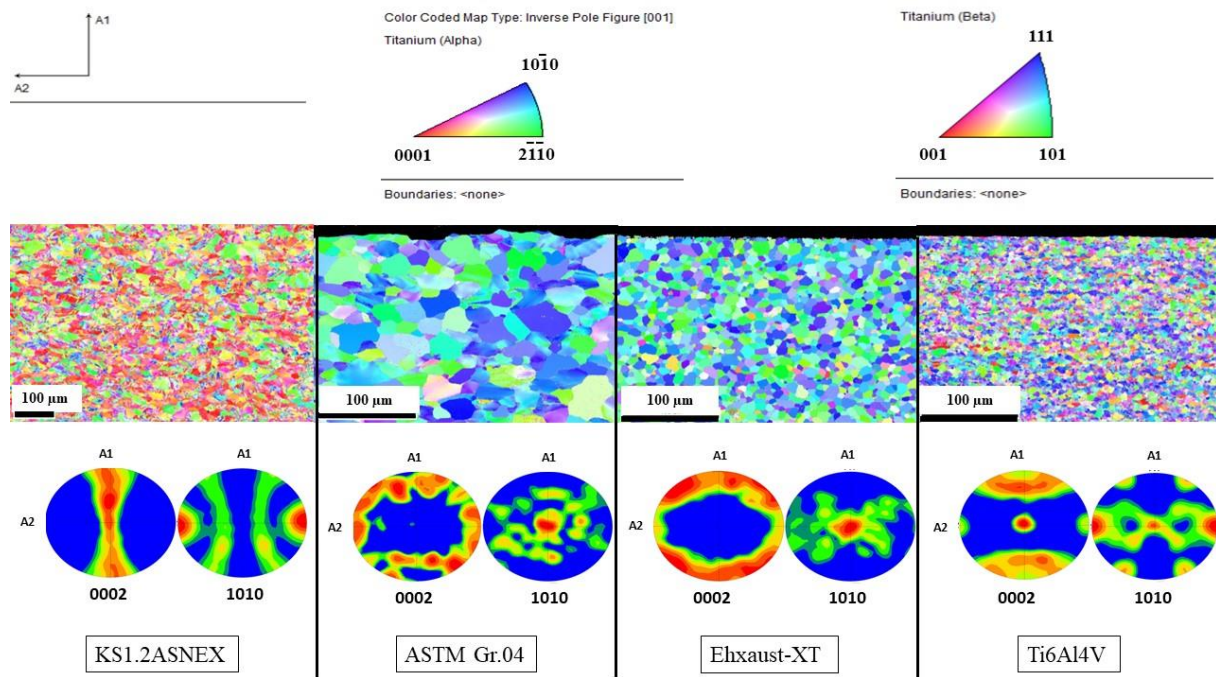


Figure 4-4: Pole figures and inverse pole figures [001] of the studied alloys at RT.

#### 4.2.3 Hardness at RT

The measured hardness values were analogous to the strength values obtained within the study and shown in table 4-3. As expected, Ti6Al4V possesses the highest hardness number, according to Vickers. Owing to its highest oxygen content among the studied  $\alpha$ -alloys, Gr.04 exhibits the highest hardness number, followed by XT and KS with the lowest hardness. Table 4-3 concludes every hardness number measured at RT. Since hardness is a superficial feature of the material, it is also expected that material anisotropy does not emerge, and there is no tendency of hardness in dependence on the sample orientation. Another matter to be considered is that the hardness number could be impacted by material treatment. So, Ti6Al4V might exhibit another hardness range if it is chemically or thermally treated, for instance. A comparison between the hardness number at RT and elevated temperatures will be shown later.

Hardness number according to Vickers [HV0.5]				
Direction Alloy	0°	45°	90°	Mean hardness number
KS1.2ASNEX	165	162	165	164
Exhaust-XT	184	190	188	187
ASTM Gr.04	247	256	248	250
Ti6Al4V	320	310	315	315

Table 4-3: Hardness number for all the studied alloys according to Vickers at RT.

### 4.3 Fatigue test at RT

Based on the results obtained in section 4.1, KS seems to have the best ductility and creep-forming potential among the studied alloys. For this reason, a fatigue test was conducted to characterize its durability under dynamic loadings.

As illustrated in section 3.3.4, the Wöhler curve was deduced with the implementation of equ. 3.6 and assuming the lognormal distribution of the values of  $\sigma_D$ . Figure 4-5 depicts the plotted curves according to Gnedenko-ansatz.

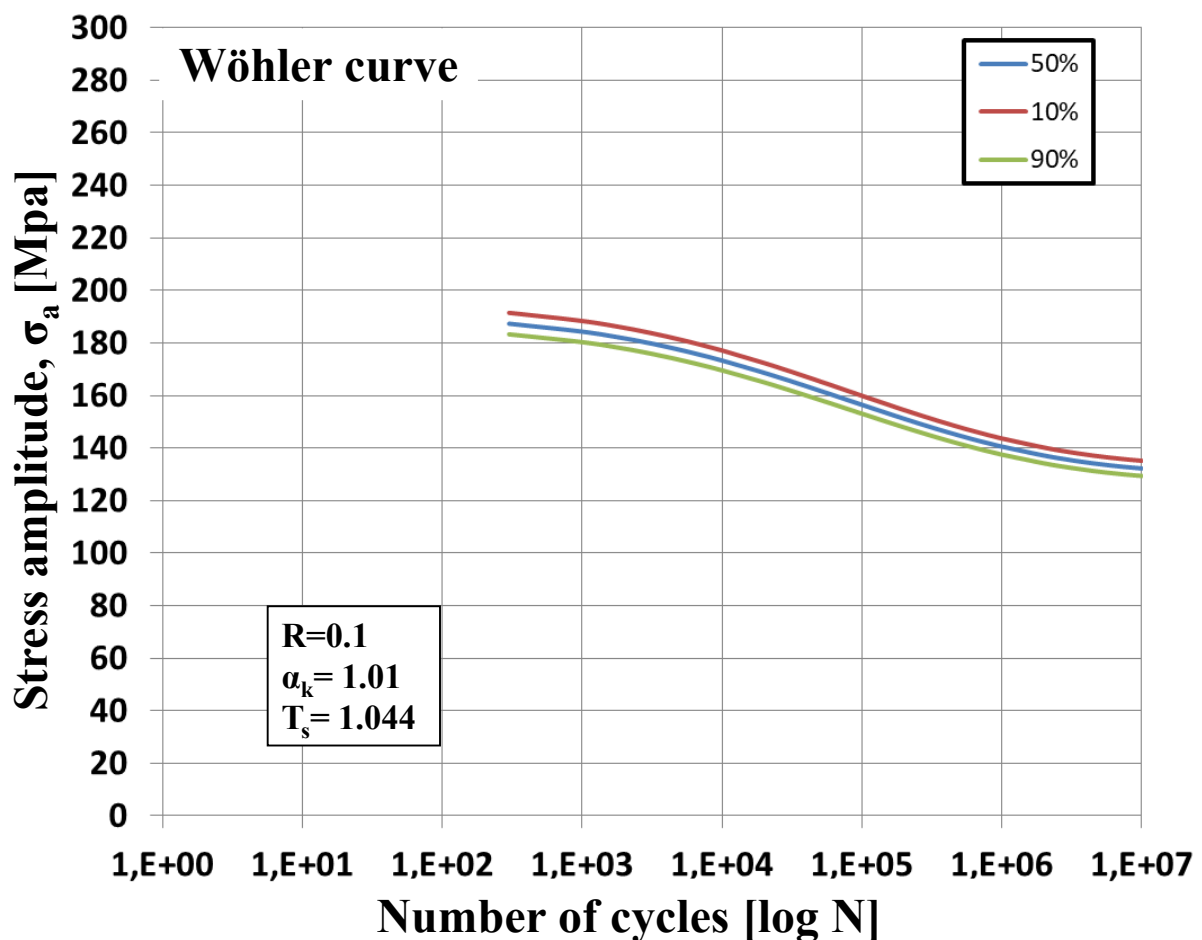


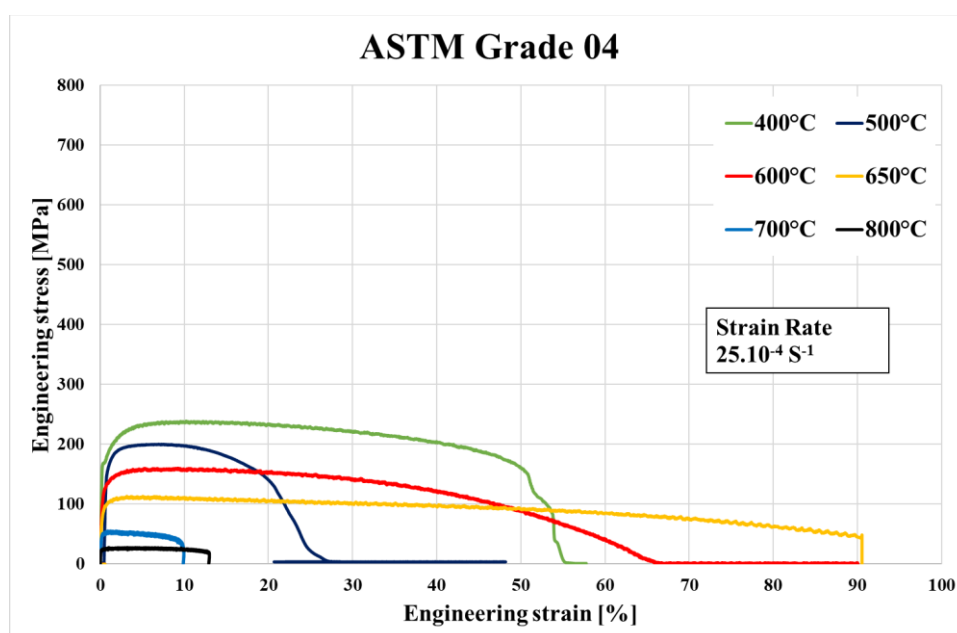
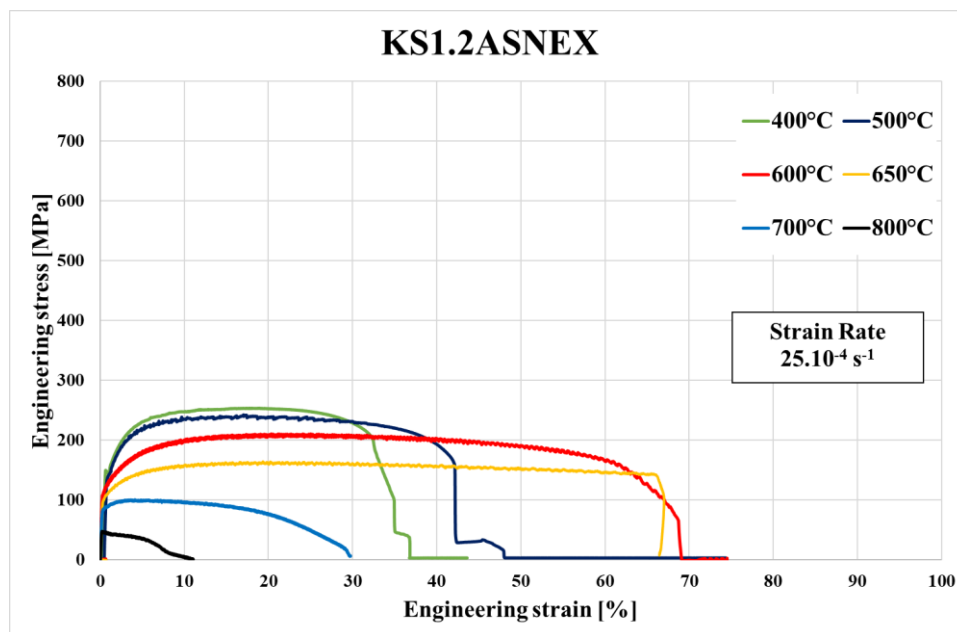
Figure 4-5: Wöhler curve for KS according to Gnedenko at RT.

The amplitude of the fatigue stress is approximately  $\sigma_a = 155$  MPa. The stress ratio of  $R=0.1$  indicates an alternated load in the tension-tension stress range. In this case,  $\sigma_D$  can be deduced by the following term:  $\sigma_D = \frac{\sigma_a}{0.45}$ . Consequently, the fatigue stress amounts to approximately  $\sigma_D = 345$  MPa. The form factor  $\alpha_k$  is nearly one means the test was made without any stress concentration. The scatter band  $T_s$  is also relatively narrow, with a value very close to 1. Its low value confirms the consistency of the extrapolation with the lognormal distribution for the

experimental results. According to such a result, it can be stated that a dynamic load with resulting stress of 345 MPa can KS endure for a duration of ten million cycles with a very high probability since  $T_s$  possess a very low value.

#### 4.4 Tensile test at elevated temperatures

Results will be shown in this section in a similar way to sections 4.1 and 4.2. However, a comparison between the results of both sections will be presented as well. Results of the tensile test at 400°C to 800°C with an interval of 100°C are displayed in figure 4-6.



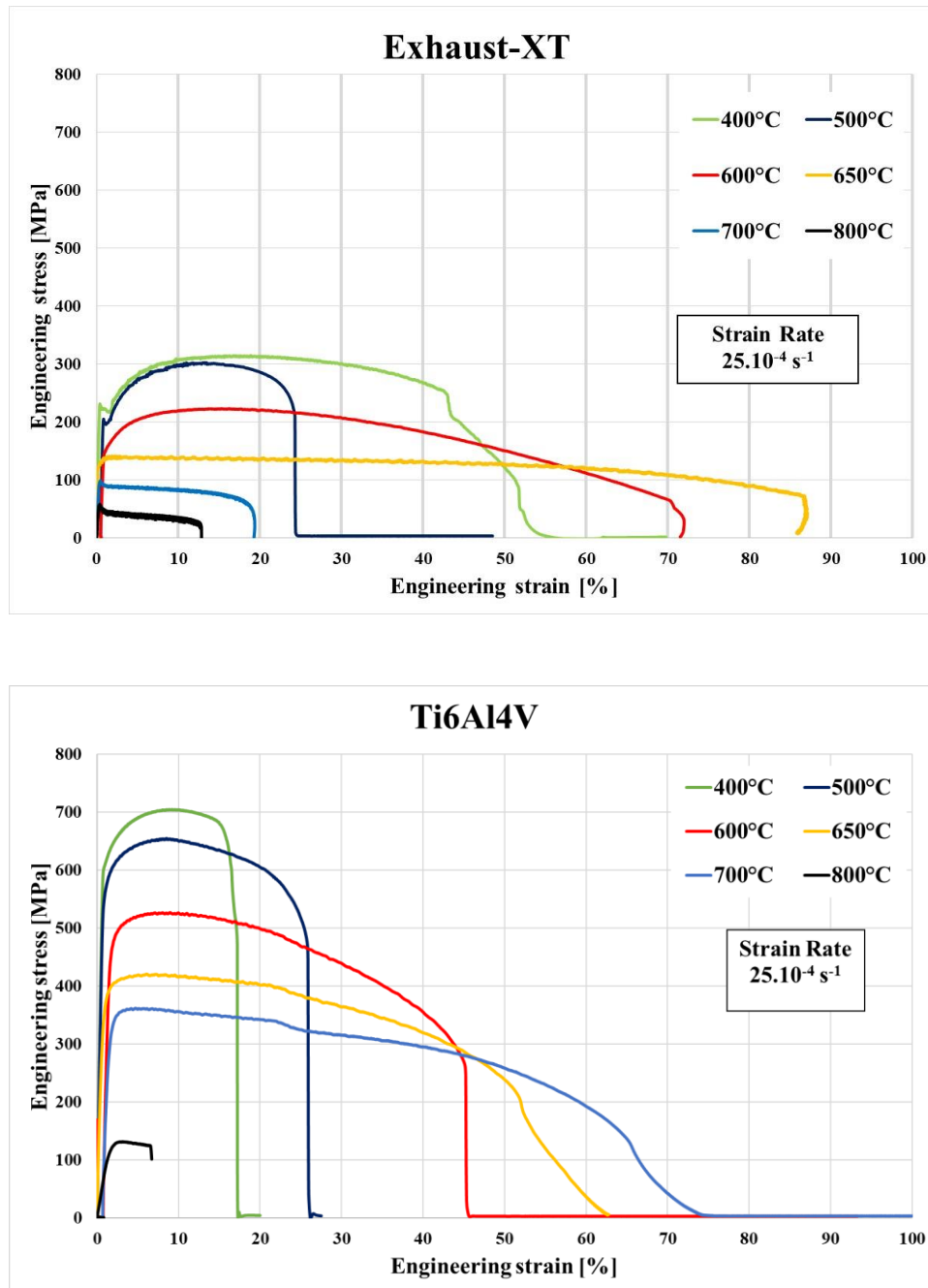


Figure 4-6: Stress-strain curves at elevated Temperatures for KS, Gr.04, XT, and Ti6Al4V.

However, a tensile test at 650°C was added afterward since all regarded  $\alpha$ -alloys have a wide variation of tensile behavior between 600 and 700°C. As can be seen in figure 4-6, ductility increases proportionally with temperature levels up to 650°. The tensile test at 700°C shows a declination of ductility in the case of  $\alpha$ -alloys so that  $\epsilon_B$  drops from 90% to 10% in the worst case. Such a descent ductility at 700°C can be mostly observed with Gr.04. Ti6AL4V reveals a very good elongation to fracture, on the other hand. However, a similar phenomenon is observed with the results of the tensile test at 800°C for all studied alloys, including Ti6Al4V. This can be ascribed to the high diffusability of oxygen starting from 700°C, resulting in the

presence of  $\alpha$ -phase enriched by interstitial oxygen with a solubility of 34%. It is the formation of  $\alpha$ -case. Ti6Al4V possesses a significant amount of Al, which retards the formation of  $\alpha$ -case by the formation of the desired  $\text{Al}_2\text{O}_3$  upon  $\alpha$ -phase with a high solution of oxygen. For this reason, it can be stated that the ductility of Ti6Al4V at 700°C is better than  $\alpha$ -alloys in general [LEYE03]. Up to 650°C,  $\alpha$ -case cannot affect the mechanical properties, and hence, the ductility of  $\alpha$ -alloys is remarkably better than Ti6Al4V. Regarding the shape of the stress-strain curve, it still has the typical shape of the curve with a pronounced yield point. Although XT and Gr.04 exhibit higher  $\epsilon_B$  than KS in the best case of each, KS is nominated to hold the best drawability, where the plasticity before necking, i.e.,  $\epsilon_{gl}$ -value, is the decisive feature. Looking at the stress-strain curve at 650°C respectively, the value of  $\epsilon_{gl}$  for KS amounts to ca. 20%, while such a uniform elongation for XT and Gr.04 amounts to 2% and 3.1%, respectively. These are listed in table 4-4, besides other mechanical properties obtained from the tensile test at elevated temperatures.

Alloy T [°C]	YS [MPa]				US [MPa]				$\epsilon_{gl}$ [%]			
	Ti64	Gr.04	KS	XT	Ti64	Gr.04	KS	XT	Ti64	Gr.04	KS	XT
400	600	162	141	225	705	239	248	315	8.85	10.2	21	19
500	540	142	133	190	655	200	242	303	8.52	7.2	17	13.3
600	420	110	104	136	527	160	210	223	8.9	9.2	20.3	16.3
650	360	70	90	120	420	113	165	141	6.1	3.1	19.3	1.9
700	290	40	84	90	360	55	100	98	4.69	1	4.1	0.5
800	110	20	45	55	130	27	47	58	3.12	5.4	0.22	0.4

Table 4-4: Mechanical properties obtained from tensile test at elevated temperatures.

Ti6Al4V maintains its strength even at a high temperature like 600°C. Owing to its meaningful Al-content, the strength does not decrease drastically with higher temperatures. A similar phenomenon is also observed in the case of XT, whose Si-content secures thermal stability up to 600°C. Starting from 700°C, all studied  $\alpha$ -alloys undergo a structural softening so that a work hardening is barely observed or even not found at all. However, such a softening at 700°C is not notified with Ti6Al4V. The mechanical properties of Gr.04 are the most remarkable at high-temperature levels. The ultimate strength becomes lower than KS, regardless of the temperature level observed within the warm forming level. In addition, a remarkable brittleness appears at 500°C for both Gr.04 and XT.

Alloy	r-value T [°C]	r <sub>0</sub>	r <sub>45</sub>	r <sub>90</sub>	r <sub>m</sub>
	KS1.2ASNEX	400	1.1	2.1	3.2
500		1.15	1.93	2.26	1.8175
600		0.97	1.72	1.63	1.51
700		0.8	1.25	1.1	1.1
800		0.76	1.27	1.5	1.2
Exhaust-XT	400	1.38	2.23	4.1	2.485
	500	1.4	2.1	2.34	1.985
	600	1.4	2.53	4.55	2.7525
	700	1.04	1.58	1.32	1.38
	800	0.89	1.11	1.06	1.0425
ASTM Gr.04	400	3.26	2.85	3.49	3.1125
	500	1.22	3.5	0.45	2.1675
	600	0.73	2.72	0.15	1.58
	700	0.54	1.22	1.11	1.0225
	800	0.58	1.3	1.27	1.1125

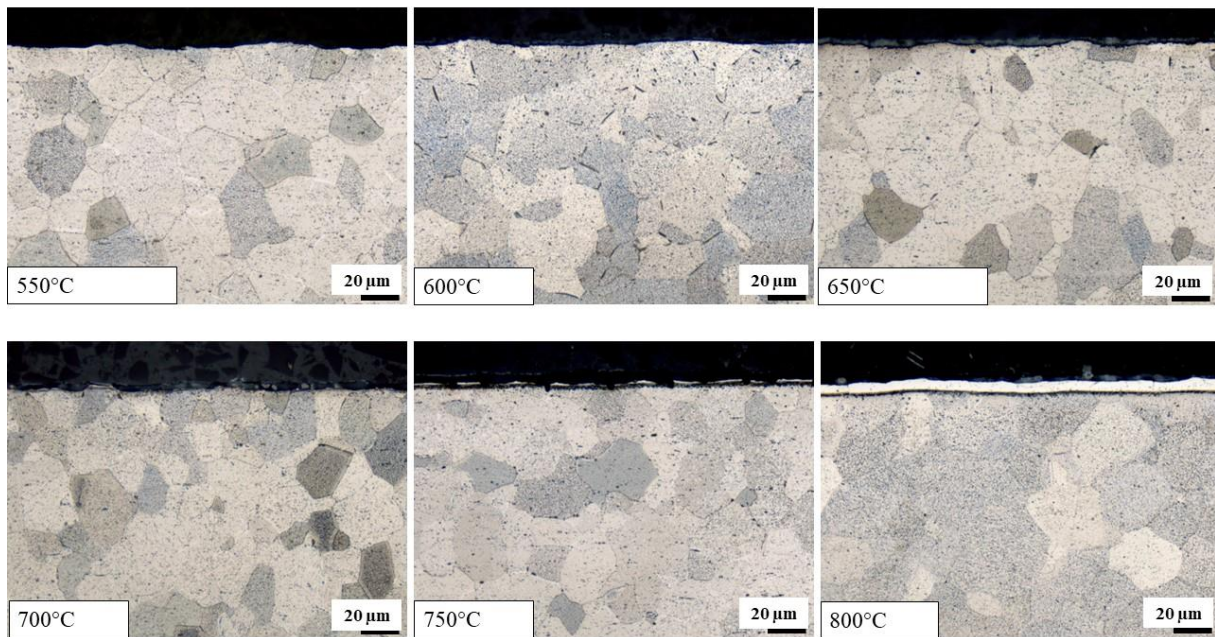
Table 4-5:  $r_m$ -Value at elevated temperatures obtained according to ISO 10113.

This would be justified in a metallographic manner. Such an observation is confirmed by the  $r$ -value presented in table 4-5. It is obvious that the  $r$ -value at 700°C and 800°C is lower than elsewhere in all cases. In case Gr.04  $r_{90}$  at 500°C and 600°C is quite low, denoting a bad drawability if loading would be parallel to TD. However,  $r_m$ -values match the definition of good drawability with a wide strain hardening area at the stress-strain curve, i.e., the wider this area, the bigger  $r_m$ -value (refer to chp. 2.2.2.3). Such a statement is proven by comparing values from table 4-5 with the path of stress-strain curves in figure 4-6.

## 4.5 Metallographic examination at elevated temperatures

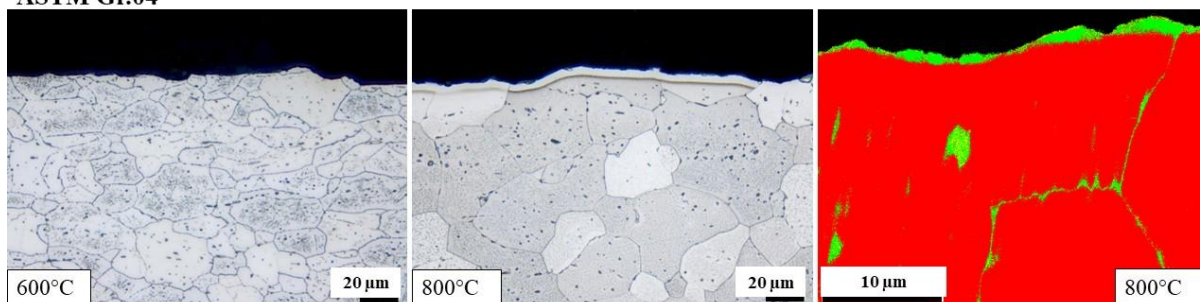
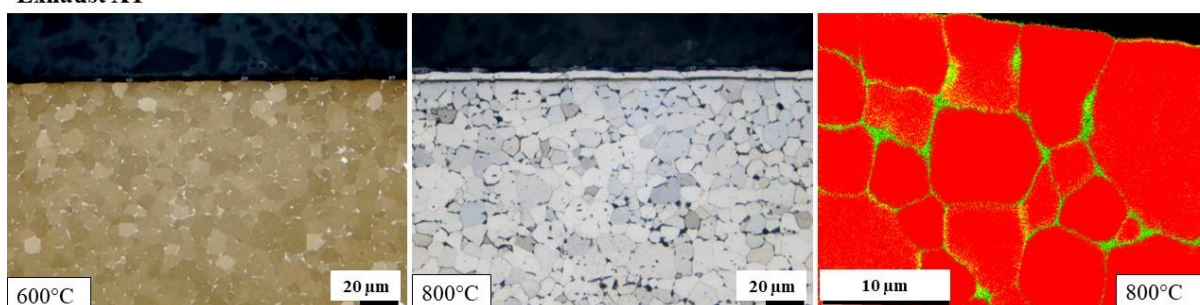
### 4.5.1 Microstructure at elevated temperatures

The study of microstructure gives information about the oxidation behavior of the materials. In figure 4-7, the microstructure of KS is obtained from tensile samples used in the previous section at various temperature levels.

**KS1.2ASNEX**

*Figure 4-7: Microstructure of KS at elevated temperature.*

Obviously, KS resists the formation of oxide scale up to 700°C. Starting from forming at 750°C, an inconstant white layer at the surface emerges. Such a layer becomes readily wider at 800°C and denotes the higher oxygen solubility in  $\alpha$ -phase with an increased temperature. The microstructure of Gr.04 and XT is shown in figure 4-8. (In figure 4-8, the red color is for  $\alpha$ -phase, the green color for titanium dioxide ( $\text{TiO}_2$ ), and the yellow one for titanium (III) oxide ( $\text{Ti}_2\text{O}_3$ )).

**ASTM Gr.04****Exhaust XT**

*Figure 4-8: Microstructure of Gr.04 and XT at elevated temperatures.*

Besides the micrographs taken at 600°C and 800°C, an EBSD mapping explains the phase distribution. A similar behavior, deduced from figure 4-7, is observed in figure 4-8 with respect to XT and Gr.04. However, EBSD phase mapping at 800°C implies a thin TiO<sub>2</sub> superficial layer, thinner than the white layer in the corresponding micrograph. Indeed, the white layer has the same phase as the base metal, namely an  $\alpha$ -phase.

This fact confirms the issue that the formation of the  $\alpha$ -case layer is predominant upon the formation of oxide scale in  $\alpha$ -alloys, and it is quite hard to distinguish between the TiO<sub>2</sub> layer and the  $\alpha$ -case one with such a micrograph obtained by light microscope. For this reason, EDX-method with EBSD helps to make this differentiation. However, such a phenomenon arises from 750°C, denoting an excellent oxidation resistance up to 750°C for  $\alpha$ -alloys. SEM investigation enhances the statement above and shows the difference in phase identification between position (a) and (b) as depicted in figure 4-9 for KS at 800°C. The comparison between phases in both positions denotes a high Ti<sub>x</sub>O<sub>x</sub> content at the surface, which is not recognized in the base material.

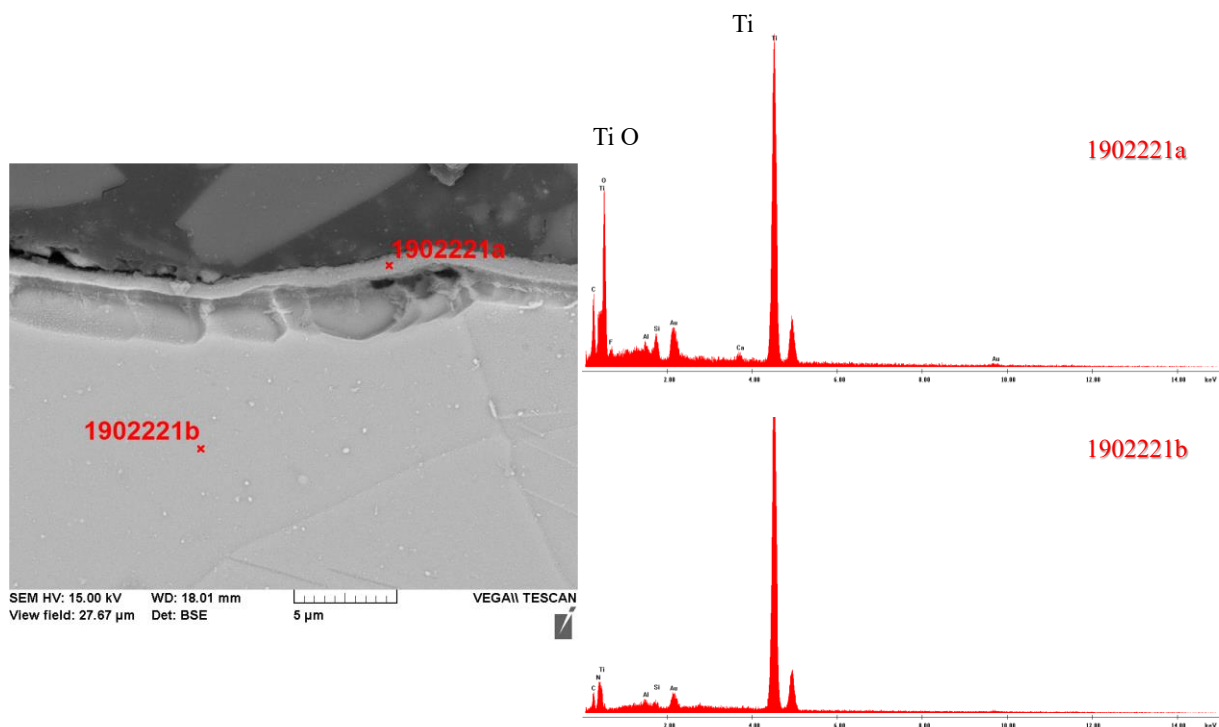
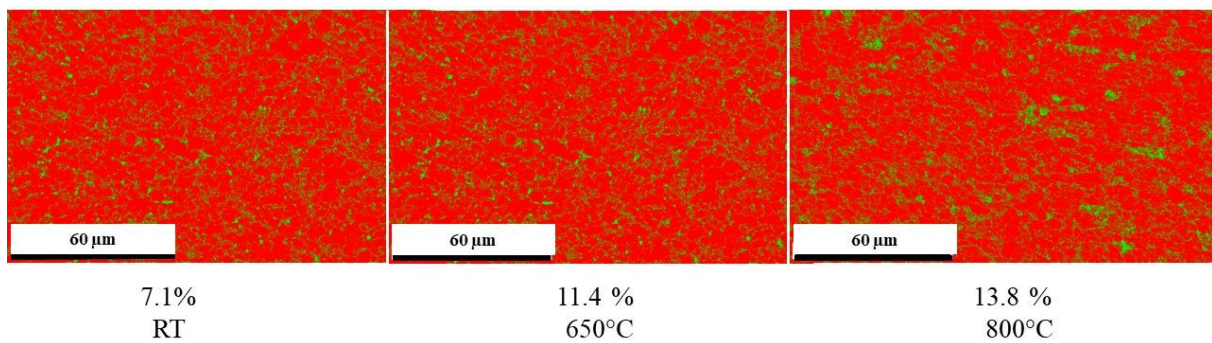


Figure 4-9: SEM for KS at 800°C, recognition of Ti<sub>x</sub>O<sub>x</sub> phase at the surface.

On the other hand, the evolution of  $\alpha$  and  $\beta$  phases in dependence on temperature was observed in the case of Ti6Al4V. In figure 4-10, the collection of  $\beta$ -lamellae on the grain boundaries of  $\alpha$  is highlighted by the green color. The volume fraction of the  $\beta$ -phase increases rationally with increasing temperature. Such a volume fraction almost doubles from 7.1% to 13.8%,

corresponding to the temperature variation from RT up to 800°C. It should impact the forming behavior of the alloy as well as its mechanical properties in general. The limitation of  $\beta$ -volume fraction up to 14% leads to maintaining Ti6Al4V, a convenient corrosion resistance. The formation of TiO<sub>2</sub> is the main reason for the corrosion resistance, especially pitting corrosion, of titanium alloys. However, according to [LEYE03], the passivation of the surface depends strictly on the integrity of the oxide scale so that the oxide layer is localized undamaged on the very upper surface of the material. Such integrity is shown very exemplarily in the case of Gr.04 at 800°C, while the opposite is obtained for Ti6Al4V. (In figure 4-10, the green spots refer to the  $\beta$ -grains.)



*Figure 4-10: Volume fraction of  $\beta$ -phase of Ti6Al4V depending on the temperature.*

For this reason, titanium ASTM Gr.04 is announced to exhibit the best pitting corrosion resistance among the studied alloys at elevated temperatures. However, a highly thin TiO<sub>2</sub> layer in the case of KS and XT cannot serve as a passivating layer against corrosive environments. Consequently, the oxidation behavior of KS and XT is obviously favorable upon Ti6Al4V as well as Gr.04. A neglectable oxide layer is observed in figure 4-11 in the case of XT and KS, while the oxide layer in the case of Gr.04 is thicker. Ti6Al4V exhibits the thickest oxide layer with variable thickness across the material surface. In addition, another thin Ti<sub>2</sub>O<sub>3</sub> layer is observed (in figure 4-11 in yellow color) with Ti6AL4V. Some intrinsic grains of Ti<sub>2</sub>O<sub>3</sub> were also formed. Another feature observed with the aid of the study of microstructure is the effect of the usage of a protective gas within the hot creep forming. Since a relaxation period follows the hot forming stage, exposure to gas lasts longer manifoldly. Therefore, an application of HCF under a protective environment is expected to support the oxidation behavior of the material. In figure 4-12, a comparison of EBSD micrographs for all regarded materials at 800°C is made with and without the usage of the protective gas. Argon, as an inert gas, was used to ensure a protective ambience. Samples of all studied alloys were laid into a pre-heated batch

furnace at 800°C for 12 min, once with the application of the argon gas and another time without it. Then, they were air-cooled down to room temperature. According to the measurement conducted on the used argon, its purity amounts to approximately 95%.

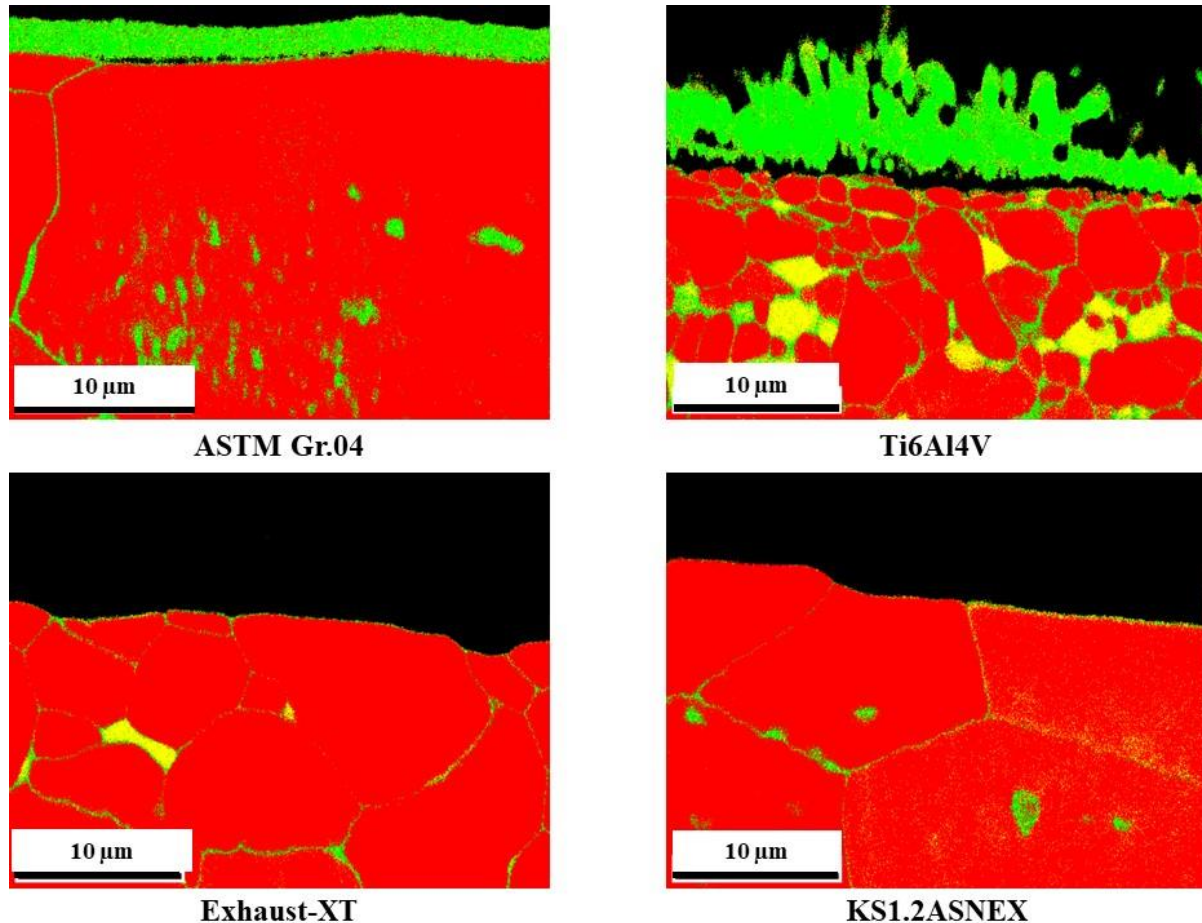
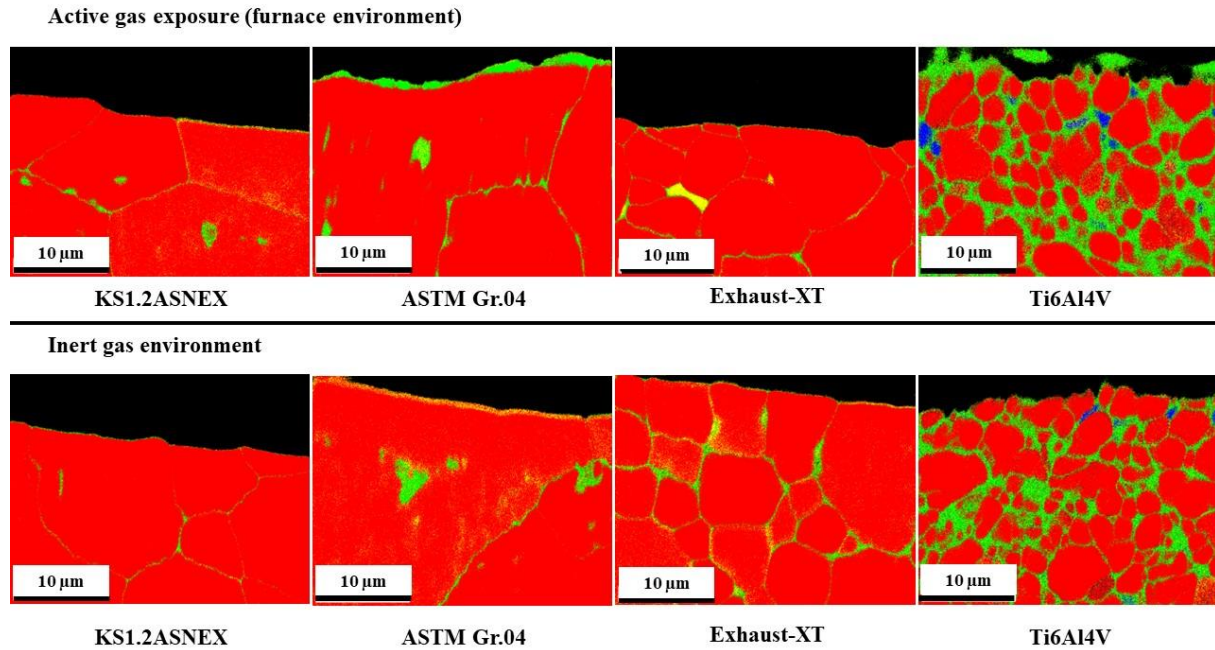


Figure 4-11: Shape of Oxide scale at 800°C for the studied alloys.

As can be seen in figure 4-12, the usage of inert gas impacts the oxidation behavior of Gr.04 as well as Ti6Al4V meaningfully. According to the EBSD mapping displayed in figure 4-12, the heating conditions and Al-content are not appropriate to raise the desired alumina instead of titanium dioxide at the surface of the Ti6Al4V sample. So, the selected oxidation cannot be ensured in this case. However,  $\text{Al}_2\text{O}_3$  is present within some grains as well as on the grain boundaries and serves as a major phase to enhance thermal stability.

KS and XT exhibit a high oxidation resistance at 800°C even without the usage of the protective gas. Such a phenomenon is ascribed apparently by the gradient in oxygen content of  $\alpha$ -alloys and the high aluminum content of Ti6Al4V (see table 3-1). (In figure 4-12, red and blue color refer to  $\alpha$  and  $\beta$ -phases respectively. Green color is for  $\text{TiO}_2$ , and yellow is for  $\text{Ti}_2\text{O}_3$ . The grey spots in Ti6Al4V micrographs indicate the presence of  $\text{Al}_2\text{O}_3$ ).



*Figure 4-12: Effect of usage a protective gas on the formation of superficial Oxide layer at 800°C.*

Analog to the investigation at RT, we can also find out the grain size by determination of the G-index. Table 4-6 shows it in dependence on temperature.

Alloy T[°C]	KS	XT	Gr.04	Ti6Al4V
<b>600</b>	8	10	8.5	11
<b>800</b>	8	9.5	7.5	12

*Table 4-6: G-index at elevated temperatures*

The microstructure of each alloy, whose G-index was observed in table 4-2, has become finer with increasing temperature. XT exhibits the finest microstructure among the studied  $\alpha$ -alloys. However, Ti6Al4V is still the most fine-grained microstructure in all cases. The distribution of  $\beta$ -phase around the grain boundaries of  $\alpha$ -ones is shown in figure 4-13.

Here, the needle-like  $\beta$ -grains propagate around  $\alpha$ -grains with increasing temperature. However, the stability of the G-index with respect to all materials denotes the high thermal stability of titanium alloys in general. In the case of Ti6Al4V, both the oxide layer and  $\alpha$ -case layer are separately recognized out of a light microscope scanning without any need for further investigation.

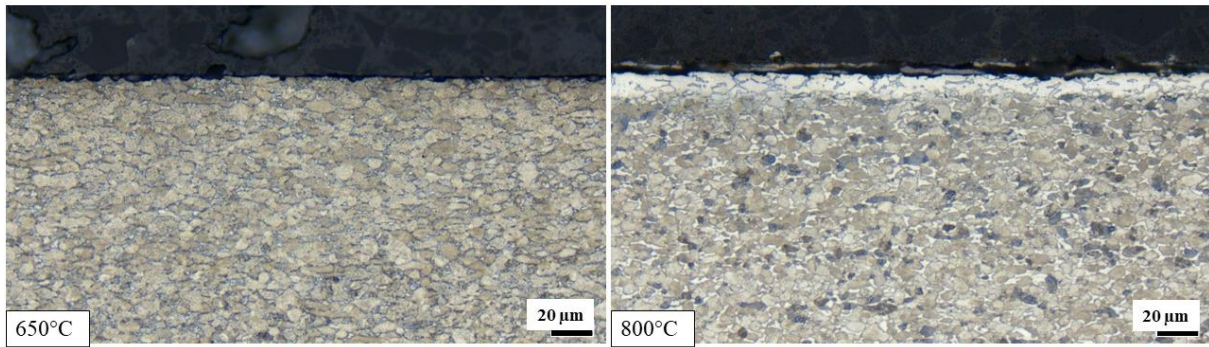


Figure 4-13:  $\alpha$  and  $\beta$  distribution for Ti6Al4V in dependence on forming temperature.

At the end of the microstructural study, a temperature level of 650°C can be stated as convenient to conduct HCF with no need for any subsequent chemical removal. KS and XT have proven the best oxidation resistance in this case.

#### 4.5.2 Texture at temperature level (650°C)

Changing of the texture of  $\alpha$ -alloys represented by KS has been compared to Ti6Al4V in RT and 650°C. The Pole figure of KS at 650°C reveals more inclination of the basal pole as well as the prismatic plane to other angles than RD (A1) and TD (A2).

Therefore, the distinctive anisotropy at RT becomes lower, so the technical texture is slightly lower at 650°C than at RT [LEE20].

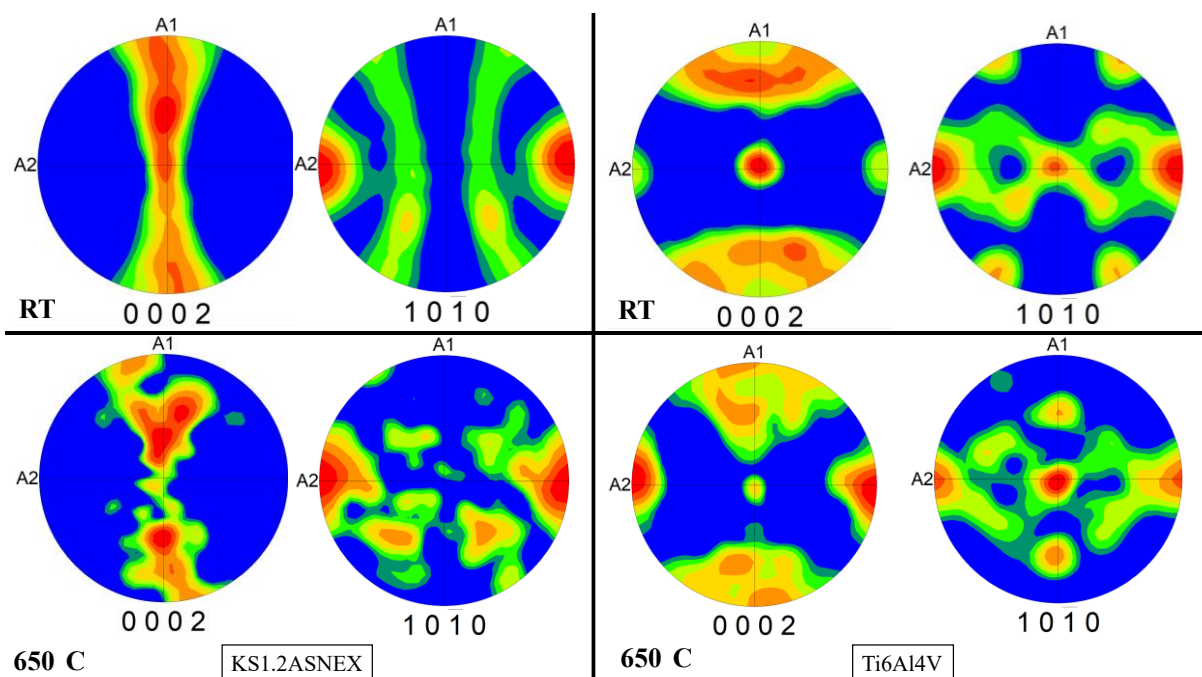


Figure 4-14: Pole figures of KS and Ti6Al4V at RT and 650°C (RD:A1 & TD:A2).

Consequently, the effect of texturing of KS at RT on the presence of earing is expected to be inferior at 650°C. Ti6Al4V exhibits the same tendency at RT as well as at high temperatures. A small difference can be seen in the basal pole so that the basal plane (0002) at RT is mostly inclined to ND, while it is more inclined to TD at 650°C. In addition, the density of grains with a diagonal orientation of the prismatic plane at RT diminished at PF (101̄0) at 650°C, resulting in more homogeneity in grains orientation at this high temperature. However, both basal and prismatic poles imply less texturing at 650°C than at RT, denoting a better drawability in both cases. IPF for both materials in the RD-TD plane with (001) shows a similar tendency at RT to this at 650°C. In figure 4-15, mapping confirms for KS the predominance of the basal plane (0001) parallel to the projection plane with less density at 650°C than RT. In the case of Ti6Al4V, the tendency for prismatic planes (101̄0 for  $\alpha$  phase and 101 for  $\beta$  phase) at RT becomes less at 650°C.

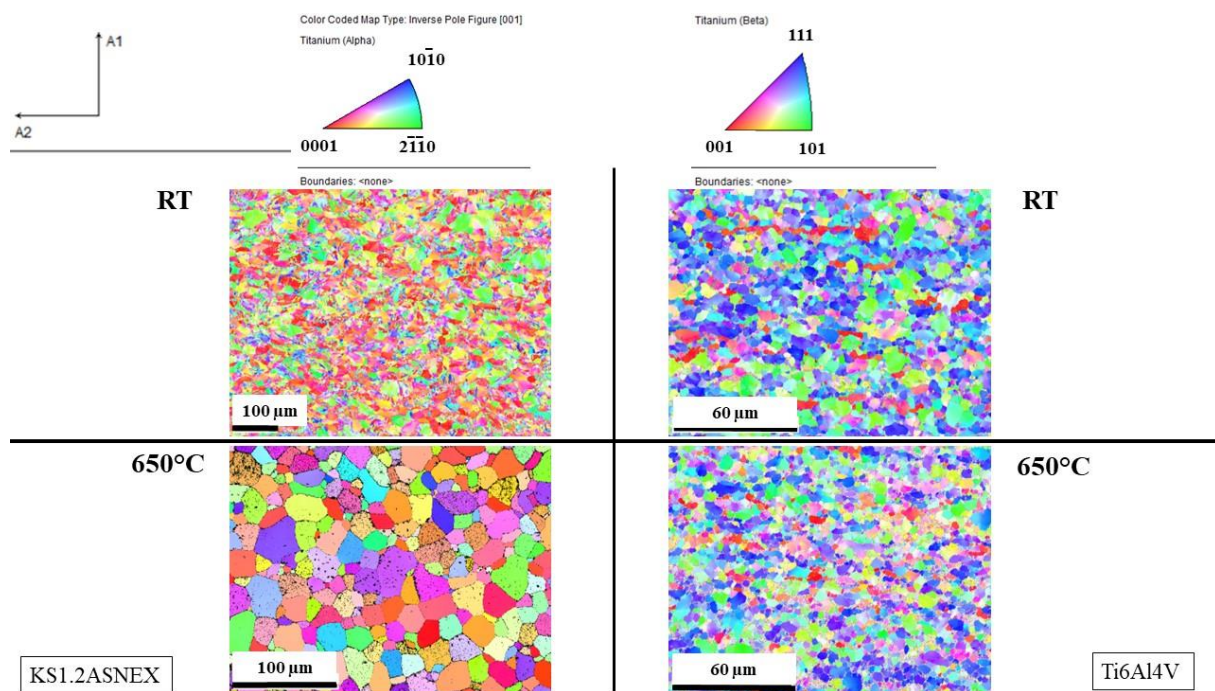


Figure 4-15: Inverse pole figures on plane (RD-TD) for KS and Ti6Al4V at RT and 650°C.

Contrary to Ti6Al4V, EBSD mapping for KS does not reveal the grain refinement at higher temperatures compared to RT because the as-received material has already been cold rolled, and, thus, the grain boundaries at RT are not easily recognized. For this reason, we submitted the grain size with the aid of the G-index investigation according to ISO 643.

### 4.5.3 Hardness at elevated temperatures

Compared to table 4-3, the hardness number at elevated temperatures is nearly similar to the measurement at RT. Such an expected result is due to the absence of any type of heat treatment. The only variation is observed in the hardness of Gr.04. Apparently, heating the material up to the recrystallization temperature results in a small softening of the material surface. This can be ascribed to the thick  $\alpha$ -case layer seen in figure 4-11 compared to other studied alloys. The latter layer is the main cause of any brittleness occurrence.

<b>Hardness number according to Vickers [HV0.5]</b>	
<b>Alloy</b>	<b>Mean Hardness</b>
<b>KS1.2ASNEX</b>	162
<b>Exhaust-XT</b>	200
<b>ASTM Gr.04</b>	228
<b>Ti6Al4V</b>	325

Table 4-7: Hardness number according to Vickers at 800°C for the studied alloys.

### 4.6 Statistical model for HCF on KS

Based on results in section 4.5, KS sounds to possess the best potential for hot forming. However, the parameters of HCF should be adapted to obtain the best stress relief conditions without running a risk of the emergence of  $\alpha$ -case. As explained in section 3.4, a large study was designed on KS, and then the regression analysis results were availed to optimize the parameter set in the case of XT and Gr.04.

Before starting the statistical study, superficial test series of relaxation were conducted on KS to show the bare effect of forming temperature on the formation of  $\alpha$ -case as well as stress relief. For this purpose, a course of temperatures from 550 to 800°C was chosen.

In figure 4-16, results are displayed schematically, which implies a complete stress relief starting from 700°C. In this case, the variation of other parameters is not considered.

However, stress relief of 85% at 600°C is also acceptable, according to the specifications of manufacturing aerospace parts [DAN462].

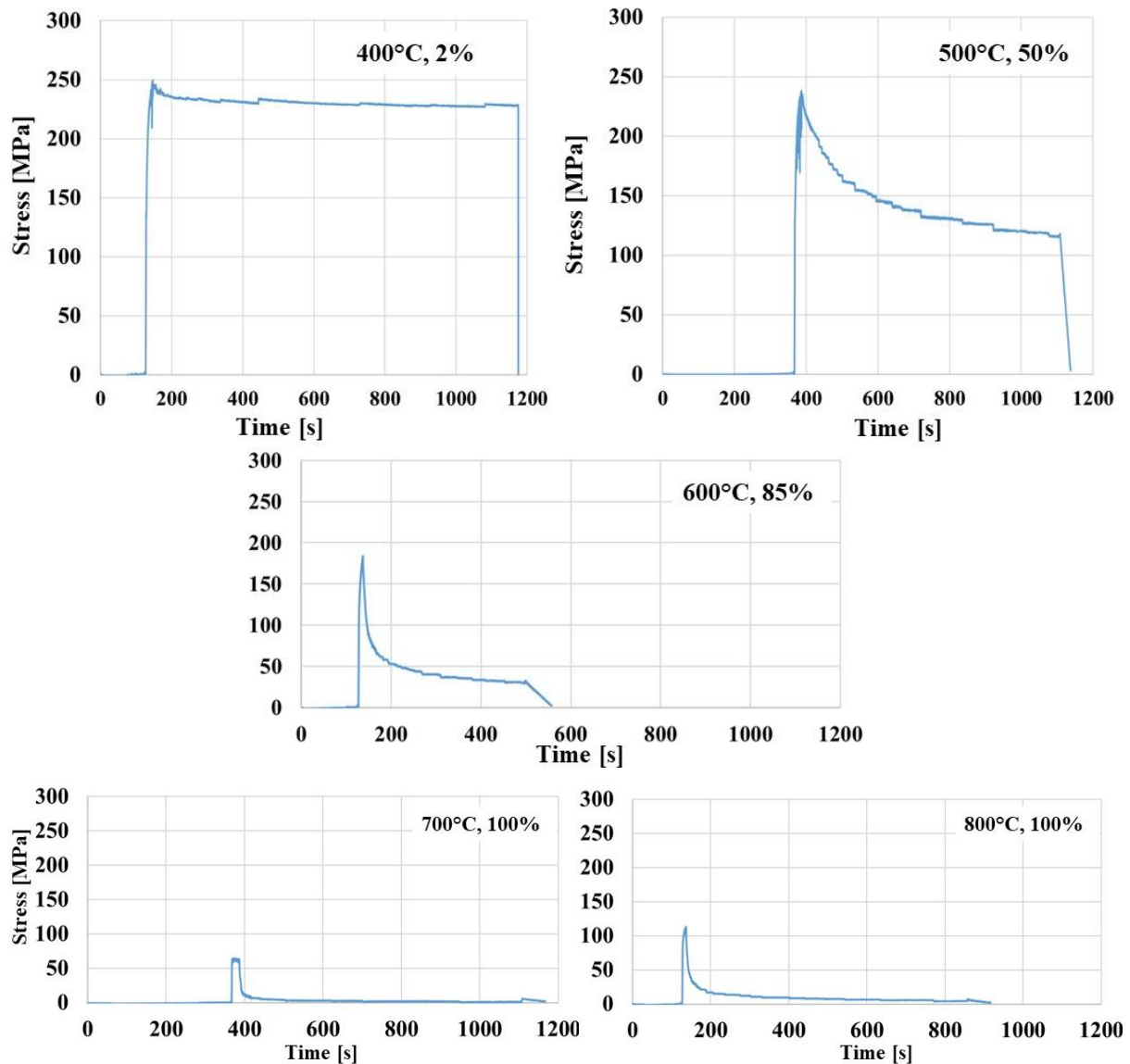


Figure 4-16: Stress relaxation curves for KS in dependence on temperature level.

#### 4.6.1 Screening phase

The screening phase was made based on table 3-5 with regard to results displayed in figure 4-16. With the aid of Cornerstone<sup>®</sup>, a detailed table of experiments has been generated. Such a table includes 28 test runs, as listed in table 4-8. However, the focus within this table is on stress relief, whereas the formation of  $\alpha$ -case is observed in the previous section, and 750°C was consequently announced as the temperature level, starting from which  $\alpha$ -case is formed at the surface. RMS and optimums stages also set a focus on the  $\alpha$ -case layer.

The result of table 4-8 is defined as the residual stress in percent, i.e., the percentage of the residual stress after relaxation from the whole stress arising at the end of the forming stage. The result obtained from figure 4-16 about the proportional increase of stress relief with forming temperature has been enhanced so far.

Parameter Number	Temp. [°C]	Strain rate [s <sup>-1</sup> ]	Heating time [s]	Creep strain [%]	Sample Orientaion	Relaxation time [s]	Result
							Residual stress [%]
1	800	0.075	120	0.2	RD	1800	4
2	750	0.075	360	5	TD	1440	0
3	750	0.09	120	10	RD	1320	0
4	650	0.06	120	5	RD	0	100
5	750	0.06	360	10	TD	1080	0
6	800	0.09	360	5	RD	1800	0
7	700	0.06	120	10	RD	1800	2.2
8	600	0.09	360	0.2	RD	1440	0
9	550	0.06	120	1	RD	1440	29.5
10	700	0.06	360	0.2	TD	0	100
11	550	0.09	360	10	TD	60	49.76
12	550	0.075	360	5	RD	720	24.23
13	750	0.09	360	10	RD	0	100
14	550	0.09	120	0.2	TD	1800	39.39
15	600	0.075	120	10	RD	1080	10.81
16	750	0.09	360	10	TD	60	10
17	650	0.06	360	0.2	TD	1080	0
18	650	0.075	120	10	TD	1440	10.44
19	750	0.06	360	10	RD	60	8.7
20	700	0.075	360	1	RD	360	7.62
21	800	0.06	360	10	TD	720	0
22	550	0.06	360	10	RD	60	48.37
23	800	0.075	120	1	TD	0	100
24	650	0.09	360	1	RD	360	17.43
25	600	0.075	360	1	TD	1800	16.31
26	750	0.075	120	0.2	TD	360	7.46
27	600	0.06	120	5	TD	360	16.02
28	700	0.09	120	5	TD	1080	3.19

*Table 4-8: Stress relief recorded after the screening phase for KS.*

Experimental results confirm a correlation between temperature and stress relief. However, the effect of other parameters should also be taken into consideration.

Therefore, a statistical analysis has been conducted. In order to obtain a regression analysis without any external impact, it was assumed that the relation among all the parameters is linear, i.e., there is no statistical weighting of any parameter (even forming temperature) upon the

others. Since the trial of the test consists of less than 50 samples, Cornerstone manual suggests a significant level  $\alpha=0.1$  as a rule of thumb. In this context, each parameter whose  $\alpha > 0.1$  is supposed as statistically insignificant. Table 4-9 shows the summary of the term ‘significance’ throughout the screening stage. Based on the statement above about significance level and according to table 4-8, the following statement can be released:

The term significance of relaxation time has assumed the value of 0, which means that it has the highest statistically significant over other parameters. Test number 14 in table 4-8 was conducted with a forming temperature of 550°C and other plotted parameters. Owing to the long-term relaxation of the 1800s, it was possible to achieve 60% stress relief. However, all the tests conducted with high relaxation time have resulted in meaningful stress relief.

Figure 4-17 plotted relaxation time over stress relief, and it shows the points distribution over the relaxation time.

Forming temperature can also be announced as a significant term owing to its significance value of 0.013. Heating time has also exhibited a statistical significance, whereas its significance value was below 0.1. Creep strain, strain rate, and sample orientation have not impacted stress relief significantly. For this reason, although they have not been completely excluded within the next stage of the HCF design of the study, they were varied without any weighting.

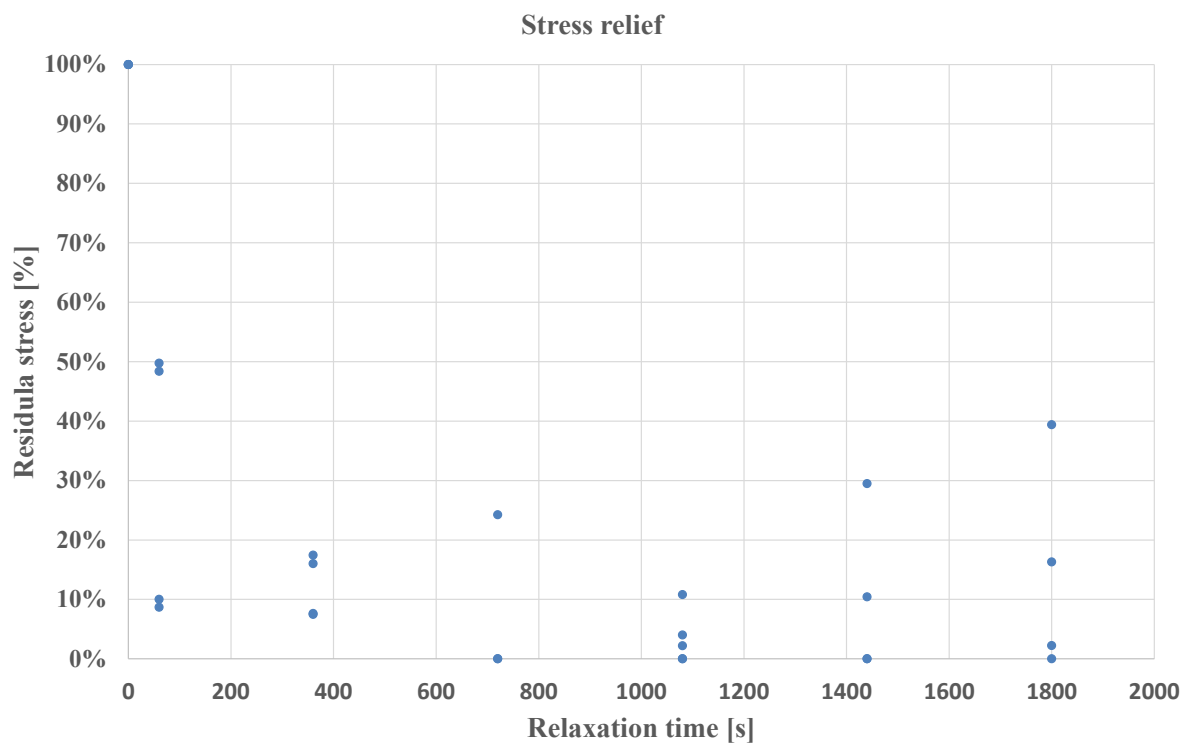


Figure 4-17: Scatter plot for residual stress depending on relaxation time in screening stage.

Term	Stress relief
Constant	0.000
Forming temperature	0.013
Strain rate	0.870
Heating time	0.073
Creep strain	0.324
Relaxation time	0.000
Sample orientation	0.584

Table 4-9: Term significance out of regression analysis after screening stage for KS,  $\alpha=0.1$ .

#### 4.6.2 Refinement stage

The upcoming part of the study focused on the significant terms according to the previous stage. For this purpose, a new design was implemented instead of the linear one, namely the D-optimal design spoken in section 3.4.2. By means of Cornerstone, the study was designed to focus on relaxation time, heating time, and heating level. The strain rate was chosen for the whole stage of  $25 \cdot 10^{-4} \text{ s}^{-1}$ , and all the samples have the same orientation. D-optimal design with a quadratic and interactive model has been established, in which the interaction among relaxation time, heating time, and forming temperature has been set up, and the squaring of the aforementioned terms has also been done. Table 4-10 below summarizes the whole stage with its results, which were utilized to perform the regression analysis for the refinement stage.

Complete stress relief could have been achieved at  $800^\circ\text{C}$  even with a relaxation time of 360s. However, results reveal a stress relief of 85% in the best case and 70% in the worst one. Stress relief of 95% can be achieved at  $700^\circ\text{C}$  according to table 4-10 in the best case. On the other hand, such a temperature does not exhibit any tendency to emerge an  $\alpha$ -case layer at the surface, even when relaxation time is quite high. Starting from  $750^\circ\text{C}$ , a thin  $\alpha$ -case layer can be observed, whose width has been increased ca. fivefold at  $800^\circ\text{C}$  despite less relaxation time in comparison. The correlation among the statistically significant parameters and their weighting results in a variation of the significance of each term compared to the previous results from table 4-9. As seen in table 4-11, relaxation time, forming temperature, and their products have the major influence on stress relief. A remarkable term to regard is also creep strain and its products. The latter parameter does not show any impact on the emergence of the  $\alpha$ -case layer.

Parameter Number	Temp. [°C]	Heating time [s]	Creep strain [%]	Relaxation time [s]	Results	
					Residual stress [%]	$\alpha$ -case layer [ $\mu\text{m}$ ]
41	600	360	0.5	360	30.1	0
42	800	360	1	1080	4.84	4.9
43	600	120	1	360	22.54	0
44	600	360	10	360	14.88	0
45	600	120	10	720	17	0
46	800	120	0.5	1080	1.67	4.5
47	800	360	0.5	1080	0	7.5
48	700	360	1	720	8.93	3
49	600	120	0.5	1080	21.6	0
50	600	120	0.5	360	28.7	0
51	700	240	0.5	360	13.45	0
52	600	240	10	360	14.7	0
53	700	360	10	1080	3.9	0.5
54	700	120	10	1080	4.1	0.1
55	800	240	10	1080	4.35	5.3
56	800	240	1	360	8.72	2.4
57	800	120	1	1080	0	9
58	600	240	1	720	14.9	0
59	800	360	10	720	2.6	5.3
60	800	120	10	1080	1.32	6.1
61	800	360	1	360	1.57	7.2
62	600	360	0.5	720	18.7	0
63	800	120	0.5	360	7.44	3
64	600	360	1	360	20.76	0
65	800	120	0.5	720	3.2	1.5
66	600	120	1	1080	18.6	0
67	800	360	10	360	6.9	3.5
68	600	120	10	360	15.01	0
69	600	120	10	1080	8.93	0
70	800	360	0.5	360	4.95	2.9
71	800	120	1	360	3.22	2.5
72	600	360	1	1080	14.28	0
73	800	360	1	360	0	2.9
74	800	120	10	360	5.52	2.7
75	700	120	1	720	4.9	1.5
76	600	360	0.5	1080	19.5	0
77	600	360	10	1080	7.9	0
78	600	120	1	1080	13.7	0
79	700	240	0.5	1080	4.7	2
80	800	120	10	360	2.92	2.9

Table 4-10: Results recorded after refinement stage for KS.

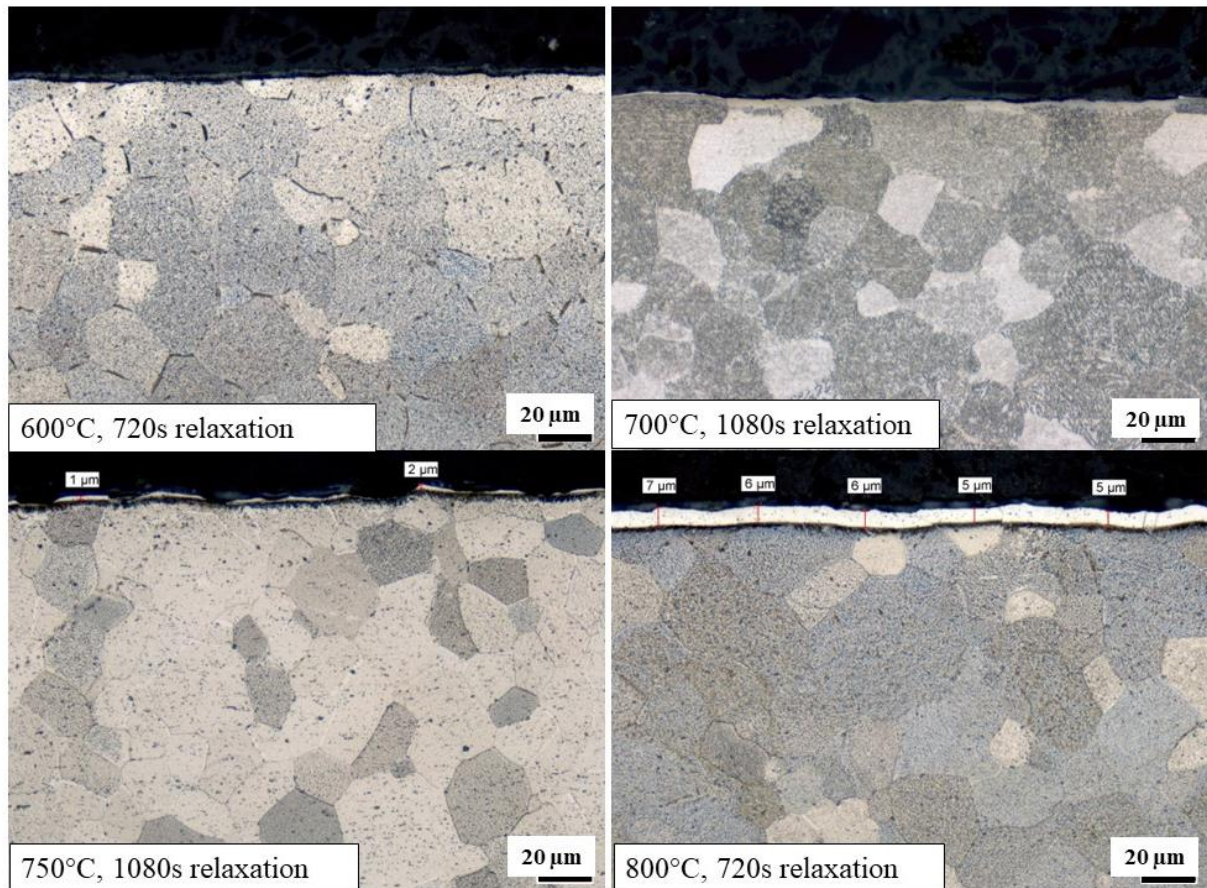


Figure 4-18: Presence of  $\alpha$ -case layer according to variation of HCF conditions for KS.

Indeed, forming temperature seems to have the highest effect on both results. Such a statement was also confirmed by reading the results from table 4-10. Apparently, the weighting of the parameters does not make a meaningful change in results except for forming temperature, whose weighting has impacted both stress relief and the presence of  $\alpha$ -case. However, the interaction between creep strain and relaxation time can have a large significance in terms of stress relief. As a result of the regression analysis, stress relief can be modeled according to the following equation:

$$SR[\%] = -171.7 + 0.6 \cdot T + 0.03 \cdot t_r - 3.1 \cdot 10^{-5} \cdot T \cdot t_r - 3 \cdot 10^{-4} \cdot T^2 - \phi \quad (4.1)$$

T: Forming temperature [°C].

$t_r$ : Relaxation time [s].

$\phi$ : Error factor.

Error factor in equ. 4.1 assumes a value between 10 and 28 in proportional dependence on forming temperature. Such a small value of  $\phi$  indicates a consistent fitting of stress relief.

Number	Term	Stress relief	$\alpha$ -case
0	Constant	0.007	0.015
1	Forming temperature	0.000	0.011
2	Heating time	0.405	0.146
3	Relaxation time	0.002	0.006
4	Creep strain	0.000	0.148
5	Heating*Forming	0.506	0.108
6	Relaxation*Forming	0.017	0.001
7	Creep strain*Forming	0.000	0.107
8	Heating*Relaxation	0.526	0.390
9	Creep Strain*Relaxation	0.091	0.152
10	Forming <sup>2</sup>	0.003	0.008
11	Heating <sup>2</sup>	0.418	0.148
12	Relaxation <sup>2</sup>	0.425	0.946

Table 4-11: Term significance out of regression analysis after refinement stage for KS.

The regression analysis also enables another statistical graph with a depiction of the influence of each term of both outputs respectively. This graph is called the Pareto effect. This way of statistical analysis depends on the percentage effect of each parameter on the output. As a rule of thumb, the significant parameters are those whose accumulative effect amounts to 80%. Figure 4-19 depicts the effect of the most significant parameters on stress relief and the thickness of an  $\alpha$ -case layer.

Parallel to the regression analysis, the Pareto graph implies the most effect of forming temperature and relaxation time on both stress relief and the emergence of  $\alpha$ -case layer. Forming temperature should impact the result most. Again, creep strain sounds to have a significant influence on the results, which does not belong to the input terms in practice, but rather to the results. However, creep strain has not appeared in equ. 4.1 as a term, i.e., it is not mathematically suggested as a decisive term. A remarkable point out of the statistical analysis in this refinement stage is the absence of the effect of heating time on the results, as seen in table 4-11 and figure 4-19. Its effect might become lower after weighting the parameters mentioned above.

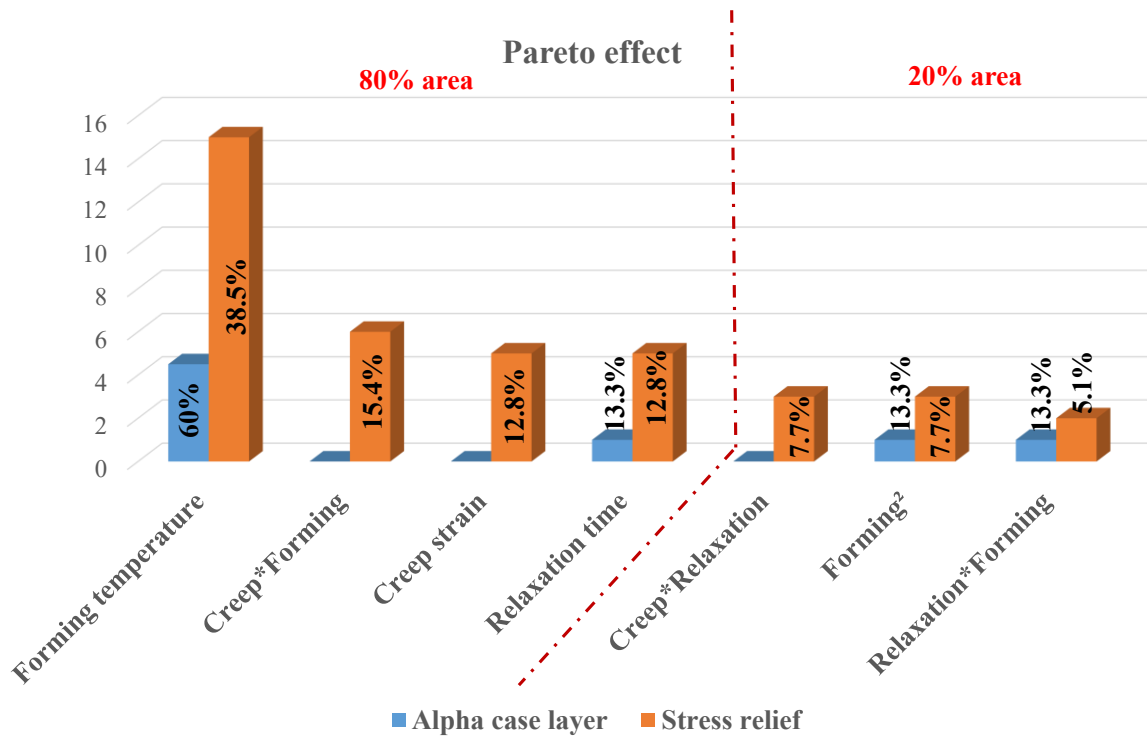


Figure 4-19: Pareto effect of parameters on the results of refinement stage for KS.

#### 4.6.3 Optimum stage

After conducting both statistical stages, the main parameter of HCF is adapted in order to obtain a well-deep formed blank with a minimum hazard of springback effect and, if possible, no presence of the detrimental  $\alpha$ -case layer. While tensile tests have revealed the best conditions of hot deep drawing, the results of both previous stages have confirmed that adaptation of forming temperature and relaxation time should ensure the sought outputs. At the end of the refinement stage, a so-called predicted response graph defined the best run based on the results of the regression analysis. Such parameter values are listed in table 4-12 below.

Term	T [°C]	$t_r$ [s]	Results	
			Residual stress [%]	$\alpha$ -case layer thickness [ $\mu\text{m}$ ]
<b>Predicted Value</b>	700	710	$7.8 \pm 5$	$0.6 \pm 1.8$

Table 4-12: Predicted values of the significant parameters after refinement stage for KS.

Based on this predicted value, an optimum stage has been conducted, which consisted of 8 test runs. The spectrum of forming temperature was widened to cover a range between 670 and 750°C in four steps for each two test runs. Other parameters were kept constant, as shown in

table 4-13 below. Indeed, stress relief of 93% can be ensured in all the cases, and a maximum thickness of the  $\alpha$ -case layer of 2.5  $\mu\text{m}$  was not exceeded.

Figure 4-20 illustrates the formation of the  $\alpha$ -case layer and depicts the measurement of its thickness according to each test run. It is also noteworthy to see the enrichment of the  $\alpha$ -grains adjacent to the surface with oxygen, which is typical for titanium alloys with very high oxidation affinity [LEYE03].

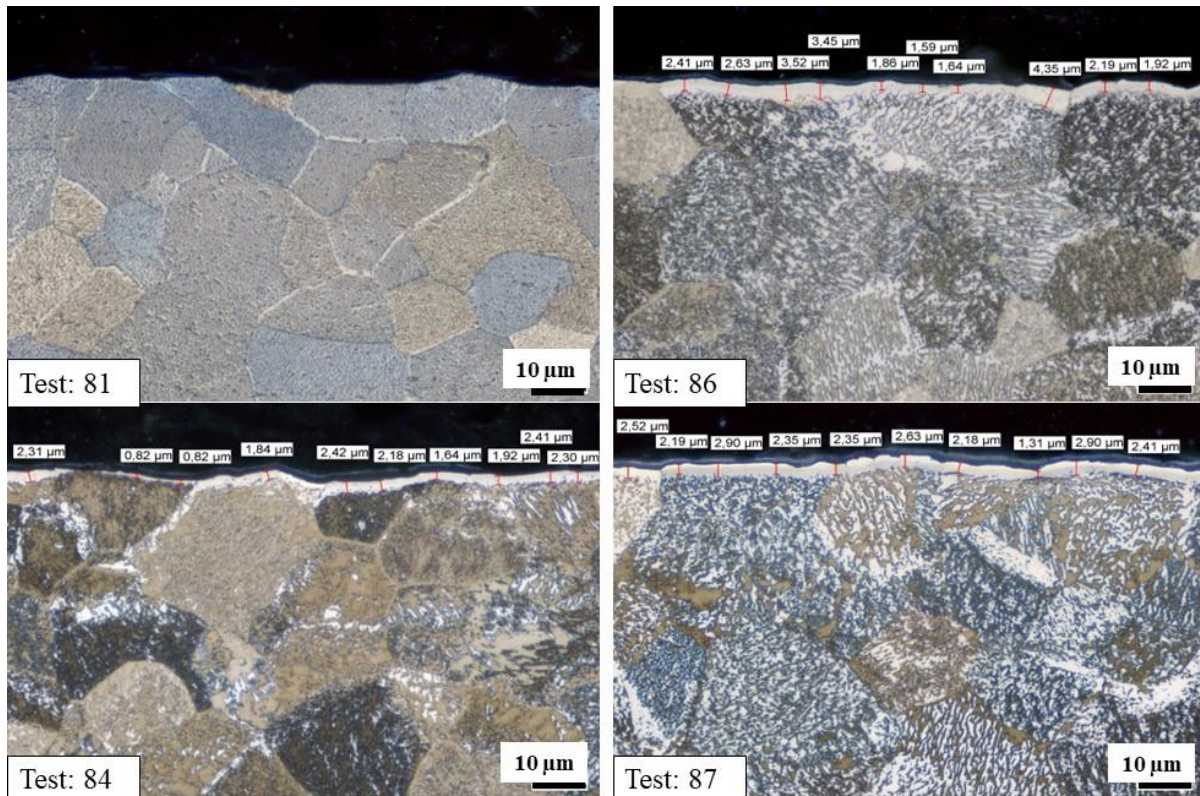


Figure 4-20: Phenomenon of  $\alpha$ -case within the optimum stage for KS.

A comparison between micrographs of a specimen without  $\alpha$ -case exposure (test 81) and micrographs of specimens with such a phenomenon shows the effect of oxygen solution on  $\alpha$ -grains readily. However, results have not shown any tendency in terms of either output.

The statistical study for HCF on KS confirms the results of section 4.2.1 about the possibility of having a free microstructure of  $\alpha$ -case emergence up to 650°C with an ensured stress relief of 85%, industrially quite acceptable for hot deep drawing and convenient for aerospace specifications [DAN462].

Number	Forming temperature [°C]	Heating time [s]	Creep strain [%]	Strain rate [s <sup>-1</sup> ]	Relaxation time [s]	Results	
						Residual stress [%]	$\alpha$ -case layer [ $\mu\text{m}$ ]
81	670	235	5	$25 \cdot 10^{-4}$	710	7	0
82						8	1.13
83	700					6.9	1.05
84						6.3	1.86
85	730					5.4	1.6
86						6.84	2.55
87	750					5.86	2.4
88						5.7	1.2

Table 4-13: Results after test series of optimum stage for KS.

#### 4.6.4 Statistical study on Gr.04

Statistical study on the other two titanium  $\alpha$ -alloys was made with benefit from the results of the extensive study made on KS. Based on the previous study on KS, which was conducted with ca. 88 test runs, a similar study has been made on XT and Gr.04 with 27 test runs, respectively.

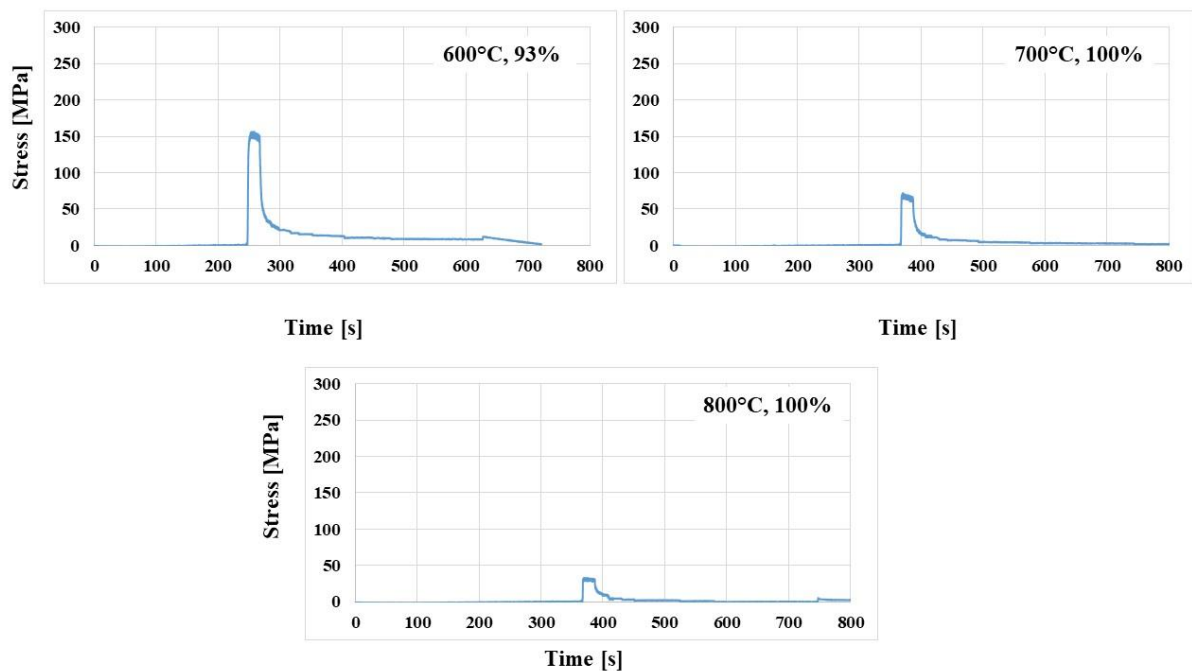


Figure 4-21: Stress relaxation curves for Gr.04 in dependence on temperature level.

In figure 4-21, the behavior of Gr.04 is displayed with respect to stress relief. In this case, stress relief of 93% can be achieved. However, the initial stress value with Gr.04 and KS at 600°C is approximately identical. According to the corresponding graph in figure 4-21, relaxation time is essential in determining residual stress. Here, stress relief is achieved within 200s, while for KS, a relaxation time of 400s was required to achieve 85% stress relief at 600°C (as depicted in figure 4-16). Needless to say, the full relaxation is at 700 and 800°C.

On the other hand, micrographs reveal an oxide position on the very top edge of samples stretched at 600 and 700°C. SEM investigation confirms the presence of  $Ti_xO_x$  as shown in figure 4-22 for positions (a) and (b) from micrographs at 600 and 700°C, respectively.

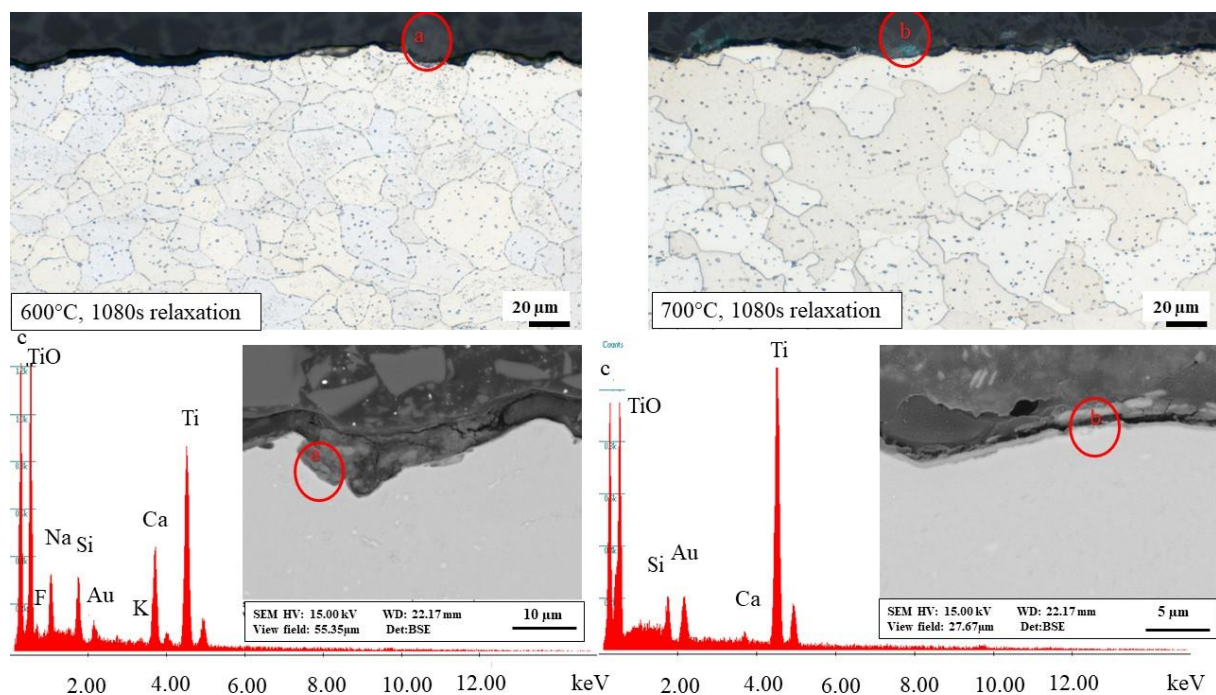


Figure 4-22: Appearance of  $\alpha$ -case positions for Gr.04 at 600 and 700°C.

Compared to KS, Gr.04 at 600 and 700°C possesses less oxidation resistance. In figure 4-23, a representative sample exhibits uniform oxidation with a constant layer at the surface. Indeed, the difference between  $TiO_2$  and  $\alpha$ -case layer is recognized as to colors. Such an effect can also be observed in figure 4-20 for KS. SEM investigation and EBSD mapping have quantified the thickness of the  $TiO_2$  layer.

This green layer distinguishes Gr.04 from all other alloys with respect to the pitting corrosion resistance. However, it might harm the material's mechanical properties and should be removed frequently after each manufacturing stage.

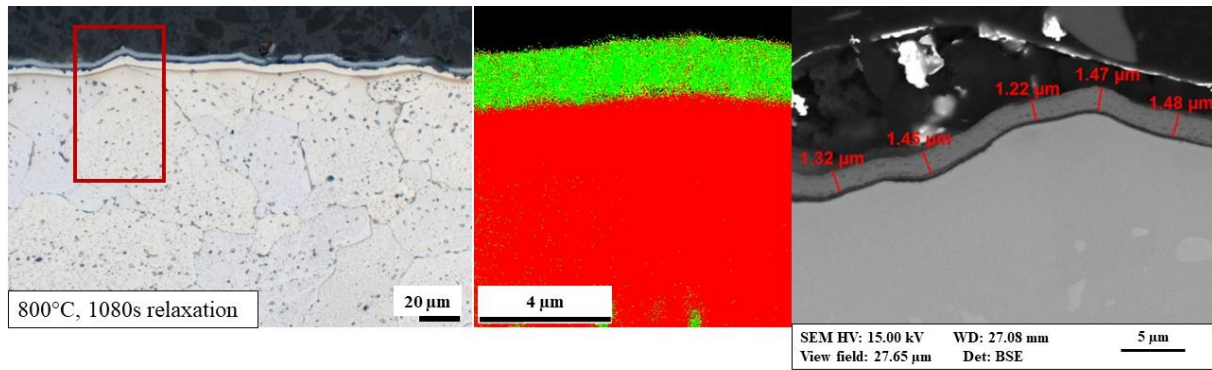


Figure 4-23: Oxide scale and  $\alpha$ -case layer for Gr.04 at 800°C.

#### 4.6.5 Statistical study on XT

Analogous to relaxation curves for KS and Gr.04, stress relief of 88% at 600°C has been achieved in the case of XT. Starting from 700°C, the residual stresses are not observed anymore. A similarity between KS, Gr.04, and XT with respect to the required force to perform the forming stage proportional to temperature level can be stated according to figure 4-24.

Another investigated parameter is the relaxation time needed to reach the abovementioned stress relief.

In the case of KS, it took approximately 400s to reach the goal, while in XT, ca. 300s. However, the difference between both materials and Gr.04 regarding the required relaxation time is a positive aspect of Gr.04. Micrographs of XT at the respective temperature show the lack of an  $\alpha$ -case layer as well oxide layer up to 700°C.

The micrograph obtained at 730°C has revealed the presence of an  $\alpha$ -case layer. However,  $\text{TiO}_2$  is recognized here on a very low scale.

The microsection obtained at 800°C has shown both layers with very acceptable integrity.

A microstructural comparison between KS and XT, according to figures 4-18 and 4-25, confirms a higher oxidation resistance for KS upon XT. The presence of a small amount of Al in KS plays an essential role in this result, which causes a better oxidation resistance, as explained in section 2.2.4. However, Gr.04 and XT deliver an integrated oxide layer to the substrate, contrary to KS, improving their pitting corrosion resistance due to passivating oxide.

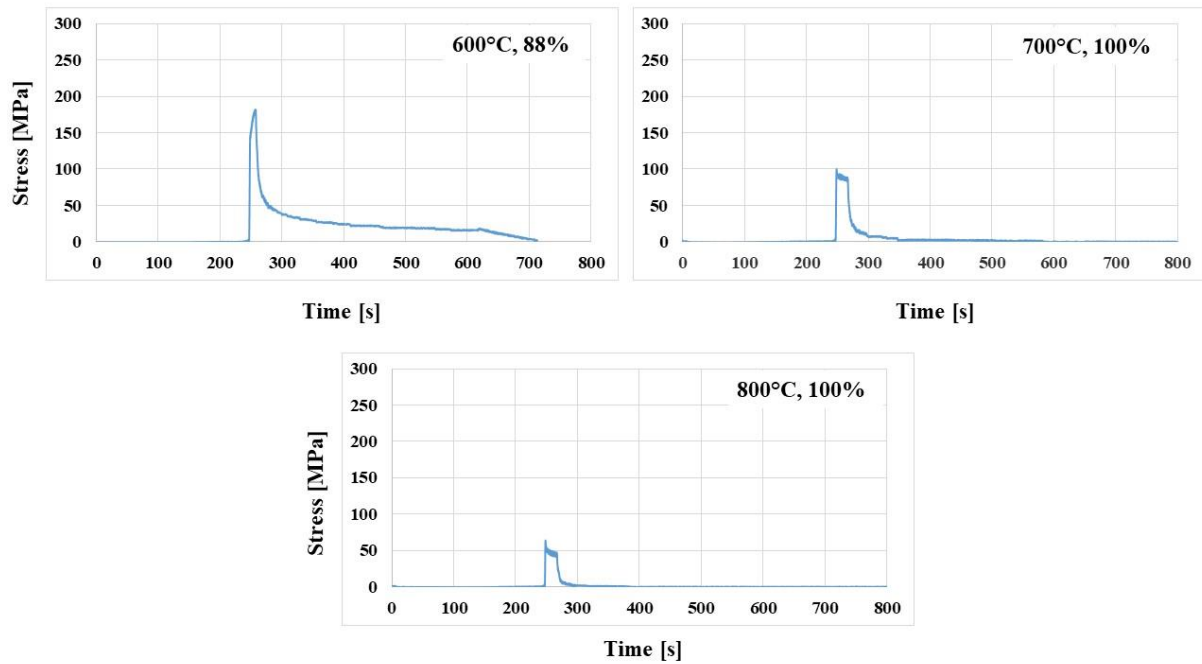


Figure 4-24: Stress relaxation curves for XT in dependence on temperature level.

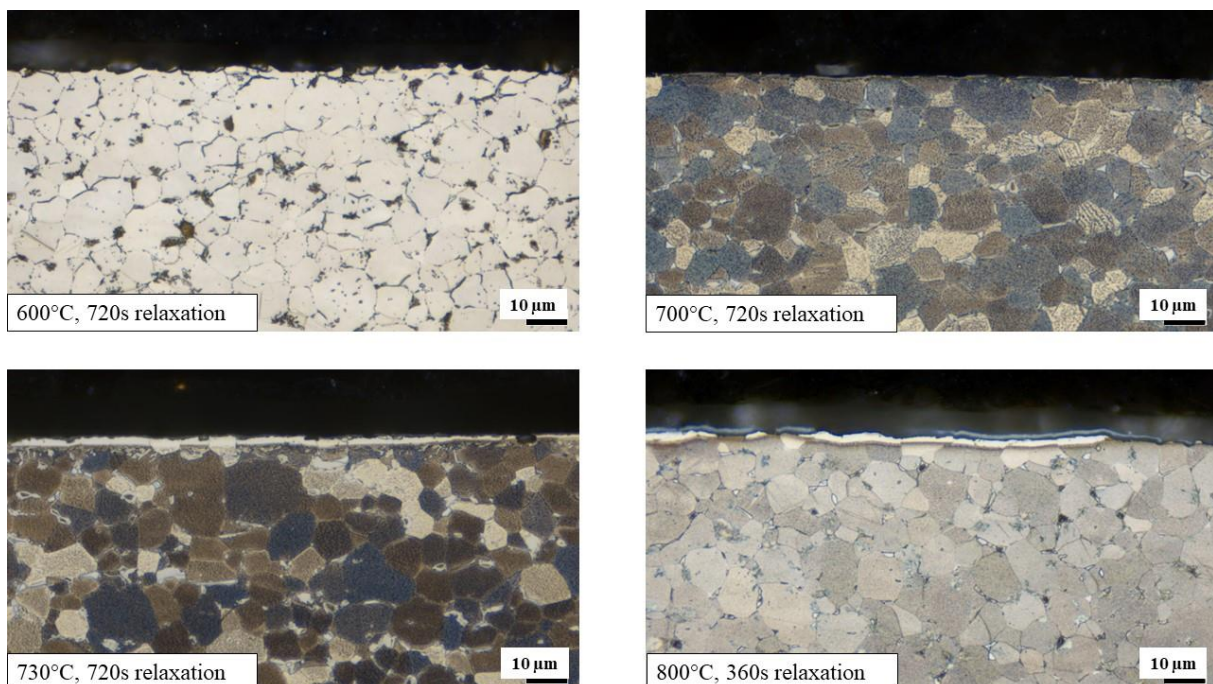


Figure 4-25: Microstructure of superficial  $\alpha$ -case for XT at different temperature levels.

#### 4.6.6 HCF of Ti6AL4V

Ti6AL4V represents another stage of required forming force compared with studied titanium  $\alpha$ -alloys. A triple value is still required at 500°C, while it decreases to double starting from 650°C. Analogous to  $\alpha$ -alloys, full stress relief can be apparently achieved starting from 650°C.

However, relaxation time at this temperature exhibits a higher value than KS, so it amounts in the case of Ti6Al4V at least 600s. Figure 4-26 regards the issue of Ti6AL4V stress relaxation curves. For this reason and others, titanium  $\alpha$ -alloys can be announced to have better HCF potential than  $\alpha$ - $\beta$  alloys. Besides stress relaxation, the presence of the  $\alpha$ -case layer at 800°C has more readiness than  $\alpha$ -alloys at the same temperature level. As seen in figure 4-27, the thickness of the affected layer is wider than the similar cases for titanium  $\alpha$ -alloys. Moreover, the TiO<sub>2</sub> layer does not show any integrity to the base metal, resulting in bad corrosion resistance due to passivating layer. However, a thin  $\alpha$ -case layer exists at 650°C, which is not seen in the case of XT and KS at all. The overall microstructural study of HCF on all the studied alloys indicates the preference of XT and KS upon Gr.04 and Ti6AL4V with respect to the oxidation behavior.

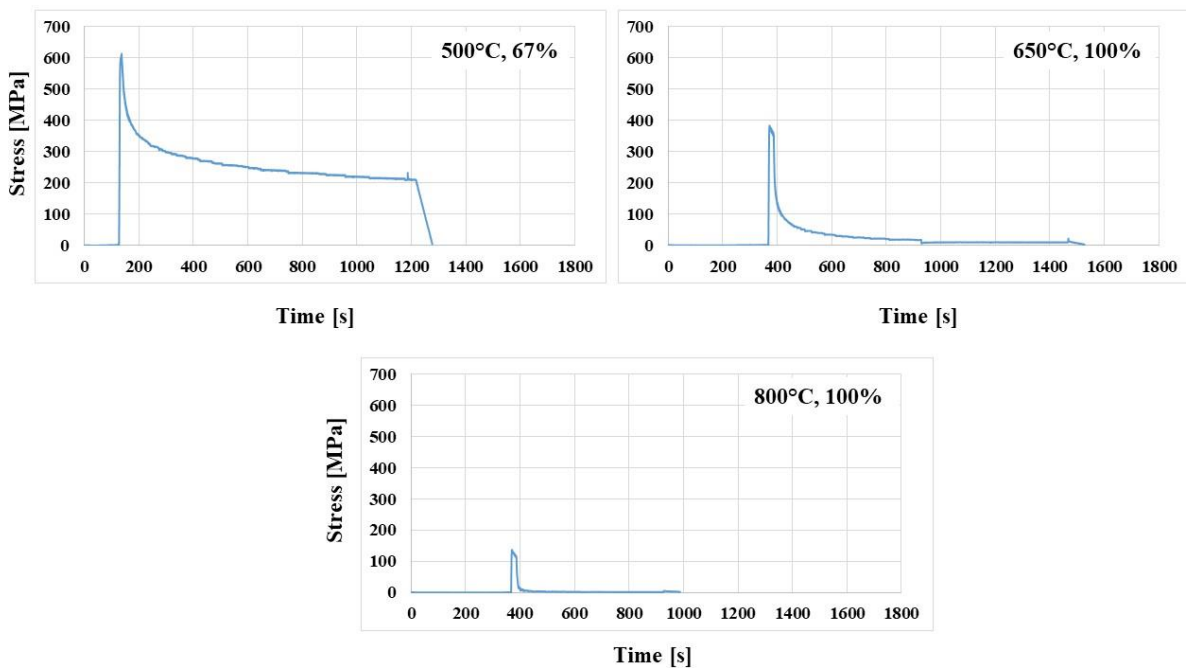


Figure 4-26: Relaxation curves for Ti6AL4V in dependence on temperature level.

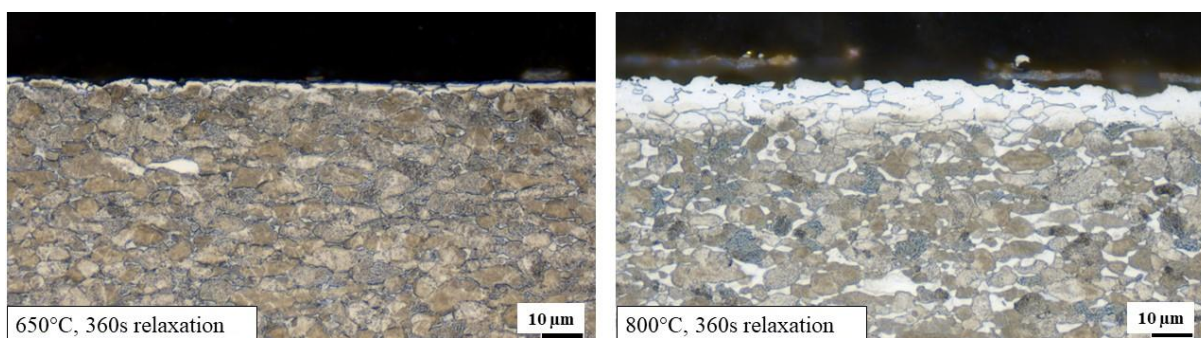


Figure 4-27: Micrographs of Ti6AL4V with oxide observation at 800°C.

## 4.7 Results of numerical study of HDD

### 4.7.1 Setting up the material model

Results obtained from the tensile test at RT, as well as elevated temperatures, were available to define a material model for the regarded titanium alloys, respectively. Those were used to fill out the fields shown in figure 3-10 to define tensile and yield strength for each material.

Since Simufact.forming deals with the actual stresses to define the model,  $K_f$  and  $\varphi$  were calculated according to equ. 3.3 and 3.4. Then the flow curve was fitted based on equ. 3.7 and 3.8 and admitted to model into Simufact.forming interface.

Such a fitting is shown in figure 4-28 for KS at 650°C in an exemplary way. A similar setup was made for KS at other temperature levels as well as for both Gr.04 and XT at the scheduled temperature levels, as illustrated in section 3.5.1 (see the appendix for more details).

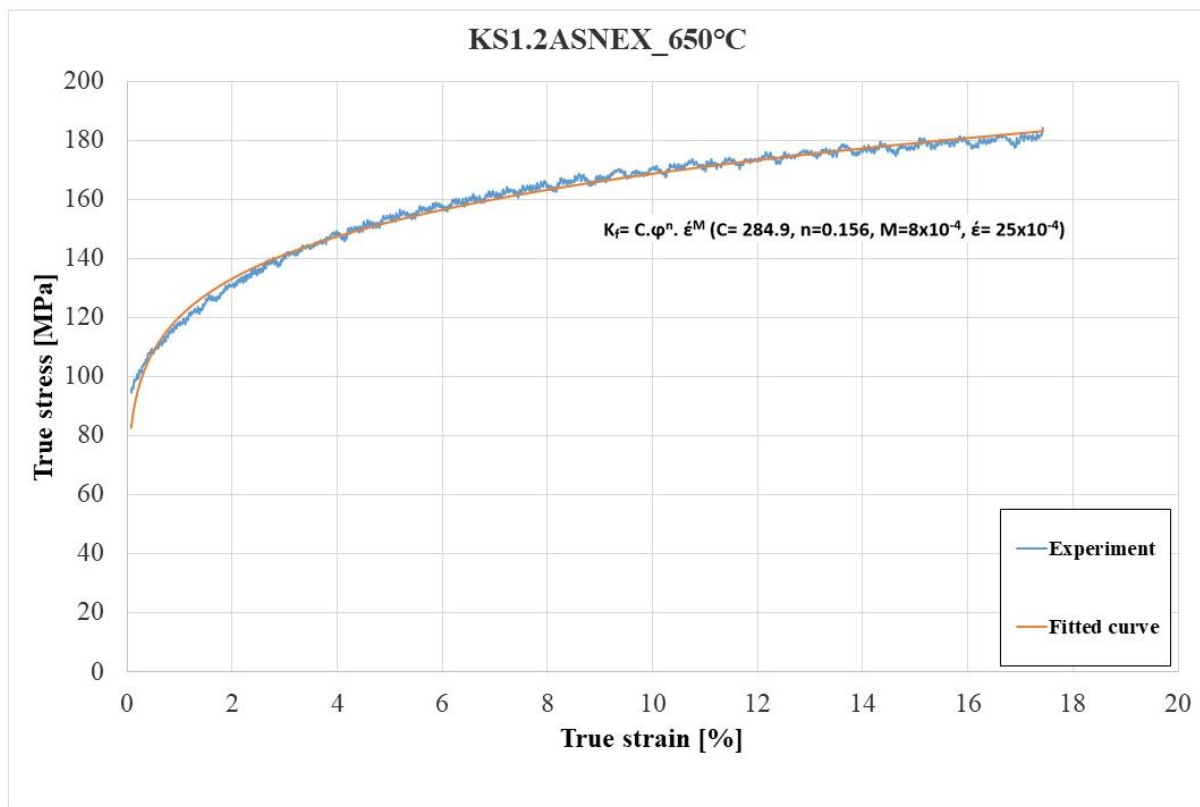


Figure 4-28: Flow curve fitted according to Hensel-Spittel-Ansatz for KS at 650°C with  $c=284.9$ ,  $n=0.156$  and  $m=8 \cdot 10^{-4}$ .

The depiction of the KS-flow curve at this point would be sufficient since it has been proposed to be the focus alloy in this study. R-values obtained from tensile tests were also entered into the proper fields to define the anisotropic behavior of the material, according to Hill and Barlat. Such a definition was barely important to be regarded in the definition of the material since

anisotropy is a crucial characteristic to be considered when defining the material model of each  $\alpha$ -alloy. As seen in figure 4-28, it has been proven that Hensel-Spittel Ansatz is suitable for describing the correlation between true stress and true strain at elevated temperatures. It also shows the ability of KS at the addressed temperature level to achieve a convenient strain needed to reach the deformation stage in the FE model. The extrapolation of the strain value beyond the observed within the study could help to implement further stress ranges, which we haven't reached in our prototyping.

#### 4.7.2 Validation of the simulation model

The swift component has already been produced by the company Formtech with many manufacturing parameters, which are listed in table 3-7.

The thickness of the swift wall was measured in eight positions and delivered to enable the comparison with the thickness obtained from the numerical hot deep drawing of the swift component. The results of such a comparison are displayed in figure 4-29 with a representative model number 3 from table 3-7, forming a swift component of XT. The diagram on the left-hand side depicts the first measured series, while the diagram beside illustrates the comparison of the second measured series.

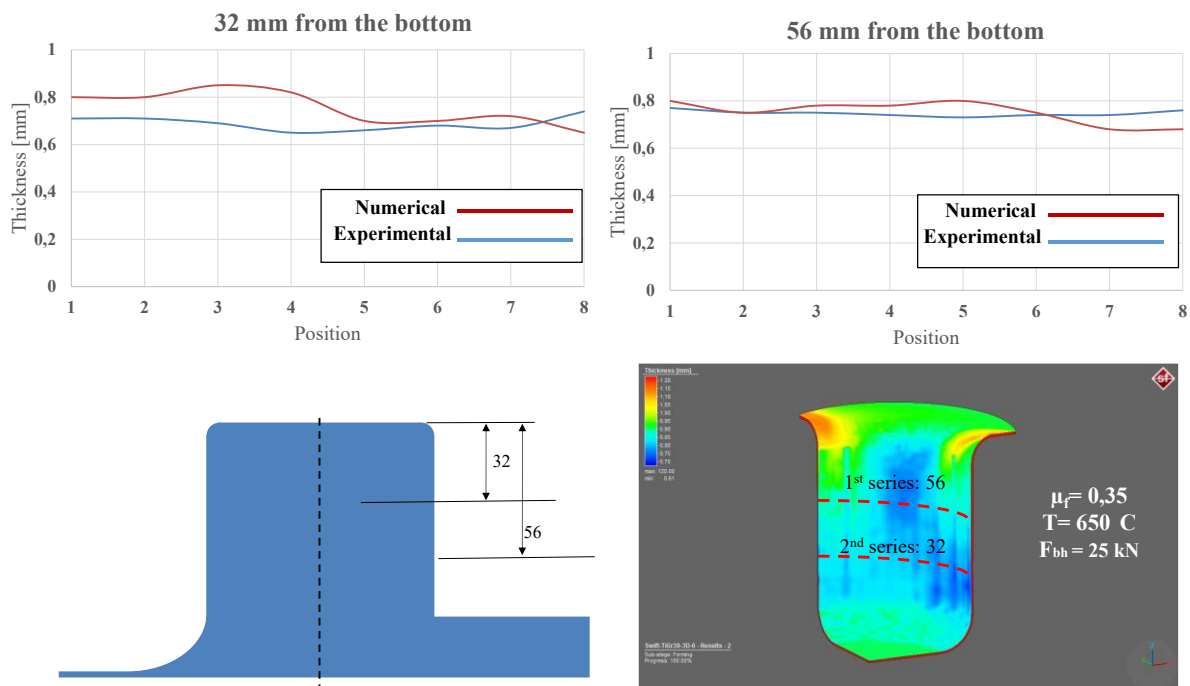


Figure 4-29: Thickness comparison between numerical and experimental forming of Swift.

While the first series denotes great consistency, the deviation of the thickness in the second series cannot be neglected. The thickness resulting from the numerical study is higher than the experimental one in general. However, it is expected to obtain a gradient of numerical accuracy as the measured position is far from the flange. Since the convergence of displacement is incremental, the simulation results in a bigger deviation the deeper the drawing is. The high deviation of thickness amount is less than 10% of the entire thickness, implying a consistency of the FE model according to the tolerance of aerospace production.

#### 4.7.3 Optimization of the numerical frame conditions of HDD

The first task of this section is to optimize the frame conditions to obtain convenient as well as acceptable FE results, from which a real HDD is conducted to manufacture an exhaust component for aerospace applications. As mentioned before, with the aid of company Formtech, a half shell of the t-duct has been submitted to be hot-deep drawn according to simulation results.

Some marginal features are chosen for this optimization. The coefficient of friction, according to Coulomb, blank holding force, the temperature of the die, and the outer contour of the blank have been varied in this context. Figure 4-30 plotted three types of blank outlines for this approach. The diameter of the disc amounts to 600 mm. The trapezium has dimensions of [655x560 mm], while the 3rd contour is suggested by Mr. Beck from Formtech as a similar contour to the formed half-shell. The width of the blank is specified to be 0.9 mm in all cases. Other varied parameters are listed in table 4-14 below. The forming temperature has been varied between 650 and 730°C only to see the effect of it in association with other conditions. However, the forming temperature has already been determined at 650°C to cause the best drawability. Although the variation of materials has comprised all the studied titanium alloys, the main focus was on KS as a nominated material to fulfill the most specifications of HCF at 650°C. A comparison among other  $\alpha$ -alloys can be made in the sense of one test run to specify the thickness distribution as well as the required punch force during the forming stage in connection with the used  $\alpha$ -alloy.

Results listed in table 4-14 are the mean thickness in the critical positions of the t-duct (a, b and c in figure 4-31) and the punch force. The first three simulation runs merely regarded the variation of the alloy. Here, a pre-defined parameter set was submitted based on previous manufacturing by FormTech. As can be seen in figure 4-31, thickness in positions (a) and (c) distinguishes KS and XT upon Gr.04. Since position (c) would be trimmed later and does not belong to the final product (dashed lines in figure 4-31 limit the final product), the main focus

on the quality of the deep drawing is reflected mainly by positions (a) and (b). The latter position exhibits minimum undulation with KS, higher undulation with XT and severe one with Gr.04, especially at the bottom of the half-shell, indicating the goodness of KS drawability.

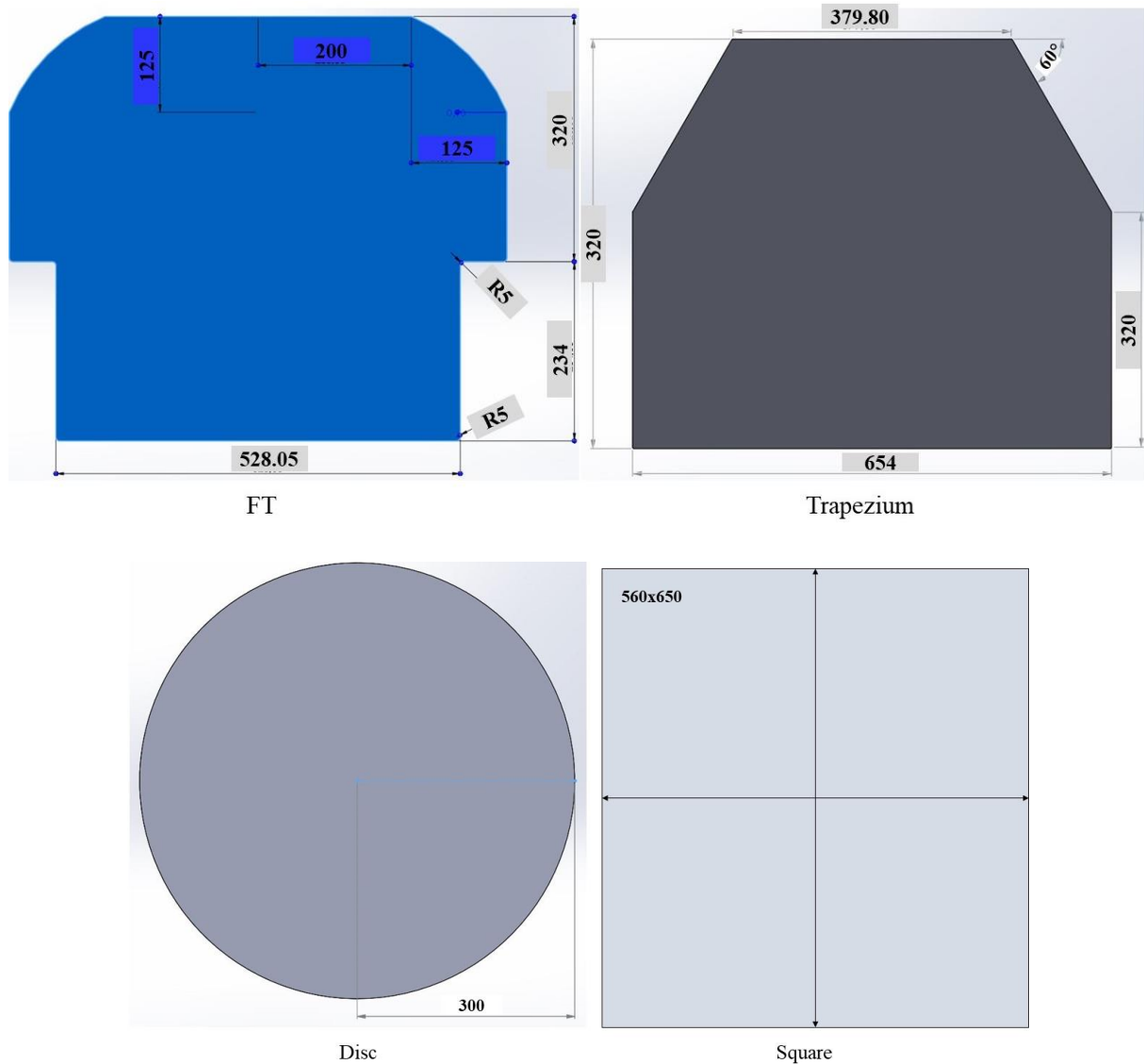


Figure 4-30: Shapes of blank for the FE-study to form a t-duct.

So, the following FE studies will handle KS exclusively. Within the aforementioned test runs, a cubic shape of the blank has been used. Since there is sufficient material around the drawn area, the effect of the blank holder can be more positively availed, whereas the area of contact between the blank and the holder is quite enough. However, the material loss is remarkable, and the required  $F_p$  becomes very high. According to table 4-14,  $F_p$  seems to be smaller when a disc is used.

No.	Alloy	T (Blank)	T (Die)	$\mu_f$	$F_{bh}$	Model	Shape	Results	
		[°C]	[°C]	--	[kN]	Criterion		$W_{crtc}$ [mm]	$F_p$ [kN]
1	KS	730	730	0.35	50	Hill	Square	0.7	670
2	XT	730	730	0.35	50	Hill	Square	0.68	700
3	Gr.04	730	730	0.35	50	Hill	Square	0.67	330
4	KS	730	730	0.35	50	Hill	Disc	0.72	224
5	KS	730	730	0.3	50	Hill	Disc	0.7	236
6	KS	730	730	0.35	60	Hill	Trapezium	0.66	330
7	KS	650	650	0.35	75	Hill	FT	0.68	300
8	KS	650	650	0.2	60	Hill	FT	0.73	460
9	KS	650	650	0.2	75	Hill	FT	0.8	475
10	Ti64	650	650	0.2	75	Hill	FT	Crack on flange	
11	KS	650	650	0.1	60	Barlat	FT	0.66	1000
12	Ti64	650	650	0.1	60	Barlat	FT	torn	700

Table 4-14: FE- study approach to form a t-duct.

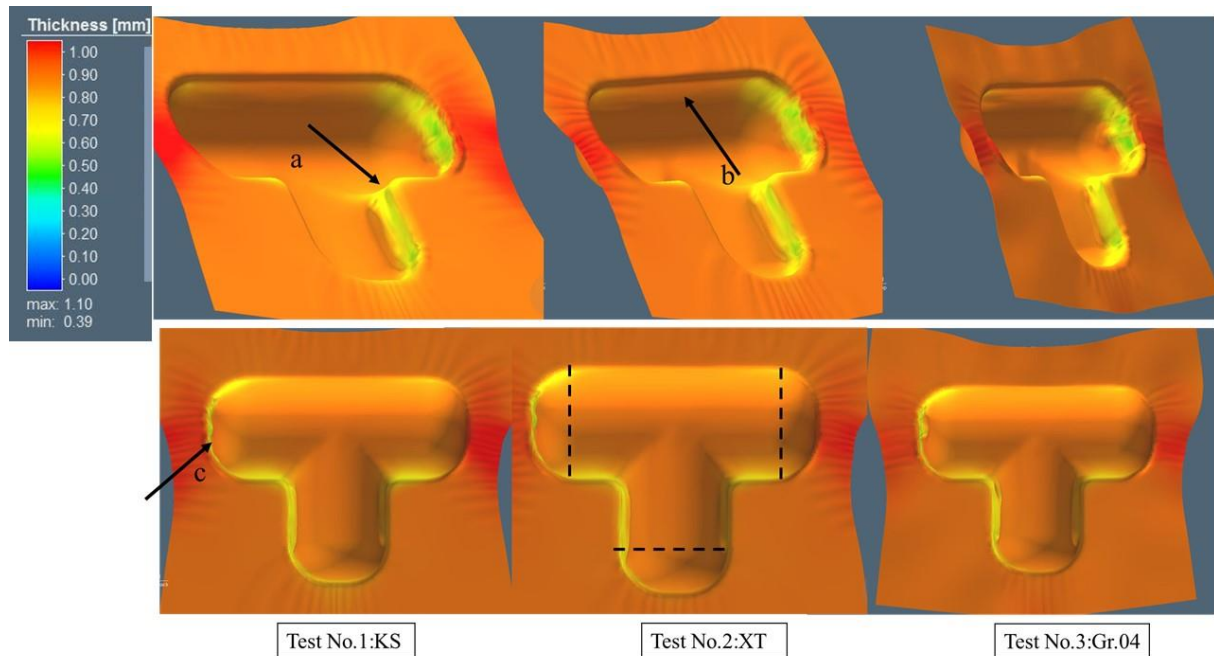


Figure 4-31: FE-comparison between the quality of critical positions after HDD on  $\alpha$ -alloys.

Indeed, the only benefit of using a disc blank is to perform the process with small axial forces. However, the quality of the t-duct, as well as the thickness distribution in the case of a square shape, is noticeably better, as can be seen in figure 4-32.

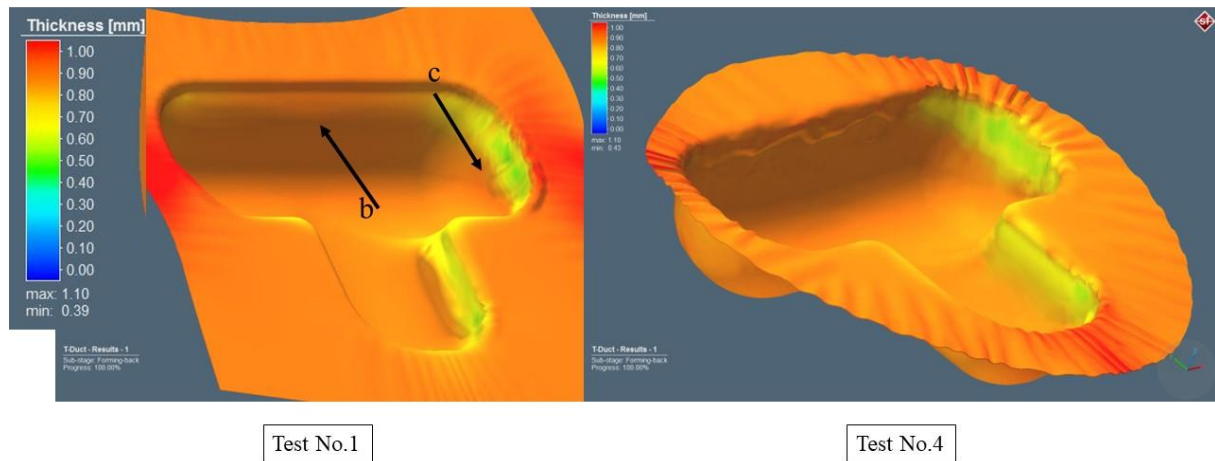


Figure 4-32: FE-comparison between square and disc for KS at 730°C.

The spoken material loss is observed in both cases and is a matter of concern. For this reason, a so-called trapezium shape of the blank is chosen to adapt the material flow in the critical positions. As shown in figure 4-33, despite the higher undulation in the flange area, the main body of the t-duct is shaped more uniformly with trapezium. Figure 4-33 also reveals some unfavorable thickness gradients on the bottom of the half-shell. Such an observation might be a result of high  $\mu_f$  so that the material flow within the deep drawing process is not identical everywhere.

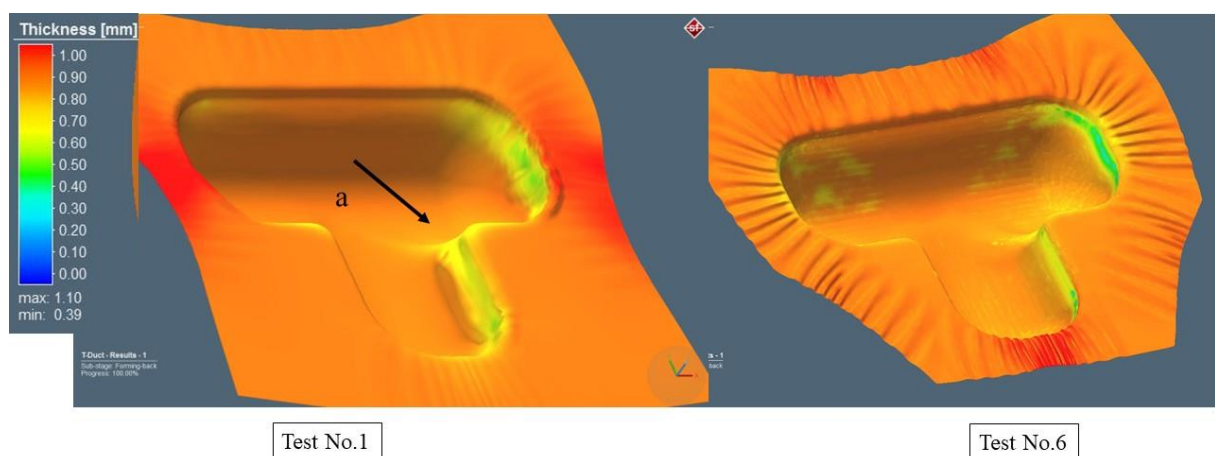


Figure 4-33: FE-comparison of thickness distribution between square and trapezium for KS at 730°C.

The thickness increase of the corresponding flange area confirms this statement. The plastic strain distribution, depicted in figure 4-34, is more uniform, and the degree of deformation is less, which is readily clear in position (a). Consequently, usage of the trapezium is preferable upon square blank.

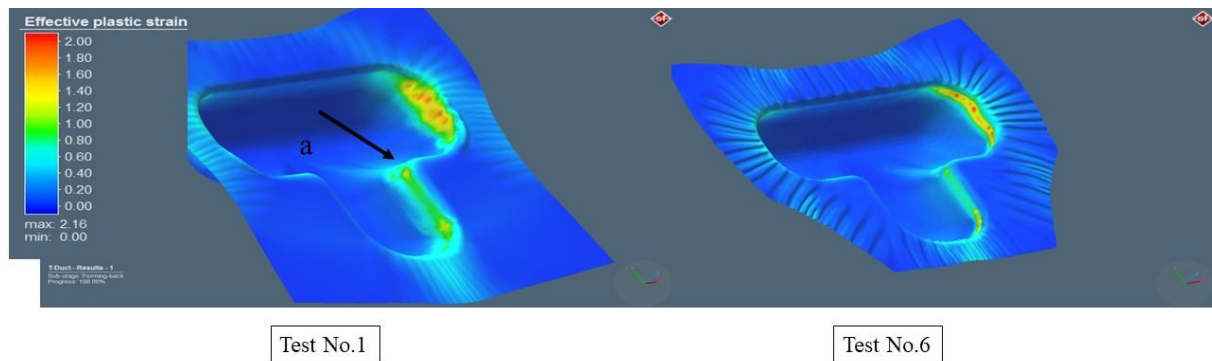


Figure 4-34: FE-comparison of material flow between square and trapezium for KS at 730°C.

Obviously, HDD conditions become better with the adaptation of the blank shape. However, some challenges still exist in the case of the trapezium. The 4<sup>th</sup> suggested blank contour is the so-called FT-contour, which stands for FormTech, as displayed in figure 4-30. In this variety, the blank is so outlined that the distance between the wall of the half-shell and the outer edge of the blank becomes smaller without reducing the flange area near the critical positions. For this purpose, three new test runs were conducted (tests no. 7, 8 and 9). The simulation has been implemented with a symmetry plane to reduce the solving time. So, the depiction of the half-shell is compacted to the quarter-shell.

Here,  $\mu_f$  has been varied between 0.2 and 0.35 and  $F_{bh}$  between 60 and 75kN. Thickness distribution, shown in figure 4-36, came up to the expectations and delivered better results than those corresponding to the shape of a trapezium. The thickness deviation from the origin could have been scaled down from 0.24 to 0.1 mm. Moreover, the thickness gradient in the spoken area is diminished in the case of FT-contour. Undulation in the flange area also becomes lower. The latter feature was not similar in all three tests, though. Apparently, the combination of increasing  $F_{bh}$  with reducing  $\mu_f$  delivers the goods. In addition, the required  $F_p$  with FT-contour is smaller than the square shape. However, it rises with the increase of  $F_{bh}$ .

The comparison of residual equivalent stress in figure 4-35 confirms that the correlation of reduction  $\mu_f$  with increasing  $F_{bh}$  results in a relatively lower value of effective stress. The mean value of the residual equivalent stress in test no.7 is approximately double of that of test no.8 in the ground of the half-shell, for instance, whereas both  $\mu_f$  and  $F_{bh}$  in test no.7 is lower than

in test no.8. Increasing  $F_{bh}$  with maintaining the low value of  $\mu_f$  caused to achieve a better material flow and, hence lower local stresses.

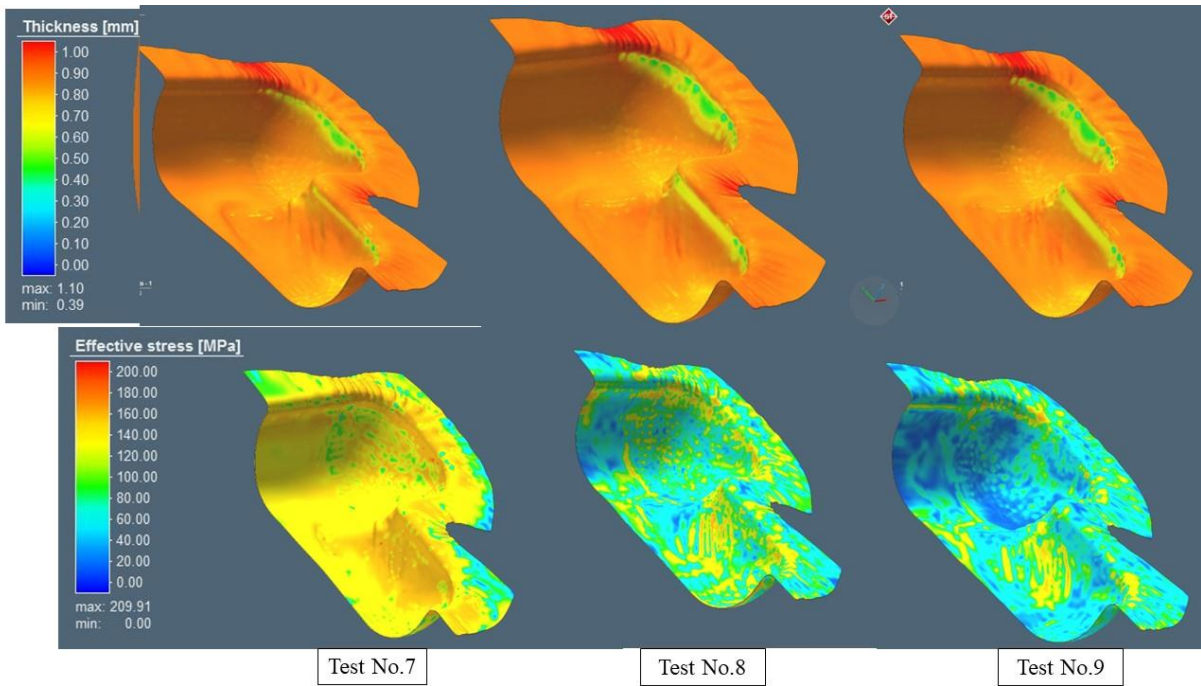


Figure 4-35: Effect of FT-contour,  $\mu_f$  and  $F_{bh}$  on the thickness distribution and effective stress for KS at 650°C.

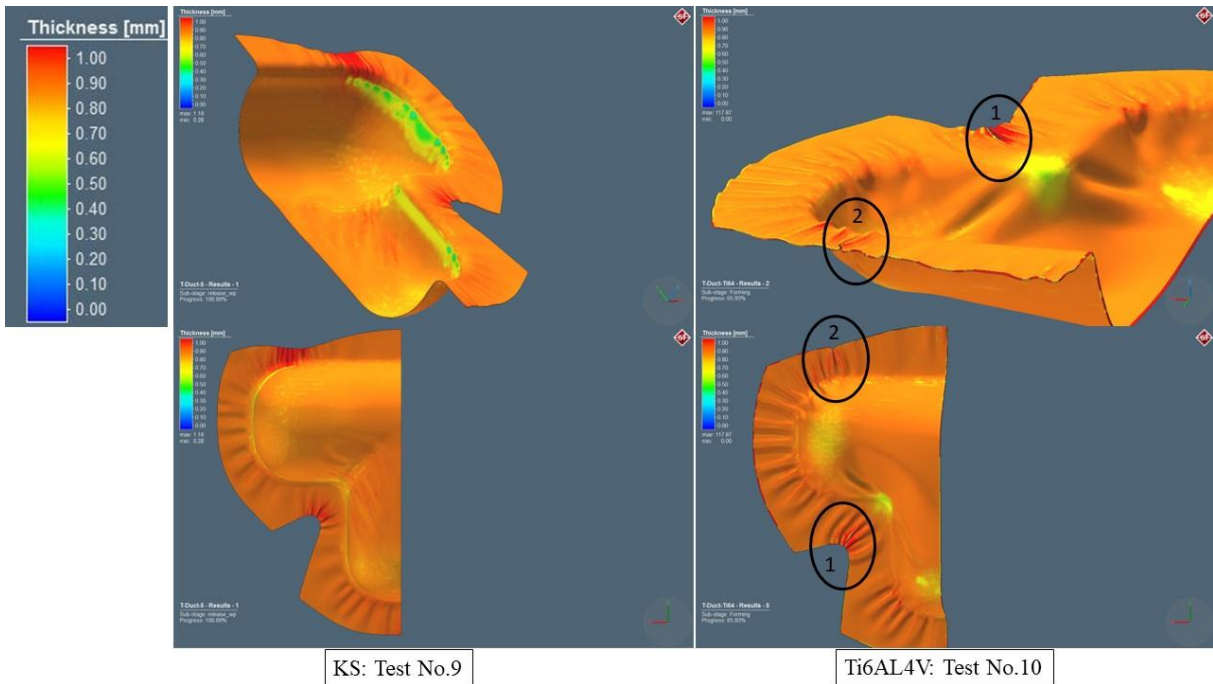


Figure 4-36: FE-comparison for HDD of KS and Ti6Al4V with the best parameters.

It is noteworthy to mention that the abovementioned three FE studies were conducted with a forming temperature of 650°C, which has already been announced as the best temperature level to perform HCF.

Based on the aforementioned FE study, forming at 650°C,  $\mu_f$  of 0.2 and  $F_{bh}$  of 75kN represent the parameter set of the best numerical approach to simulate HDD for titanium  $\alpha$ -Alloys. This matches the statement in [SHAO12] about the good results with a lowering of  $\mu_f$ . A comparison between this run and a similar one but of Ti6Al4V is made to characterize the difference between their HDD efficiency at 650°C. As mentioned in table 4-14 and shown in figure 4-36, the simulation of HDD at 650°C with FT-contour on Ti6Al4V was numerically aborted after 65% of the work. Positions (1) and (2) in figure 4-36 have exhibited a tiny crack, respectively, leading to a stop in the calculation. This is ascribed to the fact of unfavorable high planar anisotropy of Ti6Al4V at this temperature level. There, earing is distinctly pronounced, making the formation of ears at the flange, as well as undulations in the main body of the workpiece, of higher probability. However, figure 4-6 enhanced the statement that Ti6Al4V possess moderate drawability at 650°C despite good ductility.

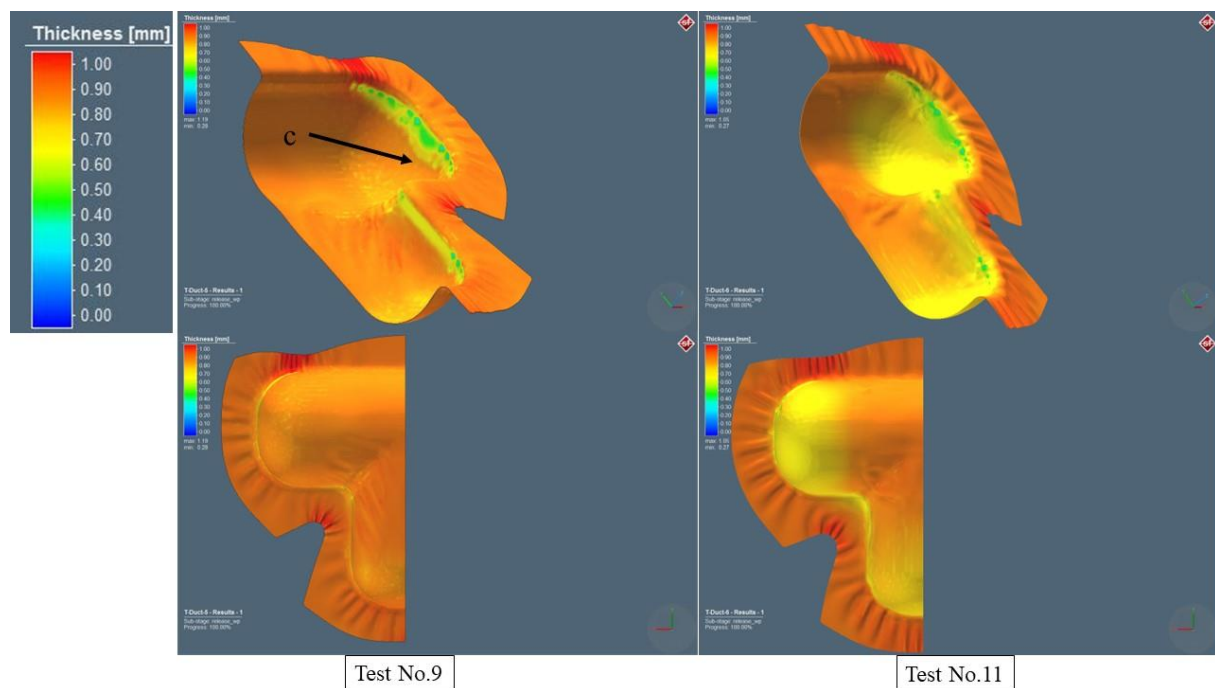


Figure 4-37: FE-study with Hill and Barlat stress state criterion for KS at 650°C.

Another feature to investigate is the consistency of the Hill and Barlat criterion. As expected, Hill48 represents a consistent criterion to describe the material anisotropy at elevated temperatures, contrary to Barlat91, with inconvenient results compared to ones according to

Hill. Test no.11 with the Barlat model reveals higher anisotropic behavior than test no.9 with Hill. Both planar and normal anisotropy are more distinctive with the Barlat criterion. The thickness gradient in the case of Barlat is also higher, especially in position (c). Comparison between both stress state models delivers a significant difference, which should be submitted by fabricating such a product according to the parameters stated in these two FE-forming tests. However, the results obtained above enhance the theory of more consistency of the Hill48 model than the Barlat one to describe the anisotropic behavior of the material within forming at elevated temperatures.

#### 4.8 Realization of FE-results with real T-duct

Thanks to the aid of the industrial company FormTech GmbH, the parameters obtained from the FE study and the statistical study on HCF have been realized to manufacture a half-shell of KS via HDD at 650°C. Results were so convenient that many half-shells were hot deep drawn into a form with no creases and no springback. Formtech has measured the mean thickness of the critical curve after laser beam cutting of the redundant.



*Figure 4-38: Thickness of the critical curve of half-shell manufactured by FormTech<sup>®</sup> according to suggested parameters.*

The mean value amounts to 0.74 mm, as shown in figure 4-38 above, denoting a maximum thinning of less than 10% (the original thickness of the blank was 0.9 mm). Such a value finds industrial acceptance according to the aviation specifications in [DAN 462]. Indeed, results obtained by this study prove the consistency of the Hill model, whereas the numerically forecasted results according to the Hill criterion could have been realized. Moreover, the thickness distribution of the simulation matches the real results to a very large extent. According to test no.9, thickness distribution ranges between 0.75-0.8 in the spoken position, as shown in figures 4-36 and 4-37.

On the other hand, metallographic examinations have been conducted on some samples cut out from a representative half-shell. Positions  $X_1$ ,  $X_2$ , and  $X_3$  were determined considering the critical positions, whereas  $X_1$  represents a sample from a position with a simple material flow.  $X_2$  and  $X_3$  belong to critical positions and are corresponded to positions (a) and (c) in the FE study (see figure 4-31). Four samples have been cut out from position  $X_3$  in order to cover the whole critical area, as shown in figure 4-39 below.

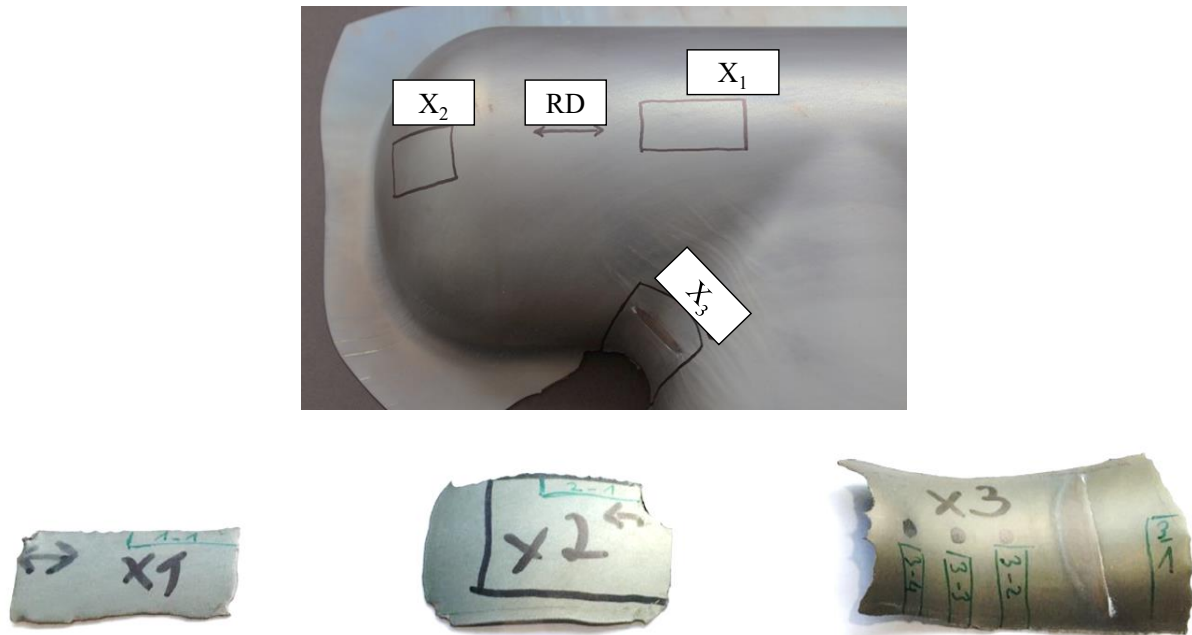


*Figure 4-39: Samples from t-duct half-shell of KS for metallographic examination.*

Irrespective of the investigated position, the process with the selected parameters resulted in a fine-grained structure with a G-index in a range of [7.2-8.5], which corresponds to a minimum number of grains around 1030 per  $\text{mm}^2$  according to ISO 643. In addition, microsections that corresponded with the above positions revealed neither any  $\alpha$ -case layer nor an oxide layer. However, a few white dots could have been observed at position  $X_2$ . In figure 4-40, the spoken position is displayed, as well as a micrograph corresponding to position  $X_1$ . The mean hardness number, measured according to Vickers [HV0.5], amounts to 180. Such a number is a bit higher than measured at  $800^\circ\text{C}$  in table 4-7 since KS exhibits a high softening starting from  $700^\circ\text{C}$ .

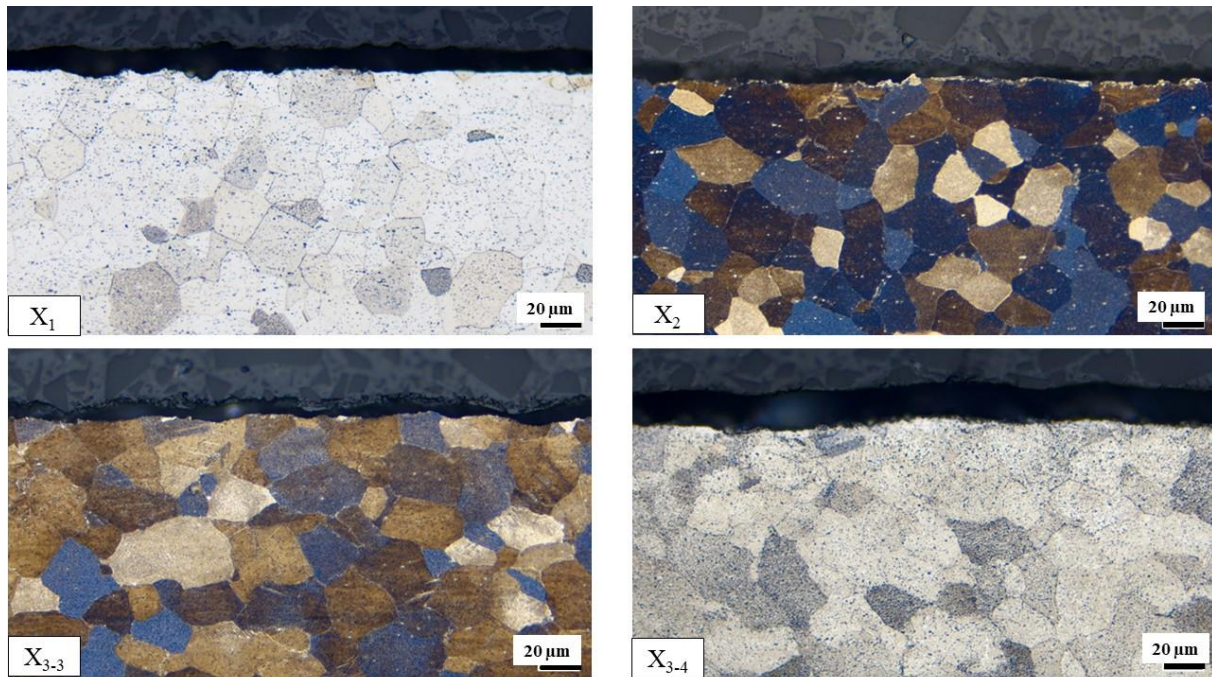


*Figure 4-40: Micrographs of positions from t-duct half-shell fabricated by FormTech based on suggested parameters within this study.*

#### 4.9 Conclusion of the results

The results and discussion section has addressed the behavior of three titanium  $\alpha$ -alloys within HCF in comparison to Ti6Al4V. These are KS1.2ASNEX, Exhaust XT, and ASTM Gr.04. Results obtained can be concluded in the following points:

- $\alpha$ -titanium alloys exhibit convenient ductility at elevated temperatures. Results show a superior elongation before fracture up to 90% in the case of Gr.04. The temperature level of 650°C shows the best plasticity for all three  $\alpha$ -titanium alloys.
- Structural softening causes the work hardening to diminish, starting from 700°C for all three  $\alpha$ -alloys. However, Ti6Al4V can be work-hardened at this temperature level.
- The oxidation resistance of all three  $\alpha$ -alloys is quite convenient, up to 800°C. KS and XT possess the spoken feature better than Gr.04. Not to mention that all of them are better than Ti6Al4V in this context. KS and XT resist the building of TiO<sub>2</sub> scale at the surface. However, an oxygen-enriched layer is built at 800°C. This is called the  $\alpha$ -case layer and is detrimental to the mechanical properties, especially the fatigue endurance, and must be avoided or, if not, removed before transferring to any next process. The regarded  $\alpha$ -alloys resist the formation of the unfavorable  $\alpha$ -case layer up to 700°C.
- ASTM Gr.04 builds a superficial oxide layer starting from 730°C. Such a layer is stable and shows excellent integrity with the base metal, denoting a potential passivating layer against pitting corrosion. A similar layer can also be observed in the case of Ti6Al4V.

However, it does not show the desired integrity with the base metal to announce a pitting corrosion resistance. Forming at high temperatures under the application of protective gas, like argon, for example, prevents the formation of such a layer at the surface even at 800°C.

- Forming at 650°C with a subsequent relaxation time of 700s results in complete stress relief, making a forming with no emergence of springback effect possible.
- Numerical study helps to adapt the marginal conditions of the hot deep drawing process. In this context, the blank holding force and the coefficient of friction are adapted to ensure a crease-free forming process. Material anisotropy is taken into consideration, which sounds, in the case of Ti6Al4V, to be a critical feature within deep drawing at 650°C. Simulations are made according to Hill and Barlat criteria and show an excellent consistency of the Hill model at elevated temperatures.
- T-duct, with 0.9mm thickness, is fabricated by company FormTech via hot deep drawing based on the suggested parameters of this study. The results of such a t-duct are quite satisfying.
- Table 4-15 concludes the best parameters obtained within this doctoral thesis.

Alloy	Forming temperature	Heating time	Relaxation time	Coefficient of friction	Blank holding	Others
	[°C]	[s]	[s]	$\mu_f$ [--]	[kN]	Inert gas
<b>KS1.2ASNEX</b>	650	360	700	< 0.2	75	yes

*Table 4-15: The best parameters to manufacture an exhaust component for aerospace applications from titanium  $\alpha$ -alloys obtained at the end of this dissertation.*

## 5 Summary

The current dissertation presents a profound investigation of the usage of some titanium alloys to fabricate specific aerospace components. These titanium alloys belong to the category of commercially pure titanium alloys. Such a category is incorporated in alpha ( $\alpha$ ) titanium alloys. In the aviation industry, some titanium alloys find important use in manufacturing exhaust components via hot sheet forming. ASTM Gr.02, Ti6Al4V, and, recently, Ti6242 are the most famous ones. ASTM Gr.02 possesses a very good potential for hot forming owing to its convenient ductility as well as the superior oxidation resistance to a very great extent at elevated temperatures. Ti6Al4V and Ti6242 are  $\alpha$ - $\beta$  titanium alloys and possess a moderate oxidation resistance at spoken temperatures. However, such an alloying category can be hardened via heat treatment, contrary to titanium  $\alpha$ -alloys. Therefore,  $\alpha$ - $\beta$  alloys find more industrial use where high strength is needed. On the other hand,  $\alpha$ -alloys exhibit favorable weldability upon other types of titanium alloys. Such a feature is ascribed mainly to oxidation resistance. Another aspect motivating this approach is the economic issue, whereas  $\alpha$ -alloys are less expensive than other types of titanium alloys. All the above-mentioned properties of  $\alpha$ -alloys promote them to be utilized in aerospace applications, where thermal stability is more required than strength.

The presented dissertation deals with three titanium  $\alpha$ -alloys. The 1<sup>st</sup> one is an alloy developed by the Japanese company KOBE.Steel and called KS1.2ASNEX, the 2<sup>nd</sup> is a British alloy from TiMET called Exhaust-XT, and the 3<sup>rd</sup> is the ASTM Gr.04. Both KS and XT alloys have been investigated and introduced as a satisfying replacement to ASTM Gr.02 owing to their oxidation resistance at high temperature and the higher strength at the same time, while Gr.04 could represent a substitution for  $\alpha$ - $\beta$ -alloys since its strength is relatively near to them in untreated conditions and exhibits better oxidation behavior. However, all the aforementioned titanium alloys are attributed to their high elastic energy, resulting in a springback and an inaccuracy in shape after forming. Material anisotropy is also a connected issue to the microtexture of titanium alloys and is undesired with sheet forming since it affects the material flow during the process and leads to the form of the “ears.”

The main focus of this work is on a novel forming method called hot creep forming. It is a hot deep drawing followed by a stress relaxation stage, at which the material flows with a constant strain value. Therefore, any kind of residual stress is expected to minimize or diminish in the best case, eliminating the springback effect. The tensile behavior of the three titanium  $\alpha$ -alloys within hot creep forming has been studied to adapt the best parameters to obtain a sheet-forming method with convenient properties. The output is explained extensively in the following.

The analysis of the forming results introduces the three regarded  $\alpha$ -alloys as promising ones to utilize in the production of exhaust components for civilian airplanes via hot creep forming. The elongation to fracture rises from 25% at room temperature to 65% at elevated temperatures. This strain value indicates excellent ductility. However, the drawability is measured by the wideness of the strain-hardening area before necking in the stress-strain curve. For this reason, KS1.2ASNEX is announced to possess the best deep drawing potential. The best drawability can be observed at 650°C for the former  $\alpha$ -alloy.

Microstructural investigation was made on the samples heated at the range [550-800] °C. It implies a consistent oxidation resistance with no emergence of any oxide scale at the surface. KS1.2ASNEX and Exhaust-XT exhibit a superior oxidation resistance up to 800°C. ASTM Gr.04 cannot resist the formation of a TiO<sub>2</sub> layer at this temperature level. Owing to the high solubility of the oxygen at high temperatures, a layer of  $\alpha$ -phase with high interstitial oxygen is formed at the surface. This phenomenon is called  $\alpha$ -case and drops the mechanical properties of titanium alloys. Such a layer emerges starting from 800°C for KS1.2ASNEX and Exhaust-XT and from 700°C in the case of ASTM Gr.04. The thickness of the  $\alpha$ -case layer is quantified with the aid of light scanning micrographs, while it is distinguished from the oxide layer by means of the EBSD mapping. The microtextural study of the denoted alloy points out an improvement of the material anisotropy at 650°C than at room temperature.

On the other hand, a statistical model is developed to optimize the hot creep forming process. Forming temperature, heating duration, and relaxation time are the most significant factors impacting stress relief and the formation of the  $\alpha$ -case layer according to the regression analysis of a statistical study made on the best alloy KS1.2ASNEX. The latter analysis reveals an equation to estimate the residual stresses in accordance with the variation of the parameters mentioned above. All the regarded alloys reveal a great stress relief to diminish the elastic energy. Starting from 600°C, stress relief of 85% in all cases can be achieved. However, full stress relief is obtained at 700°C, provided that the sample is relaxed for 700s. These suggested combination results are associated with the formation of a neglected thin  $\alpha$ -case layer. The relaxation tests have not distinguished any alloy over the others, whereas both Exhaust-XT and ASTM Gr.04 show convenient stress relief as well as prevention of  $\alpha$ -case presence.

A numerical study enhances the statement of the best suitability of KS1.2ASNEX to conduct a smooth hot deep drawing process. Besides forming temperature, coefficient of friction, blank holding force, and the shape of the blank are adapted within the finite element simulation. According to the results, a custom shape within the dissertation called “FT-contour,” a coefficient of friction of 0.2, and a blank holding force of 75kN cause the undulation during the

deep drawing to diminish and the formation of ears to be superfluous. The thickness distribution of the formed component is also satisfying. The stress state criterion is described numerically by the Hill48 model. Based on the results obtained from the statistical and numerical study, an exhaust component has been manufactured via hot creep forming. It shows a convenient shape with industrially acceptable thickness variation.

The results of the whole approach are represented schematically by the following chart.

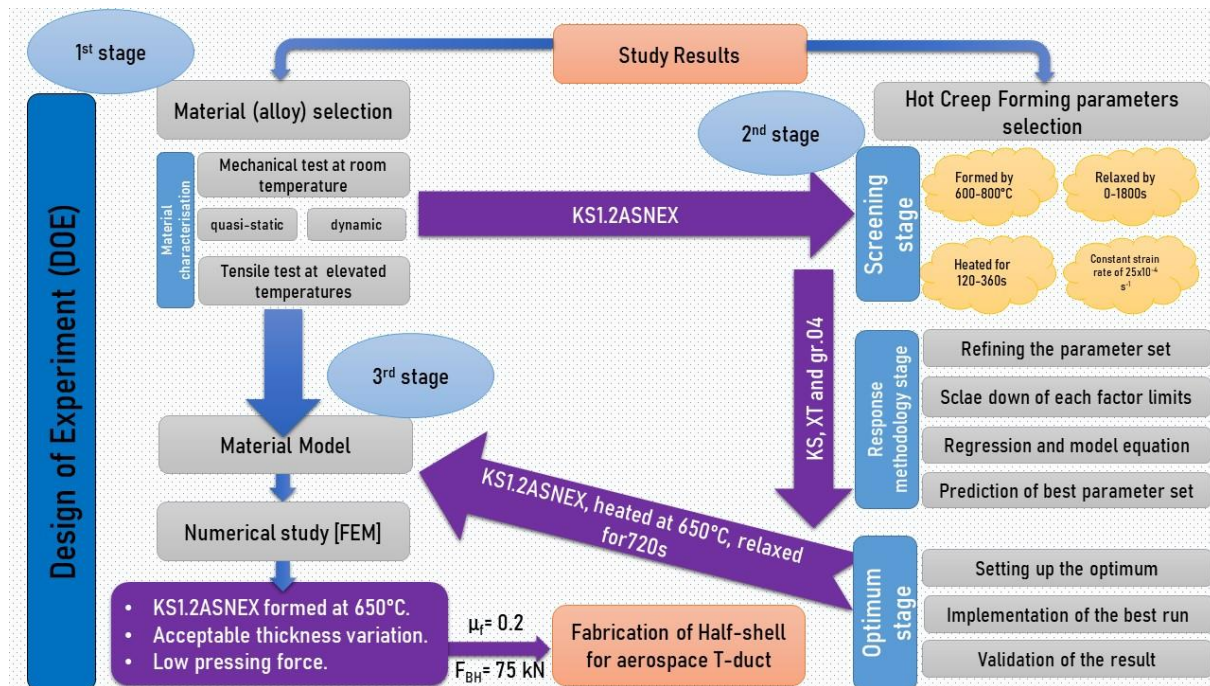


Figure 5-1: Schematic representation of all the results of the approach.

## 6 Outlook

Some features have appeared within this work and open a new horizon of the investigation with intensive research about them. One of them is a physical phenomenon related to the etching effect during the microstructural examination, while the other is an odd path of the stress-strain curve. The variation of  $\mu_f$  was also an issue.

### 6.1 Uneven representation of micrographs

Results of the metallographic examination are presented in sections 4.2 and 4.5 for tensile samples at room temperature as well as at elevated temperatures, respectively. The whole metallographic investigation has been made by materials testers in the Leibniz institute for materials engineering (Leibniz-IWT, Bremen). The execution of sample preparation by the same skilled worker for all the metallographic samples. Since the studied materials belong to the  $\alpha$ -titanium category, a well-known etching method was agreed upon according to FUSS, as explained in section 3.3.3, which had been suggested for such alloys. Nevertheless, some micrographs exhibit an unexpected colored microstructure. Figure 6-1 shows an example of the matter. All the samples are cut out from the same half-shell, i.e., all the samples had undergone the same forming process conditions, as illustrated in section 4.8. It was also confirmed by the responsible department that all the samples had been etched under the same circumstances. The difference in the coloring is still present, though. Such a phenomenon opens a potential study about which factors impact the etchant absorption of the grains.

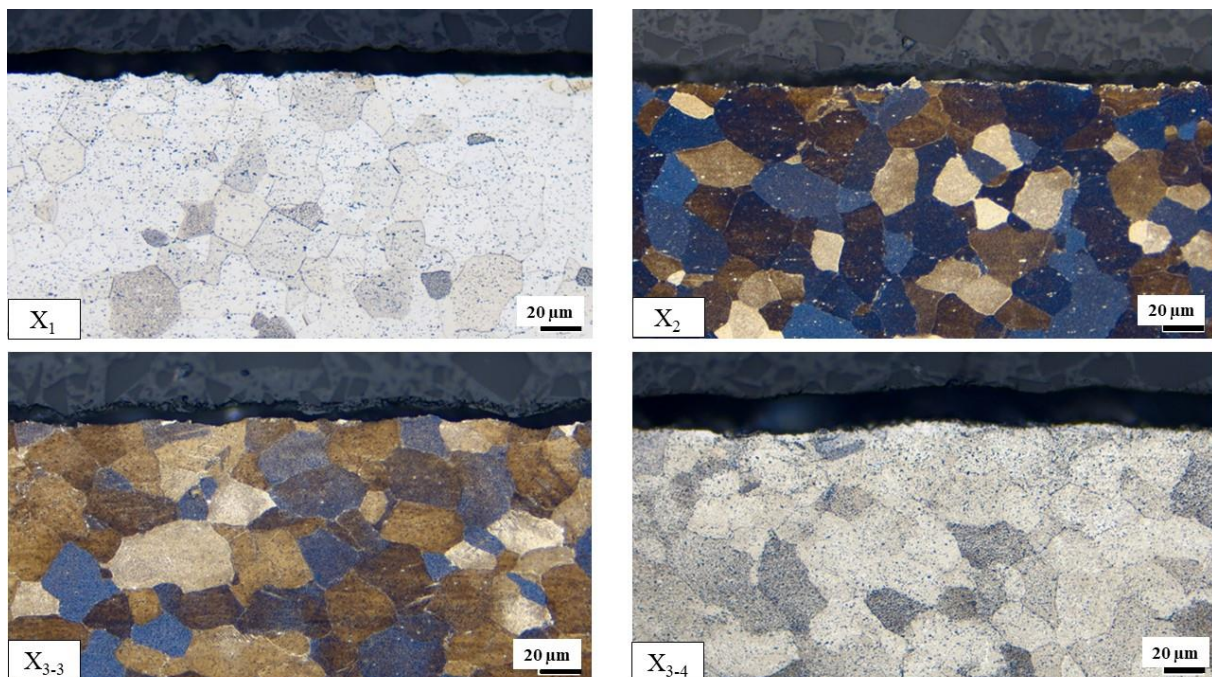


Figure 6-1: Uneven representation of microstructure for similarly prepared samples.

## 6.2 Brittleness at 500°C for ASTM Gr.04 and Exhaust-XT

During the tensile test, an unexpected result has arisen with both Gr.04 and XT. Stress-strain curves, displayed in figure 4-6, have been chosen to represent the whole tensile test, which was made at various temperature levels with three samples, respectively. According to the addressed figure, the elongation before fracture at 400°C is quite bigger than at 500°C in both alloys. Such a strain value returns to normal at 600°C and beyond it. The whole tensile test for the respective three samples of XT is concluded in figure 6-2. A synchrotron radiation beamline has been deployed to look for any possible precipitation as a cause of this phenomenon. However, the small-angle scattering maps have not shown any kind of precipitant. Indeed, the amount of silicon in the case of XT is relatively so small, that a silicon precipitant is formed on the grain boundaries and affects the mechanical properties as obtained by [YUE19]. Such a phenomenon opens a way to pursue the reason for this material behavior and motivate to search for it.

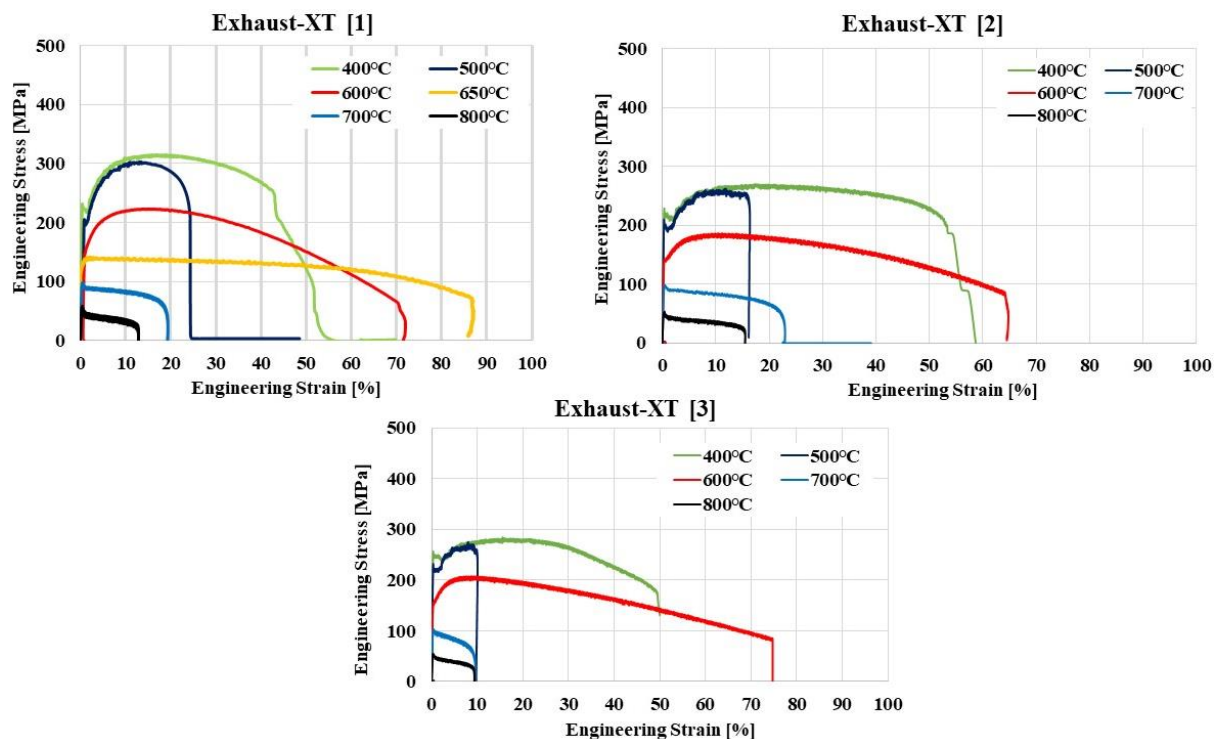


Figure 6-2: Unexpected brittleness at 500°C for XT.

## 6.3 Variation of coefficient of friction between die parts

As illustrated in section 2.2.2,  $\mu_f$  impacts the wall thickness distribution of the formed sheet. Its value is recommended to be low in some areas and high in others. Such an idea remains out of scope and needs to be pursued since it is expected to release a few differences from results obtained in sections 4.7 and 4.8.

## 7 List of literature

- [ABSP17] M. Abspoel, M. Scholting, M. Lansbergen, Y. An, H. Vegter; *A new method for predicting advanced yield criteria input parameters from mechanical properties*, Journal of Materials Processing Technology Vol 248 [2017].
- [AKAM95] T. Akamatsu, S. Ukita, K. Miyasaka, M. Shi; *Deep Drawing of Commercially Pure Titanium Sheets*, ISIJ International Vol. 35 [1995].
- [ANTT20] M-L Antti, V Collado Cipres, J. Mouzon, P. Äkerfeldt, R. Pederson; *Effect of silicon on creep properties of titanium 6Al-2Sn-4Zr-2Mo alloy*, MATEC Web of Conferences 321 [2020]
- [BADR15] O. Badr, B. Rolfe, P. Hodgson, M. Weiss; *Forming of high strength titanium sheet at room temperature*, Material and Design 66 [2015]
- [BADR16] O. Badr, F. Barlat, B. Rolfe, M. Lee; *Constitutive modelling of high strength titanium alloy Ti-6Al-4V for sheet forming applications at room temperature*, International Journal of Solids and Structures Vol.80 [2016].
- [BEAL06] J.D. Beal, R. Boyer, D. Sanders; *metalworking: Sheet Forming*, ASM Handbook- Vol 14B ASM International [2006]
- [CASA20] A. Casadebaigt, D. Monceau, J. Hugues; *High Temperature Oxidation of Ti-6Al-4V Alloy Fabricated by Additive Manufacturing. Influence on Mechanical Properties*, MATEC Web of Conferences 321 [2020]
- [CHAN20] H. Chang, L. Zhou; *Current Situation of Titanium Research, Development and Applications in China*, MATEC Web of Conferences 321 [2020]
- [CHAR13] B. Chartel, E. Massoni; *Deep Drawing of Ti6Al4V: Experiments and Modeling over a Wide range of Strain Rates and Temperatures*, Key Engineering Materials Vols. 554-557 [2013].
- [DAN462] Daimler-Benz Aerospace Airbus, 8<sup>th</sup> Issue, December 97.
- [DIER17] J. Dierdorf, *Investigation of flow curve for forming processes (Ermittlung und Approximation von Fließkurven für Umformprozessen)*, Institute of Metal Forming, RWTH Aachen university [2017].
- [DOEG10] E. Doege, B. Behrens; *Handbook forming "Handbuch Umformtechnik"*, 2<sup>nd</sup> edition, Springer Verlag Heidelberg, [2010].
- [DONA00] M.J. Donachie; *Titanium Guide – 2<sup>nd</sup> edition*, ASM International [2000]
- [DUMO20] N. Dumontet, B. Malard, B. Viguier; *Study on the origins of residual stresses in Ti-6Al-4V processed by additive manufacturing*, MATEC Web of Conferences 321 [2020]
- [DUNS20] M. Dunstan, J. Paramore, B. Butler, Z. Fang; *The uses and applications of hydrogen processing for titanium additive manufacturing*, MATEC Web of Conferences 321 [2020]
- [FIOR15] A. Fiorentino, E. Ceretti, C. Giardini; *Experimental and numerical method for the analysis of warm titanium sheet stamping of an automotive component*; Advances in materials science and Engineering; Vol. [2015]
- [FUNC20] C. Funch, K. Somlo, K. Poullos, S. Mohantym M. Somers, T. Christiansen; *The influence of microstructure on mechanical properties of SLM 3D printed Ti-6Al-4V*, MATEC Web of Conferences 321 [2020].
- [GAIA10] S. Gaiani, S. Jurendic, P. Veronesi; *Plastic Deformation of  $\alpha$  Titanium Alloys Sheets*, International Titanium Association [2010]
- [GERS05] B.Gershon, I.Edror; *Research and application of superplastic forming titanium alloys for commercial aircraft parts*; Material science forum, Vols. 475-476 [2005]

- [GWYN07] B. Gwynne, P. Lyon; *Magnesium alloys in aerospace: applications, past concerns, current solutions*, Triennial International Aircraft Fire & Cabin Safety Research Conference; New-Jersey-USA [2007].
- [HARA14] Y. Harad, M. Ueyama; *Formability of pure titanium sheet in square cup deep drawing*, Procedia Engineering 81 [2014]
- [ISMA16] A. Ismail, M.S. Mohamed; *Review on sheet metal forming process of aluminum alloys*; Proceedings of the 17<sup>th</sup> Int. AMME conference [2016].
- [ISO10113] Determination of plastic strain ration [en] 2006
- [ISO643] Micrographic determination of the apparent grain size [en] 2019
- [JAMB02] S. Jambu, B. Lenczowski, R. Rauh; *Creep forming of AlMgSc alloys for aeronautical and space applications*; ICAS Congress [2002]
- [JESH11] R. Jeshvaghani, M. Emami, H.R. Shahverdai, S.M.M. Hadavi; *Effects of time and temperature on the creep forming of 7075 aluminum alloy: Springback and mechanical properties*, Materials Science and Engineering A 528 [2011]
- [JURE13] S. Jurendic, S. Gaiani; *Numerical Simulation of Cold Forming of  $\alpha$ -Titanium Alloy Sheets*, Journal of Mechanical Engineering 59 [2013].
- [KAIB06] O.A. Kaibyshev, R.V. Safiullin, R.Ya. Lutfullin, O.R. Valiakhmetov, R.M. Galeev, A. Dutta, T. Raghu, G.G. Saha; *Advanced superplastic forming and diffusion bonding of titanium alloy*, Materials Science and Technology Vol.22 [2006].
- [KIM18] H-K. Kim, W-J. Kim; *A Springback Prediction Model for Warm Forming of Aluminum Alloy Sheets using Tangential Stresses on a Cross-Section of Sheet*, MDPI [2018]
- [KOBA01] M. Kobayashi, M. Miyagawa; *Research and development of Superplastic Materials – Recent Progresses and Future Prospects -*, ISIJ Vol 27 [1987] then [2001]
- [KOBE05] KOBE STEEL, LTD Data sheet [2005]
- [KOT14a] N. Kotkunde, A. Deole, A. Gupta, S. Singh, B. Aditya; *Failure and formability studies in warm deep drawing of Ti-6Al-4V alloy*, Materials and Design 60 [2014]
- [KOT14b] N. Kotkunde, S. Rane, A. Gupta, S. Singh; *Analysis of Warm Deep Drawing for Ti-6Al-4V Alloy*, AIMTDR [2014].
- [KRÜP86] W. Krüppers; *On the forming and surface treatment of rustproof sheets*, Thyssen Edelstahl, technical reports Vol. 12 [1986].
- [KULP03] S. Kulp; *Processing of sheet metal components cp-Ti and stainless steel materials*, Doctoral Thesis from “Universität Hannover” [2003]
- [LEE20] M. Lee, Y. Hyun, T. Jun; *Effect of oxygen contents on strain rate sensitivity of commercially pure titanium*, MATEC Web of Conferences 321 [2020]
- [LEYE03] C. Leyens, M. Peters; *Titanium and titanium alloys. Fundamentals and applications*, Weinheim, Chichester; Wiley-VCH [2003]
- [LI12] H. Li, H. Yang, F.F. Song, M. Zhan, G.J. Li; *Springback characterization and behaviors of high strength Ti-3Al-2.5V tube in cold rotary draw bending*, Journal of Materials Processing Technology 212 [2012].
- [LI14] Y. Li, H. NG, H. Jung, H. Kim, Y. Estrin; *Enhancement of mechanical properties of grade 4 titanium by equal channel angular pressing with billet encapsulation*, Materials Letters 114 [2014]
- [LIU01] J. Liu, I. Chen, S. Chou; *Relation between Deformability and Microstructures in a Commercial Pure Ti Sheet Subjected to Dual-temperature Square-shaped Deep Drawing*, ISIJ International Vol.41 [2001].

- [LIU13] J. Liu, M. Tan, Y. Aue-u-lan, M. Guo, S. Castagne, B. Chua; *Superplastic-like forming of Ti-6Al-4V alloy*, International Journal of Advanced Manufacturing Technology Vol. 69 [2013]
- [LIU15] P. Liu, Y. Zong, D. Sahn, B. Guo; *Relationship between constant-load creep, decreasing-load creep and stress relaxation of titanium alloy*, Materials Science & Engineering A 638 [2015]
- [LUO17] H. Luo, W. Li, C. Li, M. Wan; *Investigation of creep-age forming of aluminum lithium alloy stiffened panel with complex structures and variable curvature*, International Journal of Advanced Manufacturing Technology Vol. 91 [2017]
- [LÜTJ07] G. Lütjering, J.C. Williams; *Titanium – 2<sup>nd</sup> edition*, Berlin and New York, Springer Verlag [2007]
- [MACE11] E. Macerauch, H-W. Zoch; *Traineeship in materials (Praktikum in Werkstoffkunde)*, 11<sup>th</sup> Edition, Springer Fachmedien [2011]
- [MAND20] P. Mandal, A. Gomez-Gallegos, D. Gonzalez, H. Elrakayby, P. Blackwell; *Superplastic Behaviour of Ti54M and Ti64*, MATEC Web of Conferences 321 [2020]
- [MANG83] T. Mang; *Lubrication in metal processing (Die Schmierung in der Metallbearbeitung)*, 1<sup>st</sup> edition, Vogel Verlag [1983]
- [MANT20] J. Mantione, M. Garcia-Avila, M. Arnold, D. Bryan, J. Foltz; *Properties of Novel High Temperature Titanium Alloys for Aerospace Applications*, MATEC Web of Conferences 321 [2020]
- [NAWA18] T. Nawaya, A. von Hehl, S. Wagner, W. Beck; *Hot Deep Drawing Processing of Titanium Sheet Metal Parts for High Temperature Application*, AEM Vol. 21 [2018]
- [NEUG06] R. Neugebauer, T. Altan, M. Geiger, M. Kleiner, A. Sterzing; *Sheet Metal Forming at Elevated Temperatures*, Annals of the CIRP Vol. 55 [2006]
- [ODEN08] E. Odenberger, R. Pederson, M. Oldenburg; *Thermo-mechanical material response and hot sheet metal forming of Ti-6242*, Material Science and Engineering A 489 [2008]
- [ODEN10] E. Odenberger; *Direct-hit Development- Thermo mechanical sheet metal forming of components for load carrying aero engine structures*, Industrial Development Centre in Olofsröm AB/OSAS [2010]
- [ODEN11a] E. Odenberger, M. Oldenburg, P. Thilderkvist, T. Stoehr, J. Lechler, M. Merklein; *Tool development based on modelling and simulation of hot sheet metal forming of Ti-6Al-4V titanium alloy*, Journal of Material Processing Technology 211 [2011]
- [OROZ18] A. Orozco-Caballero, F. Li, D. Ojos, M. Atkinson, J. da Fonseca; *On the ductility of alpha titanium: The effect of temperature and deformation mode*, Acta Materials (Materialia) [2018]
- [OZTU10] F. Ozturk, R. Ecmel Ece, N. Polat, A. Koksall; *Effect of Warm Temperature on Springback Compensation of Titanium Sheet*, Materials and Manufacturing Processes, Vol. 25 [2010]
- [OZTU13] F. Ozturk, R. Ecmel Ece, N. Polat, A. Koksall, Z. Evis; *Mechanical and microstructural evaluations of hot formed titanium sheets by electrical resistance heating process*, Materials Science & Engineering A 578 [2013]
- [PANT01] S.N. Patankar, Y.T. Kwang, T.M. Jen; *Alpha casing and superplastic behavior of Ti-6Al-4V*, Journal of Materials Processing Technology – 112 [2001]
- [PETZ94] G. Petzow; *Metallographic etching (metallographisches Ätzen)*, 7. Edition, Gebrüder Borntaeger, Stuttgart [1994].
- [PFAL13] R. Pfaller, A. Weinert; *Statistical Investigation of Composite and Metallic Coupon and Component Tests*, 27<sup>th</sup> ICAF Symposium [2013]

- [POLM17] I. Polmear, D. StJohn, J.F. Nie, M. Qian; *Light alloys – 5<sup>th</sup> edition*, ELSEVIER [2017]
- [RADA07] D. Radaj, M. Vormwald; *Fatigue strength (Ermüdungsfestigkeit)*, 3<sup>rd</sup> Edition, TU-Darmstadt [2007]
- [RIBE10] F.C. Ribeiro, E.P. Marinho, D.J. Inforzato, P.R. Costa, G.F. Batalha; *Creep age forming: a short of fundamentals and applications*, AMME Vol. 43 [2010]
- [ROBE84] W. Roberet, D. Wilson; *Warm forming of titanium sheets*, 5<sup>th</sup> International Conference on Titanium [1984].
- [SANA20] G. Sana; *Titanium Hot Forming In The Aerospace Industry*, MATEC Web of Conferences 321 [2020]
- [SATO07] E. Sato, S. Sawai, K. Uesugi, T. Takami, K. Furukawa, M. Kamada, M. Kondo; *Superplastic Titanium Tanks for Propulsion System of Satellites*, Material Science Forum Vol. 551-552 [2007]
- [SCOT94] JR. Scott; *Material properties handbook, Titanium Alloys*, ASM International [1994].
- [SHAO12] J. Shao-song, L. Zhen, H. Xiao-dong, W. Guo-feng, Z. Kai-feng; *Superplastic forming Ti-6Al-4V titanium alloy cylinder with near uniform thickness distribution*, Transactions of Nonferrous Metals Society of China [2012]
- [SHIP91] M. H. Shipton, W.T. Roberts; *Hot deep drawing of titanium sheet*, Materials Science and Technology Vol. 7 [1991]
- [SIEM07] J. Siemiawski, M. Motyka; *Superplasticity in titanium alloys*, Journal AMME Vol. 24 [2007].
- [SMIR17] I. Smirnov, A. Polyakov, Y. Sudenkov; *Strength and fracture ultrafine-grained titanium Grade 4*, Procedia Structural Integrity 6 [2017]
- [STUT14] L. Stutz, W. Beck, S. Arends, M. Horstmann, V. Ventzke, N. Kashaev; *Material saving and cost reduction with hot forming of U-shaped titanium part*, Material, -wiss u. Werkstofftechnik, Wiley-VCH Verlag, 45 No. 9 [2014]
- [SUWA14] S. Suwas, R. Ray; *Crystallographical Texture of Materials*, Engineering Materials and Processes, Springer Verlag [2014]
- [SWAL04] W. Swale, R. Broughton; *Applying Superplastic Forming Principles to Titanium Sheet Metal Forming Problems*, Material Science Forum, Trans Tech Publications, Switzerland, Vols. 447-448 [2004].
- [TAKA20] K. Takahashi, K. Mori, H. Takebe; *Application of Titanium and its Alloys for Automobile Parts*, MATEC Web of Conferences 321 [2020]
- [TIME10] TIMET, *Properties of TIMETAL® Exhaust XT Sheets + Tubes for Automotive Exhaust Applications*, Henderson Technical Laboratory TIMET [2010]
- [TRIE08] F. Treifenbach; *Design of Experiments: The D-Optimal Approach and Its Implementation As a Computer Algorithm*, Bachelor Thesis from Department of Computing Science, UMEA University [2008]
- [WEIß07] W. Weißbach; *Materials (Werkstoffkunde)*, 16<sup>th</sup> edition, Viewegs [2007]
- [WENB07] H. Wenbo, Z. Kaifeng, W. Guofeng; *Superplastic forming and diffusion bonding for honeycomb structure of Ti-6Al-4V alloy*, Journal of Materials Processing technology Vol. 183 [2007]
- [WON15] J. Won, C. Park, S. Hong, C. Lee; *Deformation anisotropy and associated mechanisms in rolling textured high purity titanium*, Journal of Alloys and Compounds 651 [2015]
- [XIAO15] J. Xiao, D. Li, X. Li, P. Ding, K. Zhao, X. Huang, M. Xu; *Process parameter optimization of Ti-6Al-4V alloy sheet during hot stretch-creep forming*, Trans. Nonferrous Metals Society in China Vol.25 [2015]

- [YUE19] K. Yue, J. Liu, H. Zhang, H. Yu, Y. Song, Q. Hu, Q. Wang, R. Yang; *Precipitates and alloying elements distribution in near  $\alpha$  titanium alloy Ti65*, Journal of Materials Science & Technology [2019].
- [ZHAN13a] J. Zhang, Y. Deng, S. Li, Z. Chen, X. Zhang; *Creep age forming of 2124 aluminum alloy with single/double curvature*, Transactions of Nonferrous Metals Society of China [2013]
- [ZHAN13b] Q. Zhang, Q. Cao; *Planar anisotropy of commercially pure titanium sheets*, Rare Metals Vol. 32 [2013]
- [ZHAN14] T. Zhang, Y. Liu, D. Sanders, B. Liu, W. Zhang, C Zhou; *Development of fine-grain size titanium 6Al-4V alloy sheet material for low temperature superplastic forming*, Material Science & Engineering A 608 [2014]
- [ZHAN19] J. Zhang, Z. Jiang, F. Xu, M. Chen; *Effects of Pre-stretching on Creep Behavior, Mechanical Property and Microstructure in Creep Aging of Al-Cu-Li-alloy*, MDPI Vol.12 [2019]
- [ZON15a] Y. Zong, P. Liu, B. Guo, D. Shan; *Springback evaluation in hot  $v$ -bending of Ti-6Al-4V*, International Adv. Manufacturing Technology Vol. 76 [2015]
- [ZON15b] Y. Zong, P. Liu, B. Guo, D. Shan; *Investigation on high temperature short-term creep and stress relaxation of titanium alloy*, Materials Science & Engineering A 620 [2015]

## 8 Appendix

### Overview of all the fitted flow curves

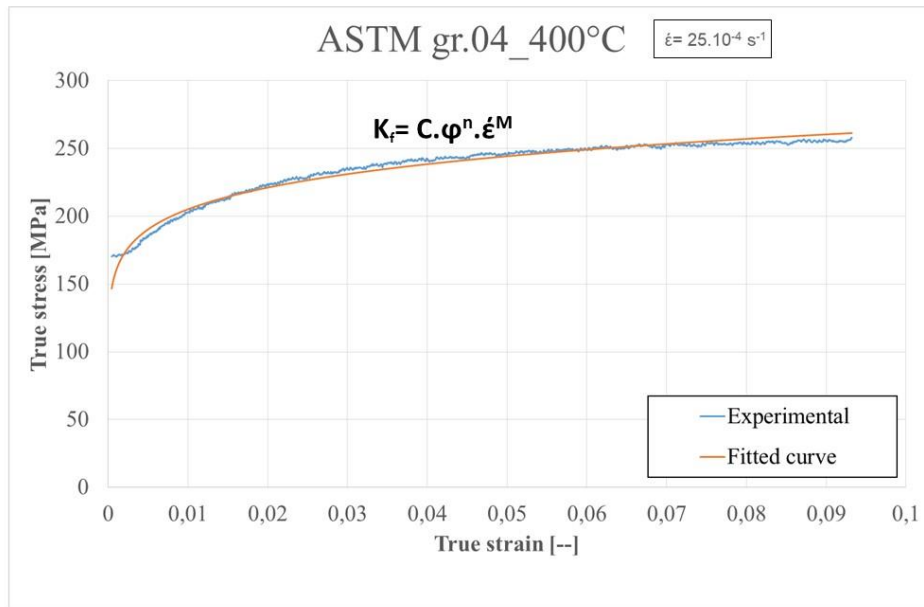


Figure 8-1: Fitted flow curve at 400°C for Gr.04.

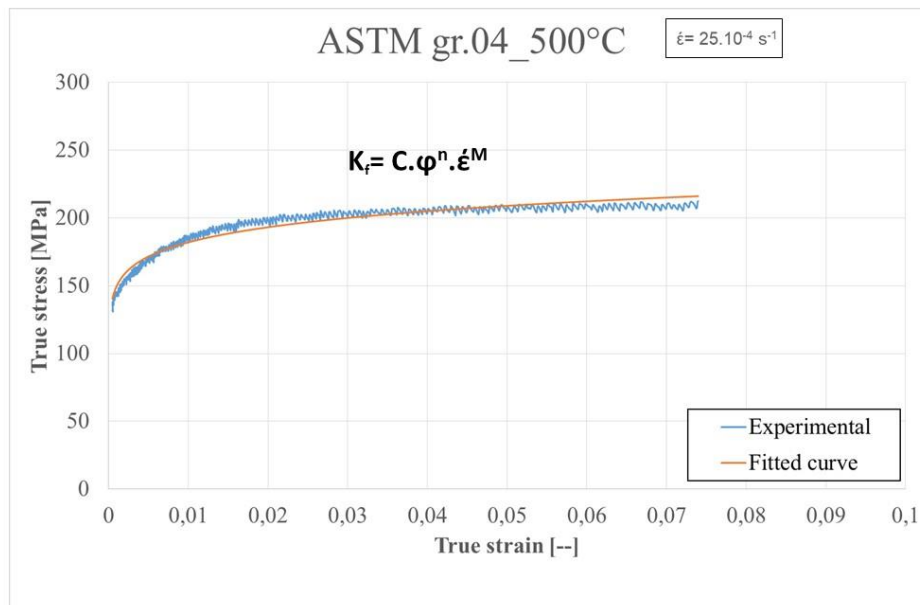


Figure 8-2: Fitted flow curve at 500°C for Gr.04.

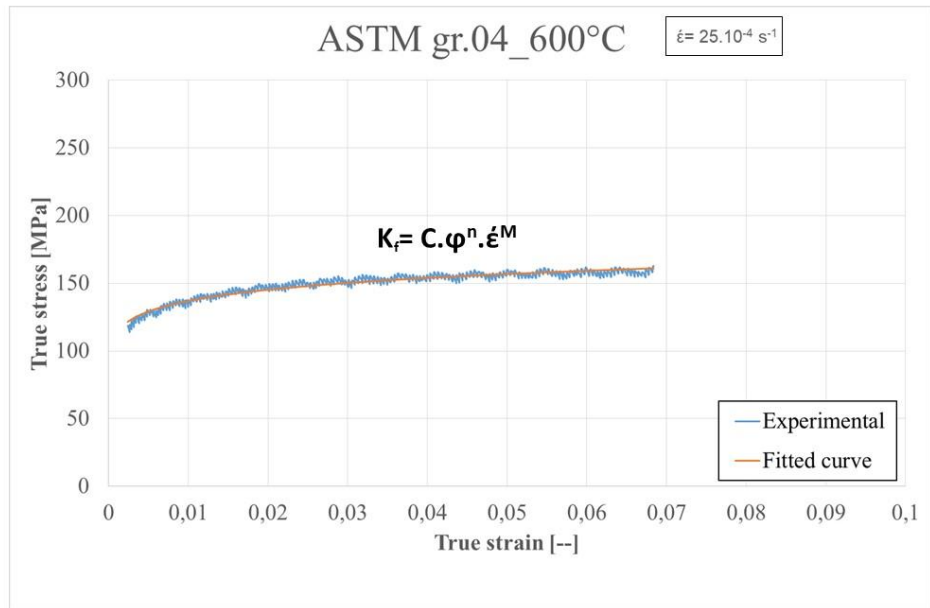


Figure 8-3: Fitted flow curve at 600°C for Gr.04

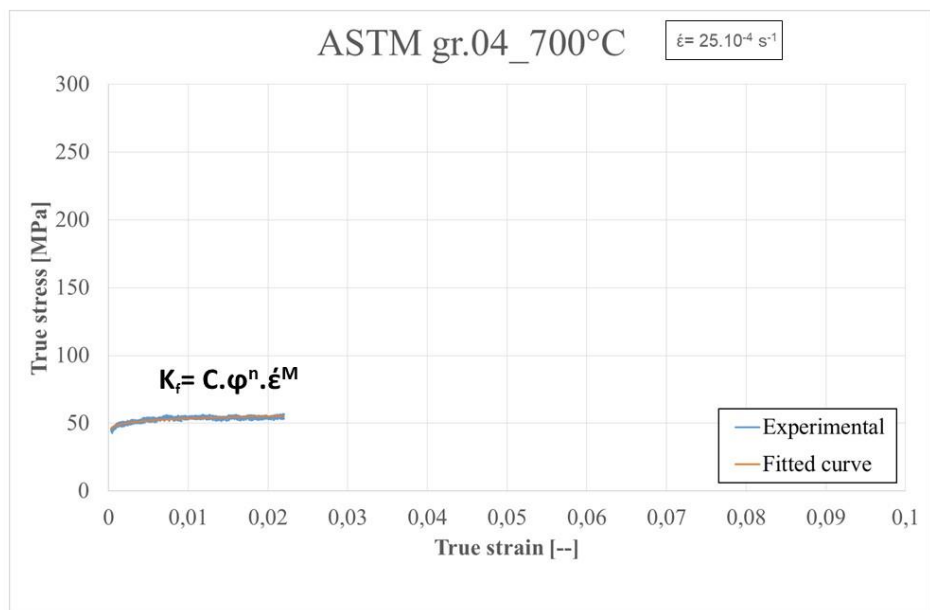


Figure 8-4: Fitted flow curve at 700°C for Gr.04.

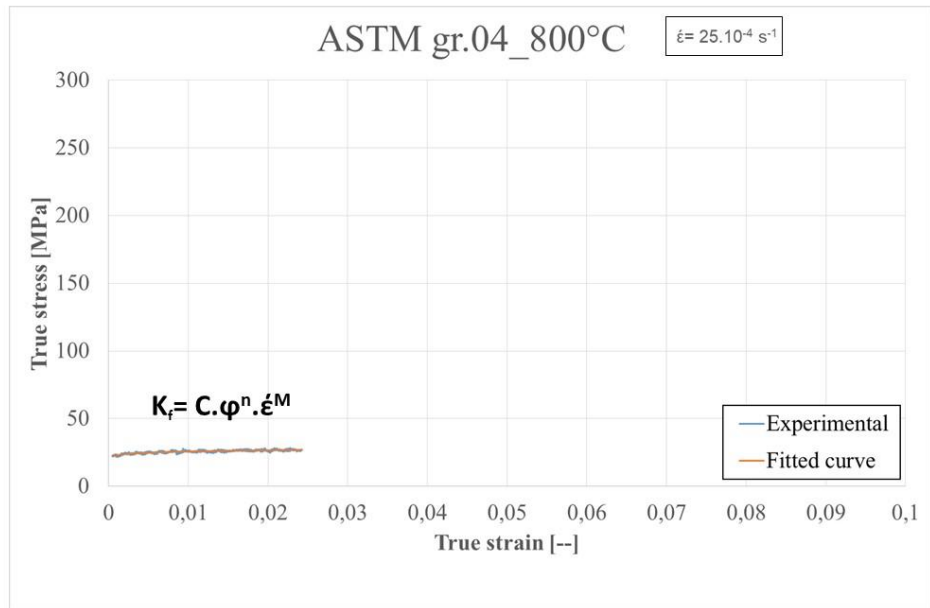


Figure 8-5: Fitted flow curve at 800°C for Gr.04.

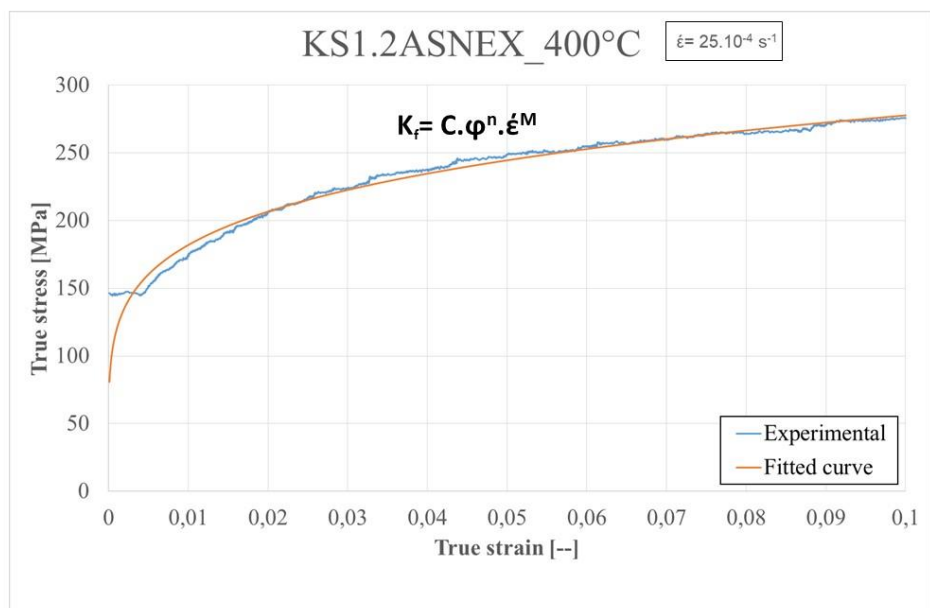


Figure 8-6: Fitted flow curve at 400°C for KS.

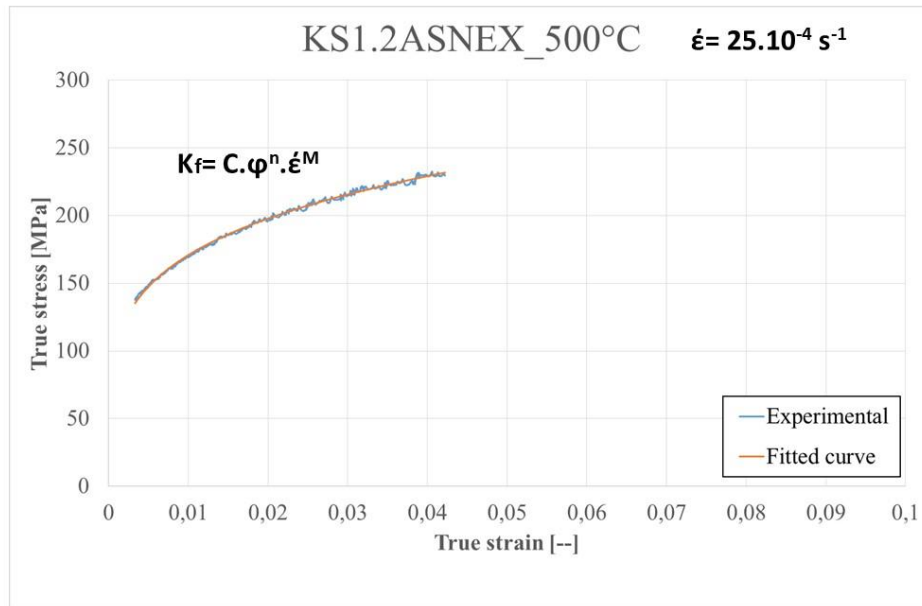


Figure 8-7: Fitted flow curve at 500°C for KS.

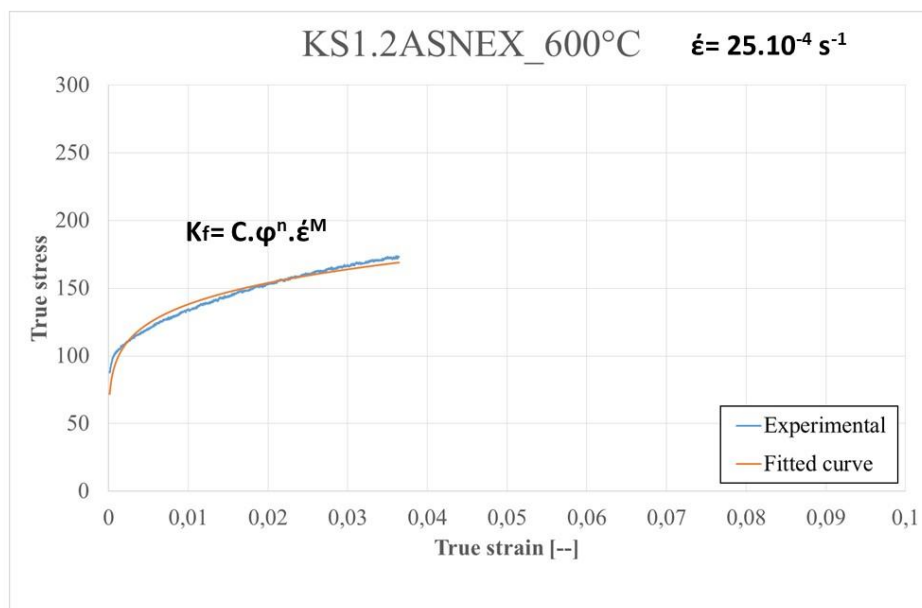


Figure 8-8: Fitted flow curve at 600°C for KS.

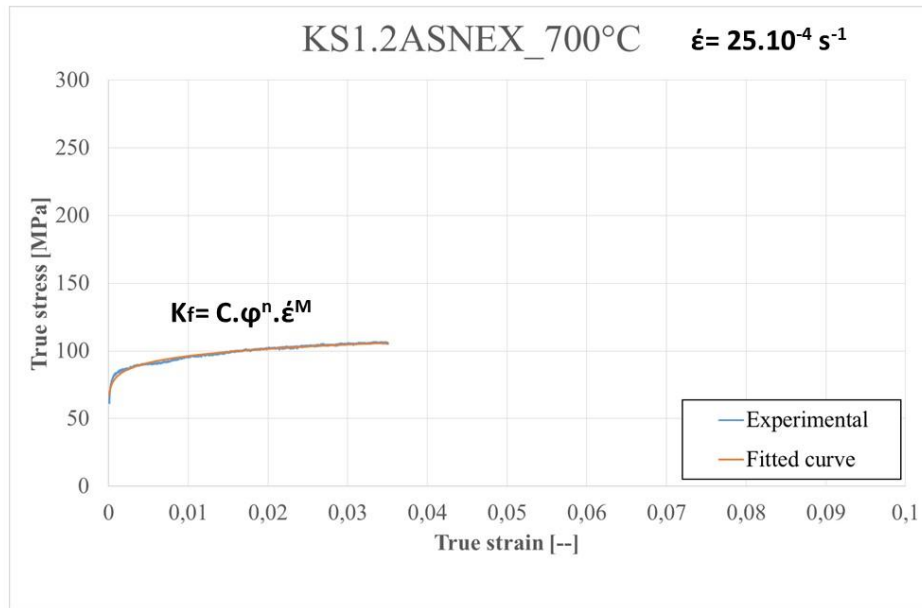


Figure 8-9: Fitted flow curve at 700°C for KS.

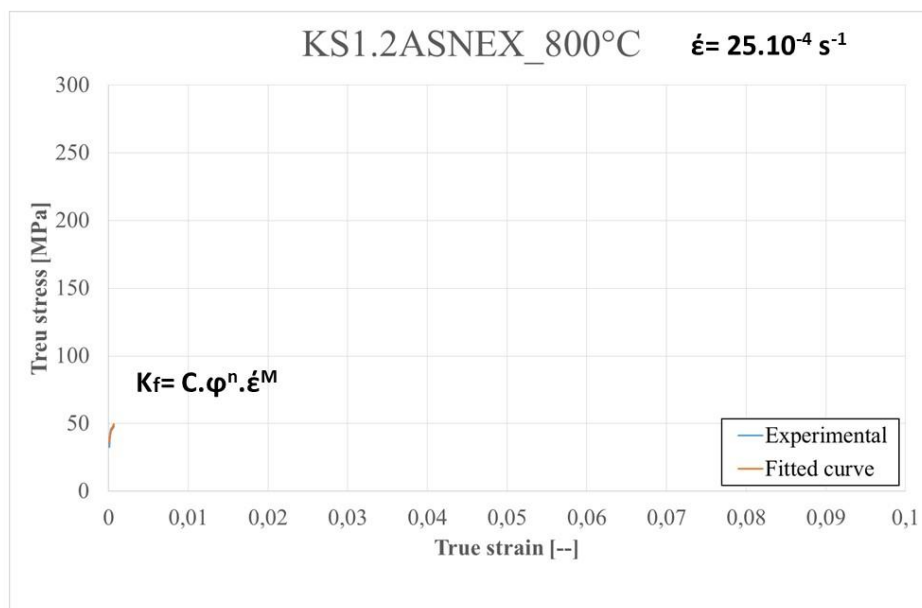


Figure 8-10: Fitted flow curve at 800°C for KS.

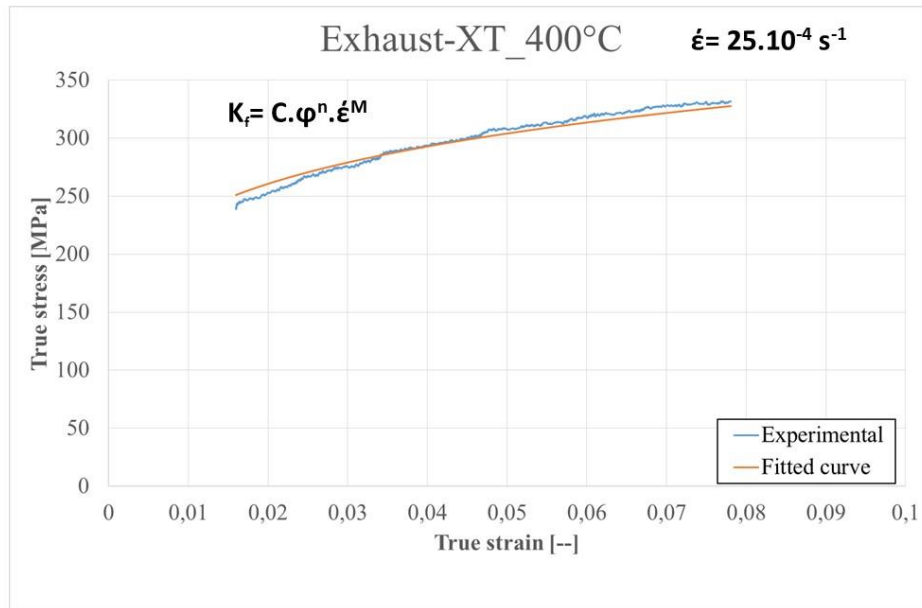


Figure 8-11: Fitted flow curve at 400°C for XT.

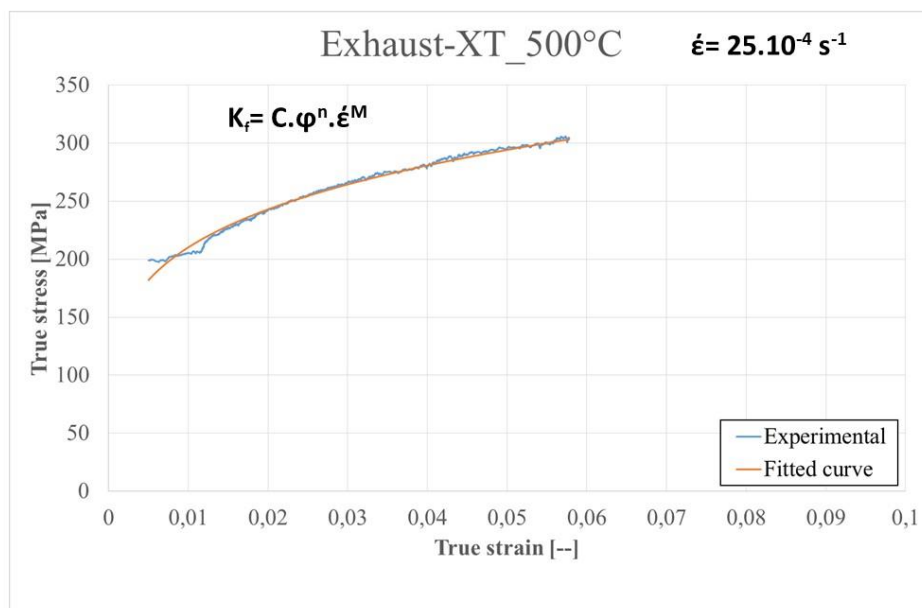


Figure 8-12: Fitted flow curve at 500°C for XT.

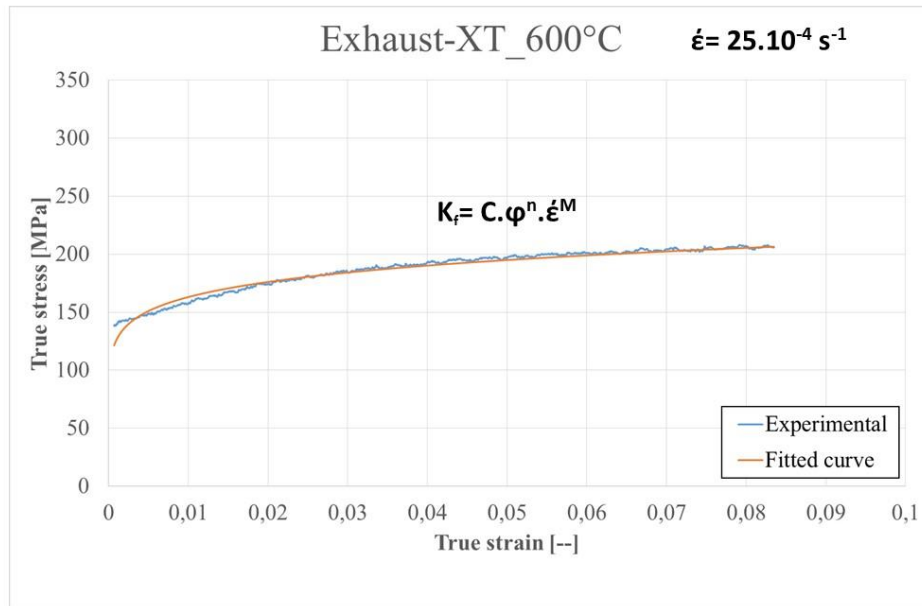


Figure 8-13: Fitted flow curve at 600°C for XT.

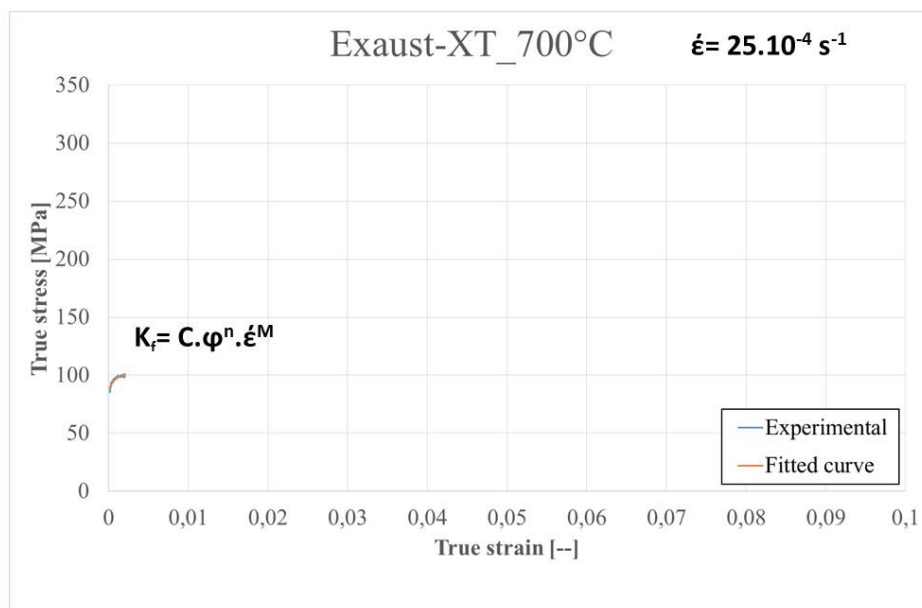


Figure 8-14: Fitted flow curve at 700°C for XT.

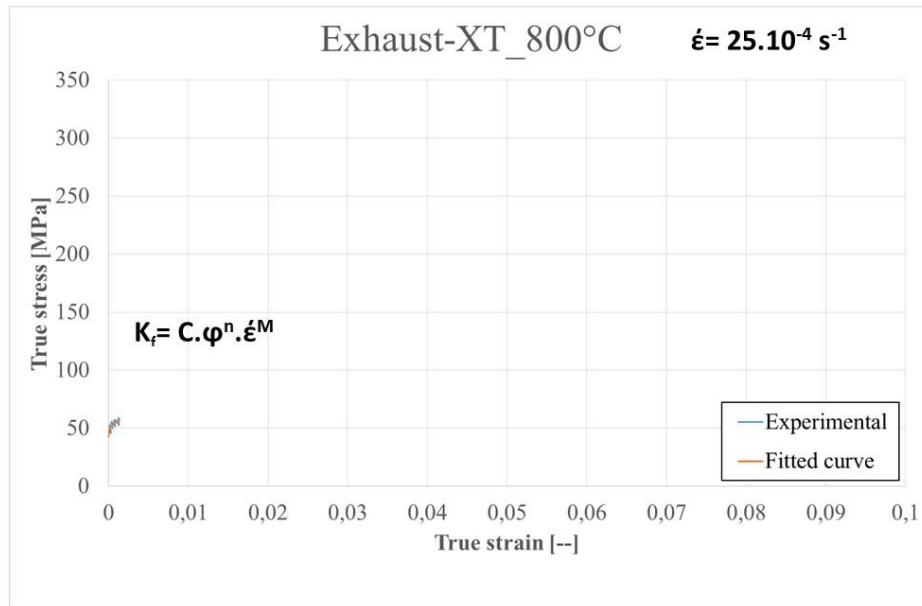


Figure 8-15: Fitted flow curve at 800°C for XT.

Alloy	Temperature [°C]	C	n	M
ASTM Gr.04	400	339.95	0.11	$9 \cdot 10^{-4}$
	500	271.5	0.09	$9 \cdot 10^{-4}$
	600	202.94	0.08	$9 \cdot 10^{-4}$
	700	65.55	0.04	$9 \cdot 10^{-4}$
	800	32.65	0.05	$9 \cdot 10^{-4}$
KS1.2ASNEX	400	426.13	0.18	$8.2 \cdot 10^{-4}$
	500	455.71	0.21	$8.2 \cdot 10^{-4}$
	600	284.9	0.15	$8.2 \cdot 10^{-4}$
	700	137.79	0.077	$8.3 \cdot 10^{-4}$
	800	160.18	0.16	$8.3 \cdot 10^{-4}$
Exhaust-XT	400	505.53	0.17	$8.1 \cdot 10^{-4}$
	500	553.11	0.21	$8.1 \cdot 10^{-4}$
	600	273.36	0.11	$8.1 \cdot 10^{-4}$
	700	139.63	0.05	$8.2 \cdot 10^{-4}$
	800	81.66	0.056	$8.3 \cdot 10^{-4}$

Table 8-1: Fitted parameter of the flow curves according to Hensel/Spittel Ansatz.